Low-Power System Design for Impedance-Based Structural Health Monitoring

Jina Kim

Dissertation submitted to the faculty of the
Virginia Polytechnic Institute and State University
in partial fulfillment of the requirements for the degree of

Doctor of Philosophy
in
Electrical Engineering

Committee:
Dr. Dong S. Ha, Chairman
Dr. James R. Armstrong
Dr. Thomas L. Martin
Dr. Jeffrey H. Reed
Dr. Joseph G. Tront

December 4, 2007
Blacksburg, VA

Keywords: Structural Health Monitoring, Piezoelectric Ceramic Electrical Model, Wideband Method, Binary Method, Damage Detection Quality

Low-Power System Design for Impedance-Based Structural Health Monitoring

Jina Kim
Dr. Dong S. Ha, Chairman
Bradley Department of Electrical and Computer Engineering

(ABSTRACT)

Maintenance of the structural integrity and damage detection are critical for all massive and complicated new and aging structures. A structural health monitoring (SHM) system intends to identify damage on the structure under monitoring, so that necessary action can be taken in advance to avoid catastrophic results. Impedance-based SHM utilizes a piezoelectric ceramic as a collocated actuator and sensor, which measures the electrical impedance of the piezoelectric ceramic over a certain frequency range. The impedance profile of a structure under monitoring is compared against a reference profile obtained from the healthy structure. An existing approach called the sinc method adopts a sinc wave excitation and performs traditional discrete Fourier transform (DFT) based structural condition assessment. The sinc method requires rather intensive computing and a digital-to-analog converter (DAC) to generate a sinc excitation signal. It also needs an analog-to-digital converter (ADC) to measure the response voltage, from which impedance profile is obtained through a DFT. This dissertation investigates system design approaches for impedance-based structural health monitoring (SHM), in which a primary goal is low power dissipation.

First, we investigated behaviors of piezoelectric ceramics and proposed an electrical model in order to enable us to conduct system level analysis and evaluation of an SHM system. Unloaded and loaded piezoelectric ceramics were electrically modeled with lumped linear circuit components, which allowed us to perform system level simulations for various environmental conditions. Next, we explored a signaling method called the wideband method, which uses a pseudorandom noise (PN) sequence for excitation of the structure rather than a signal with a particular waveform. The wideband

method simplifies generation of the excitation signal and eliminates a digital-to-analog converter (DAC). The system form factor and power dissipation is decreased compared to the previously existing system based on a sinc signal. A prototype system was implemented on a digital signal processor (DSP) board to validate its approach. Third, we studied another low-power design approach which employs binary signals for structural excitation and structural response measurement was proposed. The binary method measures only the polarity of a response signal to acquire the admittance phase, and compares the measured phase against that of a healthy structure. The binary method eliminates the need for a DAC and an ADC. Two prototypes were developed: one with a DSP board and the other with a microcontroller board. Both prototypes demonstrated reduction of power dissipation compared with those for the sinc method and for the wideband method. The microcontroller based prototype achieved an on-board SHM system. Finally, we proposed an analytical method to assess the quality of the damage detection for the binary method. Using our method, one can obtain the confidence level of a damage detection for a given damage distance.

Acknowledgements

I first want to thank my advisor, Dr. Dong Ha, for all of his guidance, advice, and motivation throughout my graduate studies. Being his graduate student and a member of Virginia Tech VLSI for Telecommunications Lab was a great opportunity. The advice from my committee members, Dr. James Armstrong, Dr. Thomas Martin, Dr. Jeffery Reed, and Dr. Joseph Tront was also greatly appreciated.

I am grateful to Dr. Daniel Inman and Dr. Benjamin Grisso at Center for Intelligent Material Systems and Structures in Mechanical Engineering at Virginia Tech. They provided excellent technical advice throughout this research, and tremendous help on tests, measurements, and publications. I also appreciate technical and managerial guidance from Dr. Robert Owen at Extreme Diagnostics, Inc. I enjoyed working with them very much.

Additionally, I want to thank National Science Foundation (Grant No. CMS 0120827), Langley Research Center of National Aeronautics and Space Administration, and Extreme Diagnostics, Inc. for their financial support of this research.

I am thankful for the support and assistance of my fellow members of VTVT Lab, including Vipul Chawla, Jeannette Djigbenou, Jihoon Jeong, Jeongki Kim, Na Kong, Yumi Lim, and Rajesh Thirugnanam. All of them made my stay at Virginia Tech enjoyable in and out of research. I wish them all great success in their research and future career.

Finally, I would like to thank my parents, Jang Keun Kim and Hong Kyung Kim. Their constant and limitless love, support, encouragement, and advice were the most essential part of my work and to the fulfillment of my dreams.

This material is based upon work supported by the National Science Foundation under Grant No. CMS 0120827. Any opinions, findings, and conclusions or recommendations

expressed in this material are those of the author and do not necessarily reflect the views of the National Science Foundation.

Dedication

To

Hyung-Jin Lee

Thank you for being a part of my life since 1998.

You made everything possible.

Table of Contents

List of Figures

List of Tables

Chapter 1:
Introduction

Structural Health monitoring (SHM) is a technique to observe and interpret any changes to the structural integrity in order to predict and prevent fatal damage on the structure. SHM is applicable to various civil and aerospace structures, such as aerospace vehicles, bridges, railroads, wind turbine blades, and power plants. Several SHM techniques have been proposed through decades, and now the research interest in SHM field is moving toward development of practical SHM systems that are permanently deployable onto real world structures without out-of-service periods.

There are two distinct approaches in realizing practical SHM systems. One is to develop an autonomous system based in a self-contained hardware with low power dissipation, and the other is to rely on a simple wireless sensor node with a separate base station computer. In the first approach which pursues an autonomous SHM system, key issues are miniaturizing the hardware form factor and reducing the power dissipation, while performing all SHM operations at the self-contained hardware. In the second approach which pursues a wireless SHM system, simplifying the wireless sensor nodes by transferring most of the calculations required for SHM operations to the base station computer is the major issue.

Impedance-based SHM, often simply called an impedance method, uses a piezoelectric patch as a self-sensing actuator and relies on the energy transfer between the piezoelectric patch and the host structure. The piezoelectric patch physically changes shape when an external electric field is applied to work as an actuator, and develops a voltage difference across two of its faces when compressed to work as a sensor. The impedance method has been acknowledged as an efficient SHM technique compared to other conventional SHM techniques in terms of hardware complexity, ease of measured data interpretation, maintenance cost, and coverage area [29][30].

As a traditional impedance method requires an impedance analyzer, which is very costly, and not all projects where the impedance method is applicable have access to an impedance analyzer, a low-cost impedance method has been developed [9]-[12]. A swept sinusoid generated by a signal generator has been used to excite the structure of interest, and the response is measured in terms of voltage. The sinusoidal signal frequency gradually increases until the entire target frequency range is excited. After measuring the structural response, the measured voltage undergoes a fast Fourier transform (FFT) by an FFT analyzer to provide impedance values at each frequency component for structural condition assessment. This first generation low-cost impedance method still demands multiple pieces of equipment and cannot be deployed to real-world structures, though the implementation cost has been reduced compared to the traditional impedance method. Also, this method is highly time-consuming, as each frequency component in the target frequency range must be individually excited.

To address the shortcomings of existing impedance methods, different approaches are investigated. One approach uses a digital wideband signal, and the other approach uses a binary rectangular signal as an excitation signal. The binary rectangular signal also uses an accumulation-based structural condition assessment method. Through these two approaches, the hardware components such as ADC and DAC are removed from the system, and the excitation signal generation and structural condition assessment procedures have been simplified. The binary rectangular signal excitation also enables the binary sensing technique using the phase of the impedance, and resultantly leads to development of the first self-contained and autonomous system in impedance-based SHM and an analytical approach to maintain the damage detection performance.

Chapter 2:
Preliminaries

2.1 Existing Structural Health Monitoring Techniques

Various approaches have been developed for nondestructive evaluation (NDE) through the decades to monitor structural integrity. Traditional nondestructive techniques include ultrasonic testing, acoustic emission, magnetic field analysis, penetrant testing, eddy current techniques, X-ray analysis, impact-echo testing, global structural response analysis, and visual inspections.

2.1.1 Ultrasonic Testing

The Ultrasonic Testing generally uses high frequency sound energy to conduct flaw detection / evaluation, and material characterization [50]. The SHM utilizing the Ultrasonic Testing employs a piezotransducer to produce an acoustic wave in the structure under testing [8][29]. The acoustic energy propagates through the material in a form of waves, and a part of the energy in the acoustic wave is reflected at the point of discontinuity, such as a crack. The reflected wave signal is then transformed into an electrical signal by the piezotransducer. Based on the time delay of the wave transmission, the change in size and density of the material is determined, and the reflector location can be analyzed.

The Ultrasonic Testing is sensitive to both surface and subsurface discontinuities, and highly accurate in determining the reflector position and estimating the size and shape of a structure. However, the Ultrasonic Testing is very hard to apply to materials that are rough, irregular in shape, very small, exceptionally thin, or heterogeneous, and it normally requires a coupling medium to promote the transfer of acoustic waves into the

test specimen [50]. Furthermore, the Ultrasonic Testing requires an experienced technician to review the ultrasonic data and discern details.

2.1.2 Acoustic Emission

Acoustic Emission is an elastic wave produced by a rapid release of energy by the changes in the internal structure, such as crack initiation / growth, crack opening / closure, and dislocation movement [51]. The elastic wave propagates through the solid to the surface, where it can be recorded by sensors, which are usually transducers to provide information about the existence and location of the possible source of internal structural changes. Acoustic Emission detects defect activity inside the material by monitoring the active defects through surface-bonded sensors when the structure is in-operation. Acoustic Emission technique has been applied in numerous structural components, such as steam pipes and pressure vessels, and in the research areas of rocks, composite materials, and metals.

The Acoustic Emission technique differs from other NDE methods; Acoustic Emission detects the activities inside the materials, while other NDE methods examine the internal structures of the materials. The disadvantage of Acoustic Emission is that commercial Acoustic Emission systems can only estimate qualitatively how much damage is in the material and approximately how long the components will last [51]. So, other NDE methods are still needed to do more thorough examinations and provide quantitative results. Moreover, service environments are generally very noisy, and the Acoustic Emission signals are usually very weak. Thus, signal discrimination and noise reduction are very difficult yet extremely important for successful Acoustic Emission applications [51].

2.1.3 Impact-Echo Testing

The Impact-Echo method operates well specifically for concrete and masonry structures. The impact-echo method uses transient stress waves generated in the

materials, such as concrete or masonry, by an elastic and low-energy impact on the surface of the structure [52]-[54]. The stress waves propagate through the material, and are reflected by air interfaces, such as delaminations, voids, and cracks within the structure or at the external boundaries of the structure. Transmitted stress waves arrive at the surface of the structure and the resulting surface displacements are recorded by a transducer located adjacent to the impact. The piezoelectric crystal in the transducer produces a voltage proportional to displacement, and the resulting voltage-time signal is analyzed to determine the presence and nature of any internal flaws or external interfaces of the structure. The Impact-Echo Testing presents high efficiency in detecting and locating large-scale voids and delaminations, but is not sensitive to the presence of small cracks and discontinuities due to low excitation frequency [29].

2.2 Impedance-Based Structural Health Monitoring

Impedance-based SHM, often simply called an impedance method, uses a piezoelectric patch as a self-sensing actuator and relies on the energy transfer between the piezoelectric patch and the host structure. The piezoelectric patch works as an actuator by physically changing the shape when an external electric field is applied, and works as a sensor by developing a voltage difference across two of its faces when compressed.

The electrical admittance of the piezoelectric patch $Y_p(j\omega)$ is the combined function of the mechanical impedance of the piezoelectric patch itself $Z_p(j\omega)$ and that of the host structure $Z(j\omega)$ as expressed in equation (2.1) [20].

$$Y_p(j\omega) = j\omega a\left(\bar{\varepsilon}_{33}^{T}(1-j\delta) - \frac{Z(j\omega)}{Z(j\omega)+Z_p(j\omega)} d_{32}^2 Y_{22}^E\right) \tag{2.1}$$

where a, d_{32}, Y_{22}^E, $\bar{\varepsilon}_{33}^{T}$ and δ denote a geometry constant, a piezoelectric coupling constant, the complex Young's modulus of the piezoelectric patch at zero electric field, the complex dielectric constant of the piezoelectric patch at zero stress, and the dielectric loss tangent of the piezoelectric patch, respectively. The first term in equation (2.1) is the

capacitive admittance of a free piezoelectric patch, and the second is the result of the electromechanical interaction of the piezoelectric patch with the host structure [20]. As the electrical admittance of the piezoelectric patch pertains to the mechanical impedance of the host structure, any changes in the measured electrical impedance of the piezoelectric patch indicate the changes in the structural integrity. Thus, the traditional impedance method measures the electrical impedance of the piezoelectric patch using an impedance analyzer, and computes the electrical admittance of the piezoelectric patch to inspect the host structure's mechanical condition.

Equation (2.1) can also be rewritten as

$$Y_p = \omega a\left(\delta\bar{\varepsilon}_{33}^{T} + y_i\right) + j\omega a\left(\bar{\varepsilon}_{33}^{T} - y_r\right) \tag{2.2}$$

where

$$y_r = \frac{Z_r\left(Z_r + Z_{p,r}\right) + Z_i\left(Z_i + Z_{p,i}\right)}{\left(Z_r + Z_{p,r}\right)^2 + \left(Z_i + Z_{p,i}\right)^2} d_{32}^2 Y_{22}^E \tag{2.3}$$

and

$$y_i = \frac{Z_i\left(Z_r + Z_{p,r}\right) - Z_r\left(Z_i + Z_{p,i}\right)}{\left(Z_r + Z_{p,r}\right)^2 + \left(Z_i + Z_{p,i}\right)^2} d_{32}^2 Y_{22}^E \tag{2.4}$$

y_r and y_i denote the coupling terms, Z_r, $Z_{p,r}$, Z_i, and $Z_{p,i}$ are the real and imaginary parts of the host structure and piezoelectric patch impedance, respectively [20]. In equation (2.2), both the real and imaginary parts of Y_p are positive linear function of frequency ω, and the slopes are functions of coupling terms and non-coupling terms. The non-coupling term of the real part slope is much smaller than that of the imaginary part slope, as δ is typically less than 1%. Therefore, the real part of Y_p fluctuates much more than the imaginary part, which is why the conductance of the piezoelectric patch is employed for impedance-based SHM [18]-[20][28].

2.3 Previous Efforts in Impedance-Based SHM

2.3.1 Traditional Method

The traditional approach developing an impedance-based SHM system relies on an impedance analyzer for excitation and sensing, and a computing unit for structural condition assessment. The impedance analyzer excites the structure with one frequency at a time by incrementing the output frequency gradually and measures the electrical impedance of the structure.

The measured electrical impedance of the structure is post processed in a computer using computation software, such as MATLAB. Though this traditional approach realizes the full operation of impedance-based SHM by employing several pieces of equipment, especially an impedance analyzer, its application is hindered to various types of structures. While the traditional approach which employs an impedance analyzer is the most primitive, it is faithful to the theoretical background of the impedance-based SHM. However, the impedance analyzer is bulky and expensive, so not all projects can afford it.

2.3.2 Low-Cost Method

The Low-Cost Method is proposed to improve the accessibility of the impedance method. Since the traditional approach using an impedance analyzer has problems of cost and size, the Low-Cost Method utilizes a sensing resistor and two extra pieces of equipment, which are smaller, lighter and less expensive than an impedance analyzer. The Low-Cost Method uses a signal generator to generate an excitation signal, which is a sinusoidal sweep signal, and utilizes a resistor to estimate the admittance of the structure. The sensing resistor forms a voltage divider with the collocated actuator / sensor, and estimates the voltage across the collocated actuator / sensor through the voltage across itself. The sensed voltage is then processed by an FFT analyzer to obtain a frequency domain response of the structure. The frequency domain structural response is finally processed in a separate computer to assess the structural condition by calculating the

damage metric. The damage metric is a root mean squared deviation (RMSD) between the current measurement and the baseline measurement. The merit of the Low-Cost Method is that the impedance method is implemented without employing an impedance analyzer, which is so expensive and large that it hinders the application of the impedance method to actual structures. However, the Low-Cost Method still requires multiple equipments to excite the structure and sense the response, and a computer to perform structural condition assessment.

2.3.3 Sinc Method

The Sinc Method is the first approach that develops an impedance-based SHM on a self-contained hardware. In the Low-Cost Method, each function of the SHM operation, except excitation of the structure and sensing the structural response, was performed by separate equipment: Generation of the excitation signal was performed by a signal generator, an FFT analyzer was in charge of a signature generation, and a computer performed a structural response assessment, while a single resistor accomplished actuation and sensing. Therefore, the Sinc Method replaces those equipments with a digital signal processor (DSP) system, while keeping the sensing resistor. The DSP system, which includes a DSP evaluation module (EVM), a DAC EVM, and an ADC EVM, generates the excitation signal, creates the impedance signature, and assesses the structural condition. In terms of the system form factor and the cost, the Sinc Method is shrunk down to three PCBs from three pieces of equipment including a computer, and is reduced to a couple hundred dollars. Another improvement from the Low-Cost Method to the Sinc Method is the excitation signal type, which is a sinc wave instead of sinusoidal sweep signal. The sinc wave is a superposition of multiple frequency components in a time domain, while the sinusoidal sweep signal is a spread of multiple frequency components in a time domain. Thus, the Sinc Method can excite the structure within a shorter period of time compared to the Low-Cost Method and the Traditional Method, which leads the Sinc Method to lower power dissipation by increasing the idle time.

While the DSP performs all computations of the impedance-base SHM operation and the sensing resistor is in charge of sensing the structural response, the DAC is necessary to provide an exact waveform of sinc for structural excitation, and the ADC is essential to support the FFT operation by offering accurate voltage levels of the structural response.

2.3.4 Impedance-Chip Method

The Impedance-Chip Method takes a different approach than the Sinc Method in improving the Low-Cost Method toward an autonomous system development. The Impedance-Chip Method uses a commercially available impedance converter system, which combines an on-board frequency generator with an ADC and a DSP engine. The frequency generator makes the structure excited with the frequency components of the target frequency range, and the structural response is sampled by an on-board ADC. The sampled response is transformed into a frequency domain through a discrete-time Fourier transform (DFT) by an on-board DSP engine. The impedance converter system does not use a sensing resistor, but uses an inverting op-amp configuration to estimate the admittance of the structure.

Since the DSP engine of the impedance converter system does not support any extra operations other than DFT, the structural condition assessment should be performed on a separate computing unit. Thus, the Impedance-Chip Method employs a wireless transmitter to transmit a data stream of the DFT result to the base station computer. The base station computer calculates the damage metric based on the received frequency domain structural response, and determines if the structure is damaged or not.

The major distinction between the Impedance-Chip Method and the Sinc Method is that the Impedance-Chip Method requires a separate computer for structural condition assessment, while the Sinc Method provides a fully self-contained solution.

2.4 Summary

It becomes important to minimize the processing burden and the amount of information from the SHM system, as the central control system gets complicated and the amount of information that an end user has to process increases with the growth of structural complexity, especially for aerospace vehicles [14]. Therefore, this work takes the approach of a stand-alone autonomous SHM system based on the impedance method.

First, the piezoelectric patch used as a collocated actuator / sensor is characterized in an electrical model. The characteristics of the piezoelectric patch are investigated without and with bonding to the surface of the host structure. To address the problem of reliance on a base station computing unit of the Impedance-Chip Method and to improve the figure of merit in terms of form factor and power dissipation from the Sinc Method, new methods are proposed. One method employs a binary wideband excitation signal, and the other uses a binary rectangular excitation signal. More importantly, a structural condition assessment technique enabled by binary structural response is proposed together with the binary rectangular excitation method. Finally, the performances of the proposed methods are analyzed through simulations based on the electrical model of the piezoelectric actuator / sensor.

Chapter 3:
Equivalent Circuit Model of PZT

3.1 Piezoelectricity

Piezoelectricity is an ability of some materials to generate an electric potential in response to applied mechanical stress [45]. As the piezoelectric effect is reversible, the materials that demonstrate the direct piezoelectric effect, which is the generation of electricity upon applied mechanical stress, demonstrate the converse piezoelectric effect, which is the generation of stress and strain upon applied electric field, as well [45][46]. There are different types of piezoelectric materials, and some representative materials include quartz, a natural crystal, and Lead Zirconate Titanate (PZT), a man-made ceramic, respectively.

The Impedance-based SHM employs a piezoelectric transducer made of single layer piezoelectric ceramic as a collocated sensor / actuator, and PZT, which is employed in this work as a surface-mountable sensor / actuator in a form of a thin patch. PZT is the most widely used piezoelectric ceramic due to its high actuation ability [40][45]. When an electric field is placed across the thickness of a PZT patch as the original polarization field, the PZT patch expands along the axis of polarization (thickness direction) and contracts perpendicular to the axis of polarization (length and width direction) [43]. PZT typically changes its shape up to 0.1% of the original dimension [45][46]. As impedance-based SHM observes the mechanical condition of the structure through electrical signals, it is meaningful to model the piezoelectric behavior of a PZT patch itself and the interaction between a PZT patch and the structure in terms of an electric equivalent circuit.

3.2 Existing Equivalent Circuit Models of Piezoelectric Ceramics

3.2.1 Unloaded Piezoelectric Ceramics

The most basic equivalent circuit model characterizing a piezoelectric ceramic such as a PZT patch near the resonant frequency is the Van Dyke Model shown in Figure 3.1, which is also generally used to model electromechanical resonance characteristics of crystal oscillators [1][37]. The Van Dyke Model is a parallel connection of a branch with R_1-L_1-C_1 in series representing mechanical damping, mass, and elastic compliance transformed into electrical magnitude by the reverse piezoelectric effect mechanical behavior of PZT and C_0 representing the electrostatic capacitance between the two parallel plates of the PZT patch [37].

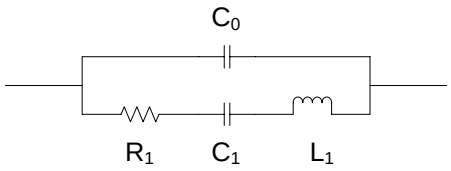

Figure 3.1 The Van Dyke Model

For more accurate modeling of piezoelectric ceramics, other equivalent circuit models applied some improvements to the Van Dyke Model. There are two well-established modeling methods for the impedance of the unloaded piezoelectric ceramics: One is to fit the impedance to an equation representing the material's characteristics to determine the elastic, dielectric and piezoelectric constant, and the other is to fit the impedance to a lumped element circuit model to predict the electric behavior of the resonator [38].

The Sherrit Model follows the first method by estimating the circuit parameters from the material characteristics. The Van Dyke Model cannot accurately model the material characteristics, particularly for materials with significant losses [38]. Adding a

frequency independent resistance in parallel to a capacitor or inductor is less general than representing these losses with complex circuit components [38]. Therefore, the Sherrit Model employs complex circuit components only as shown in Figure 3.2 to model the piezoelectric ceramic associating piezoelectric losses. Notice that the circuit component values of the Sherrit Model are found as complex numbers, while those of the Van Dyke Model are determined as real numbers.

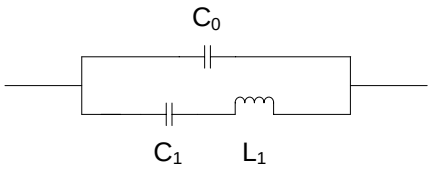

Figure 3.2 The Sherrit Model

The Guan Model is the most recent equivalent circuit model of piezoelectric ceramics relying on the other method, which estimates values of the electrical components based on the electrical behavior of the piezoelectric ceramics. The Guan model, as shown in Figure 3.3, proposes to add both a series resistor R_s and a parallel resistor R_p to C_0 of the Van Dyke Model to consider the energy dissipation [40]. Determination of the values of the electric components is as follows [40]: C_0 is first considered according to the impedance curve. C_1 is then chosen by visual inspection on the magnitude and phase of the impedance near the resonant frequency, and L_1 is calculated based on the relationship, expressed in equation (3.1), between the resonant frequency ω0 and the value of C_1.

$$\omega_0 = \frac{1}{\sqrt{L_1 C_1}} \tag{3.1}$$

The value of R_1 is determined depending on the decay speed of the impedance magnitude at the resonant frequency. Finally, values of R_s and R_p are decided by the amount of energy dissipation.

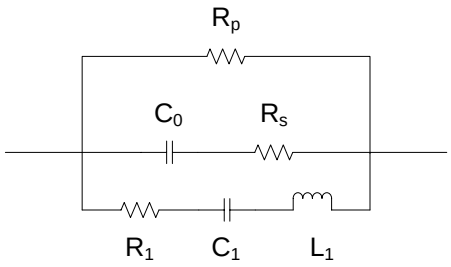

Figure 3.3 The Guan Model – Unloaded piezoelectric ceramics

The Guan Model tries to improve the accuracy of the Van Dyke Model by encompassing R_s and R_p as a consideration of the energy dissipation. However, the values of R_s and R_p may have variations resulting in another type of inaccuracy from the exciting frequency and amplitude because energy loss varies with exciting signal amplitude and frequency [40].

3.2.2 Loaded Piezoelectric Ceramics

The Van Dyke Model shown in Figure 3.1 is suitable for modeling the characteristics of a piezoelectric ceramic only in a narrow frequency range around a resonant frequency, which make the Van Dyke Model applicable only to an unloaded piezoelectric ceramic. When a piezoelectric ceramic is attached to a mechanical structure as a collocated actuator / sensor, the mechanical boundary conditions of the piezoelectric ceramic changes [40], and accordingly a different circuit model is required for a loaded piezoelectric ceramic. It has been observed through the literature that the loaded piezoelectric ceramic experiences multiple resonances at frequencies lower than the resonant frequency of the unloaded piezoelectric ceramic. Therefore, an approximated circuit model for a wider frequency ranger with multiple resonant frequencies can be employed as an equivalent circuit model for a loaded piezoelectric ceramic, as shown in Figure 3.4 by adding additional R-L-C branches in parallel to the R_1-L_1-C_1 branch of the Van Dyke Model [37].

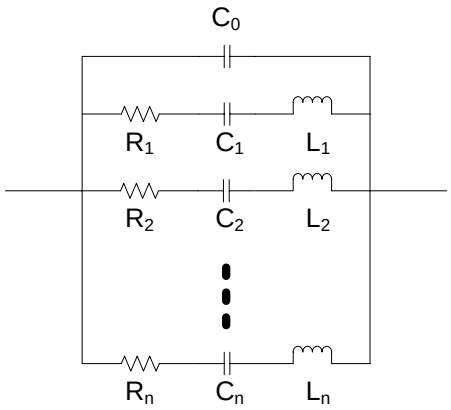

Figure 3.4 The Van Dyke Model extended for a frequency range with multiple resonant frequencies

The Guan Model that estimates an unloaded piezoelectric ceramic accommodating the energy dissipation is also extended to represent a loaded piezoelectric ceramic based on the extended Van Dyke Model as shown in Figure 3.5. Mechanical structures usually have multiple resonant modes that are much lower than the resonant frequency of an unloaded piezoelectric ceramic, and each resonant mode has its equivalent mass, damping coefficient, and spring constant respectively [40]. Therefore, each R_i-C_i-L_i branch in the complete Guan Model shown in Figure 3.5 physically stands for a mechanical resonant mode.

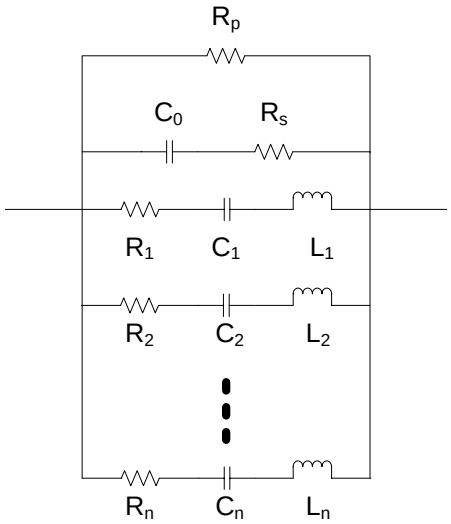

Figure 3.5 The complete Guan Model – Loaded piezoelectric ceramics

The values of R_i, C_i, and L_i, for i from 1 to n, are determined by the same method as the obtained values of R_1, C_1, and L_1 discussed in Section 3.2.1. The complete Guan Model has difficulty in determining R_i-C_i-L_i values when the resonant frequencies of the piezoelectric ceramic and the structure are very close to each other or overlapping [40].

3.3 Easy Model

This work proposes the Easy Model, which is an equivalent circuit model applicable to an unloaded or loaded piezoelectric ceramic, in order to approximate the electrical behavior of the piezoelectric ceramic in terms of lumped electrical components [60].

3.3.1 Test Configuration

As a first step to design the Easy Model, the electrical properties of the piezoelectric ceramic are investigated by measuring the electrical impedance of the piezoelectric ceramic using an impedance analyzer HP 4194A. The impedance is measured from 10 KHz to 100 KHz with a frequency resolution of 20 Hz. A PZT sheet *PSI-5H4E-T110* available from Piezo Systems, Inc. is selected as a piezoelectric ceramic in developing the Easy Model and cut into a smaller piece to be used as a specimen. Note that the same type of PZT is used as a piezoelectric transducer for all other tests throughout this work.

The test configurations for unloaded PZT and loaded PZT are illustrated in Figure 3.6. The PZT patch is excited with an electrical signal to produce a mechanical actuation to the structure, and the mechanical response from the structure is measured through the PZT patch in a format of an electrical signal. Thus, a pair of wires should be connected to each face of the PZT patch. Since the PZT patch is attached to the surface of a structure, one side of a loaded PZT patch is not accessible. Thus, a piece of copper tape is used to provide a route to the bottom of the PZT patch that is in contact with the structure as shown in Figure 3.6 (b). For the purpose of symmetry, a piece of copper tape

of the same size is attached to the top of the PZT patch, and a pair of wires is connected to the pair of copper tapes by soldering. Since the thickness of the copper tape shown in Figure 3.6 is only 35 μm, a loaded PZT patch actually has full contact with the structure and the gap between the PZT patch and the structure shown in Figure 3.6 (b) is an exaggeration. As presented in Figure 3.6 (a), unloaded PZT includes the PZT patch and a pair of copper tapes to keep test conditions of the specimen identical for unloaded and loaded cases except the attachment to the structure.

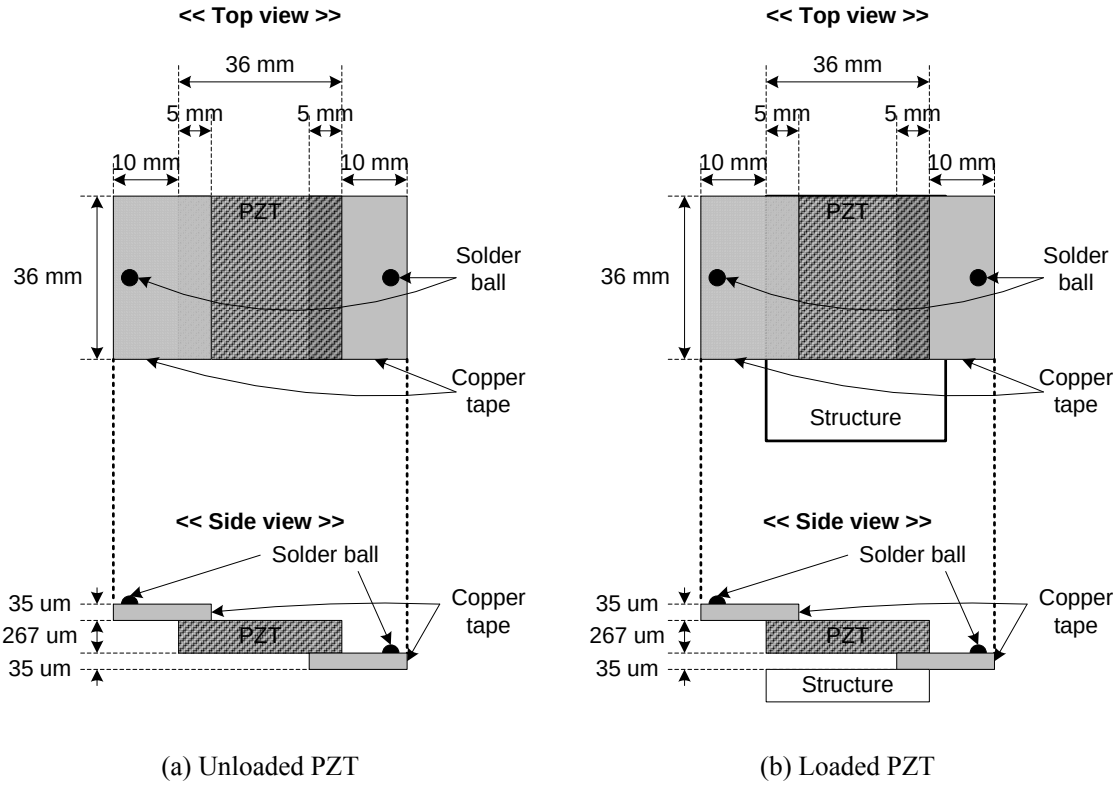

(a) Unloaded PZT (b) Loaded PZT

Figure 3.6 Typical test configurations for an unloaded PZT and a loaded PZT (not to scale)

In case of loaded PZT measurement and modeling, an aluminum beam is used as a test structure whose dimension and PZT bonding location are depicted in Figure 3.7. The loaded PZT is modeled once without damage and then with damage. As a simulated damage, a pair of magnets is used to apply pressure to the structure.

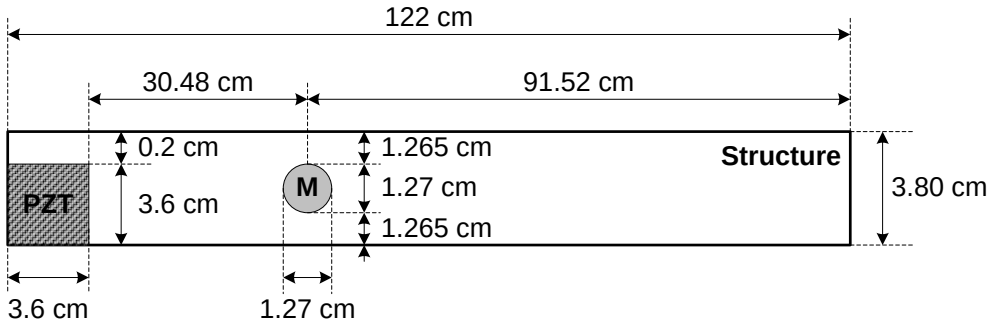

(a) Top view

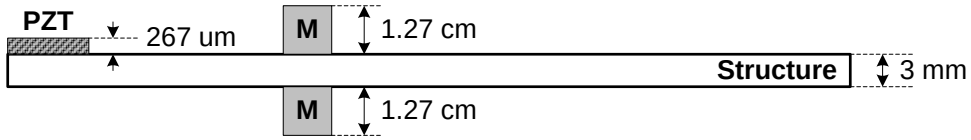

(b) Side view

Figure 3.7 Test configuration for a loaded PZT with two magnets as a simulated damage (not to scale)

3.3.2 Unloaded PZT

The measured impedance of unloaded PZT shown in Figure 3.6 (a) is presented in Figure 3.8. From the reactance curve shown in Figure 3.8 (a), one can observe that the specimen has a series resonance at 45 KHz and a parallel resonance at 55 KHz, and at the parallel resonant frequency the magnitude becomes the maximum. The PZT patch is inductive between the series resonant frequency and the parallel resonant frequency, and capacitive in other frequency ranges. In low frequency range, the reactance approaches negative infinity as the frequency decreases to DC. It can also be noted from the resistance curve that the base resistance outside the resonant frequency range is about 5 Ω.

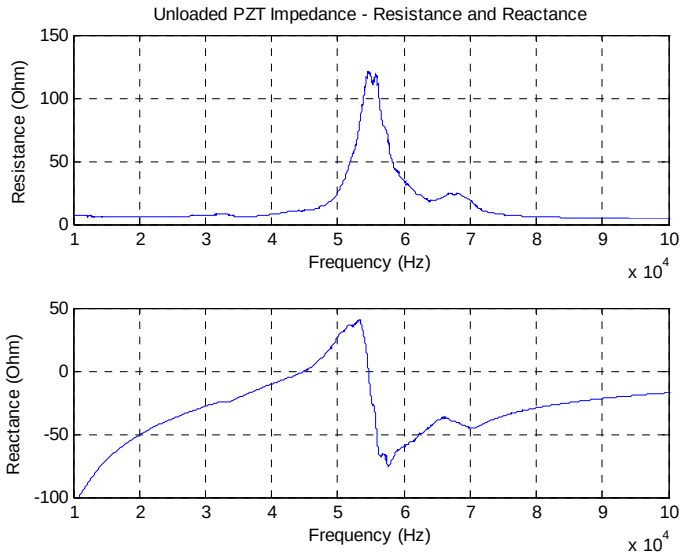

(a) Resistance and Reactance

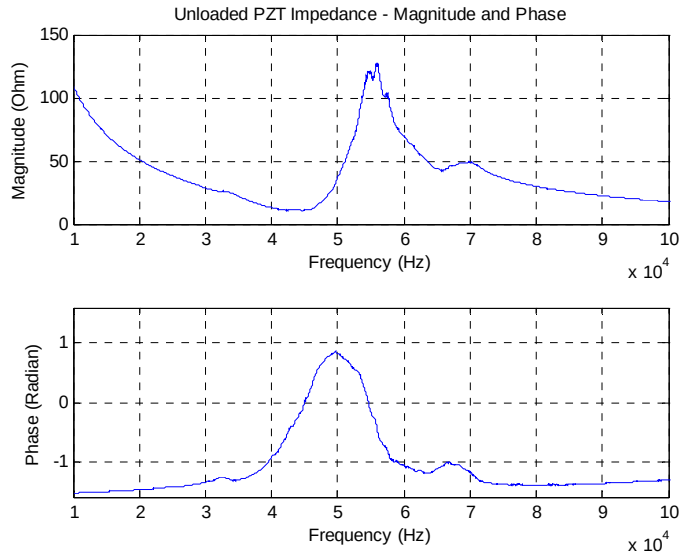

(b) Magnitude and Phase

Figure 3.8 Unloaded PZT Impedance

Since it is easy to detect where the parallel resonant frequency is from the reactance of the measured impedance, the resonance characteristics of the unloaded PZT patch can be modeled using a parallel RLC tank circuit. For a higher accuracy, an additional resistor connected in series to the RLC tank circuit is desired because the

unloaded PZT patch demonstrates almost constant resistance over the frequency range away from the resonant frequency. Also, from the fact that the reactance converges to negative infinity with decreasing frequency in low frequency range, a series capacitor to an RLC tank circuit is needed. Therefore, an RLC tank circuit with a resistor and a capacitor in series as shown in Figure 3.9 can model the electrical characteristics of an unloaded PZT patch, and it is the proposed Easy Model.

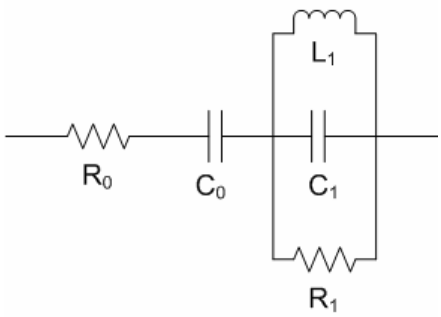

Figure 3.9 The Easy Model for unloaded PZT

Determination of the values of electrical components in the Easy Model begins with finding the value of the base resistance R_0 from the resistance curve and that of the series capacitance C_0 from the reactance curve. Then, the parallel resonant frequency ω_p is determined based on the reactance curve, and the resistance at the parallel resonant frequency is read from the resistance curve. After determining values of initial parameters, the value of R_1 can be calculated as

$$R_1 = R_{p,unloaded}\left(\omega_p\right) - R_0 \tag{3.2}$$

where $R_{p,unloaded}\left(\omega\right)$ is the measured resistance of the unloaded PZT patch at a particular frequency ω. Since the parallel resonant frequency ω_p and the quality factor Q of the RLC tank circuit are $\omega_p = \frac{1}{\sqrt{LC}}$ and $Q = R\sqrt{\frac{C}{L}}$ respectively, the value of L1 can be calculated as

$$L_1 = \frac{R_1}{\omega_p \cdot Q} \tag{3.3}$$

and the value of C1 can be obtained as

$$C_1 = \frac{1}{L_1 \cdot \omega_p^{\,2}} \tag{3.4}$$

Finally, the total estimated impedance of the unloaded PZT patch from the equivalent circuit model $Z_{pm,unloaded}(\omega)$ becomes

$$Z_{pm,unloaded}(\omega) = R_0 + \frac{1}{j\omega C_0} + \frac{1}{\frac{1}{R_1} + \frac{1}{j\omega L_1} + j\omega C_1} \tag{3.5}$$

The resulting values of electrical components of the Easy Model for the specimen calculated through the procedure presented in equations from (3.2) to (3.5) are tabulated in Table 3.1. The dotted lines in Figure 3.10 show the estimated impedance of the specimen based on the Easy Model, whose total impedance is expressed in equation (3.5). From a visual inspection, the Easy Model follows the trends of the measured impedance in four aspects, which are resistance, reactance, magnitude and phase. For a quantitative comparison, correlation coefficients between the measured impedance and the modeled impedance are calculated for resistance, reactance, magnitude and phase, separately as summarized in Table 3.2. The Easy Model estimates the PZT impedance with an approximated agreement rate of 99%.

Table 3.1 Unloaded PZT Easy Model circuit component values with single resonant frequency

R_0 (Ω)	5	R_1 (Ω)	115
C_0 (μF)	0.15	C_1 (μF)	0.277
		L_1 (μH)	30.253

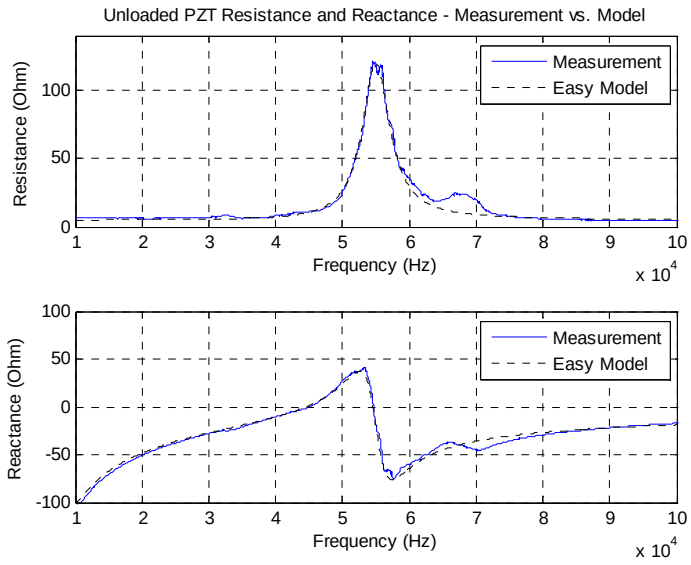

(a) Resistance and Reactance

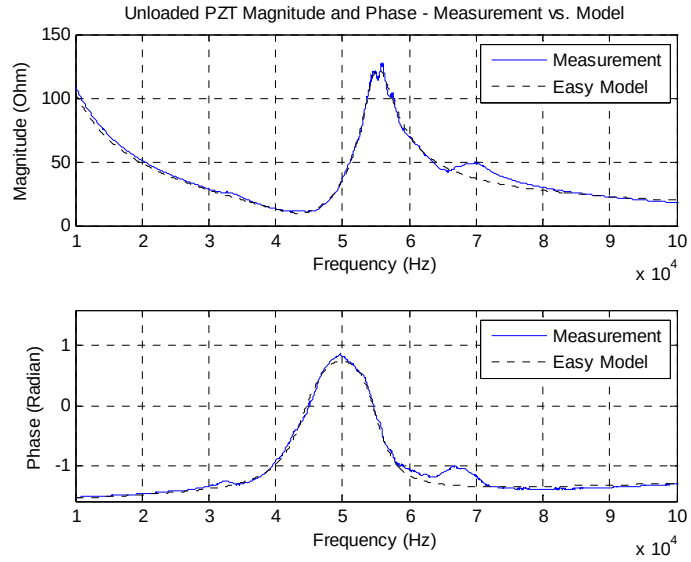

(b) Magnitude and Phase

Figure 3.10 Unloaded PZT impedance comparison with single resonant frequency – Measurement vs. Easy Model

Table 3.2 Unloaded PZT impedance comparison with single resonant frequency – Correlation coefficients between Measurement and Easy Model

Impedance Component	Correlation Coefficient
Resistance	0.9887
Reactance	0.9922
Magnitude	0.9932
Phase	0.9926

Note that the Easy Model shown in Figure 3.9 is another form of the Van Dyke Model shown in Figure 3.1. The series RLC branch and a parallel capacitor of the Van Dyke Model are transformed into a parallel RLC tank and a series capacitor in the Easy Model. The series to parallel conversion of the RLC components that represent the mechanical features of PZT is applied in order to make the calculation required to find the values of the electrical components of the model straightforward. Though the Van Dyke Model represents the physical characteristics of PZT better than the Easy Model, the Easy Model provides a simpler calculation procedure, which can also be programmed, for the component values based only on the measured electrical impedance of PZT.

Since the unloaded PZT patch tested in this section includes a pair of copper tapes as shown in Figure 3.6 (a), the measured impedance of the unloaded PZT has a local resonant frequency around 68 KHz, which is ignored in modeling with the Easy Model as shown in Figure 3.10. The Easy Model can still approximate the measured impedance of the specimen with 99% accuracy even without modeling the local resonance because rather than the copper tapes, the PZT patch is the dominant factor of an unloaded PZT. The Easy Model for a loaded PZT is discussed in the next section, and a local resonance of an unloaded PZT will be revisited for a more precise and better fitted modeling.

3.3.3 Loaded PZT

As discussed in Section 3.2.1, mechanical structures usually have multiple resonant frequencies depending on the mechanical characteristics of structures. Thus, when a PZT patch is bonded to a structure, the resonant mode of unloaded PZT has

interaction with each of the resonant modes of the structure as shown in Figure 3.11. In Figure 3.11, it is assumed that the structure has *n* resonant frequencies, and the subscripts *pmu* and *s* denote PZT Model Unloaded and Structure, respectively. Note the unloaded PZT model is same as the Easy Model shown in Figure 3.9.

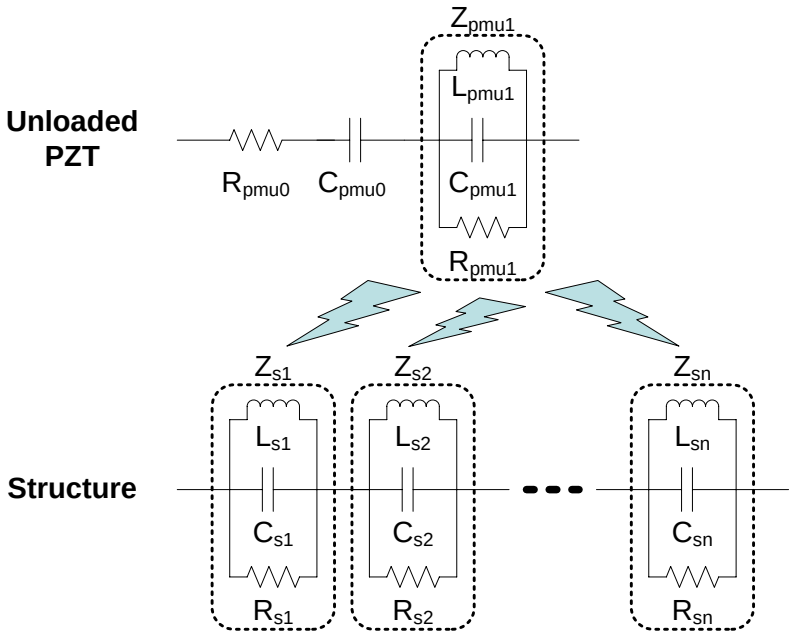

Figure 3.11 Interaction between unloaded PZT and a structure

The impedance-based SHM relies on the energy transfer between PZT and the structure, and consequently the interaction, which occurs upon the attachment of the PZT patch to the structure, between Z_{pmu1} and Z_{si}, where i is from 1 to n, can be explained with a concept of a transformer as shown in Figure 3.12. The first row of Figure 3.12 shows the equivalent circuit model of PZT and a structure at a resonant frequency using an RLC tank circuit based on the Easy Model. Z_{pmu1} block represents the resonance of PZT and Z_{si} block represents one of the resonances of the structure. When a PZT patch is bonded to the surface of a structure, the inductors of PZT and the structure forms a transformer with a transfer ratio of N_p:N_s depending on the characteristics of the structure at the specific resonant mode i as shown in the second row of Figure 3.12. Note the inductors of RLC tank circuits, L_{pmu1} and L_{si}, are distributed into two elements satisfying

$L_{pmu1} = L_{pmu11} \| L_{pmu12}$ and $L_{si} = L_{si1} \| L_{si2}$. Then, as illustrated in the third row of Figure 3.12, the inductance of PZT constituting the transformer, L_{pmu12}, can be replaced with the structure's impedance seen by PZT, Z_{si}', where $Z_{si}' = Z_{si} \cdot \left(N_p / N_s\right)^2$. Then, the impedance of loaded PZT at a resonant frequency ω_i, Z_{pmli} becomes a parallel connection of RLC tank circuits of PZT, excluding the inductance forming a transformer and an impedance of the structure seen by PZT, which is $Z_{pmli} = R_{pmu1} \| C_{pmu1} \| L_{pmu11} \| Z_{si}'$. Finally by distributing RLC components of Z_{si}', a new equivalent RLC tank circuit representing the behavior at a resonant frequency ω_i is obtained with R_{pmli}, C_{pmli}, and L_{pmli} as illustrated in the forth row of Figure 3.12.

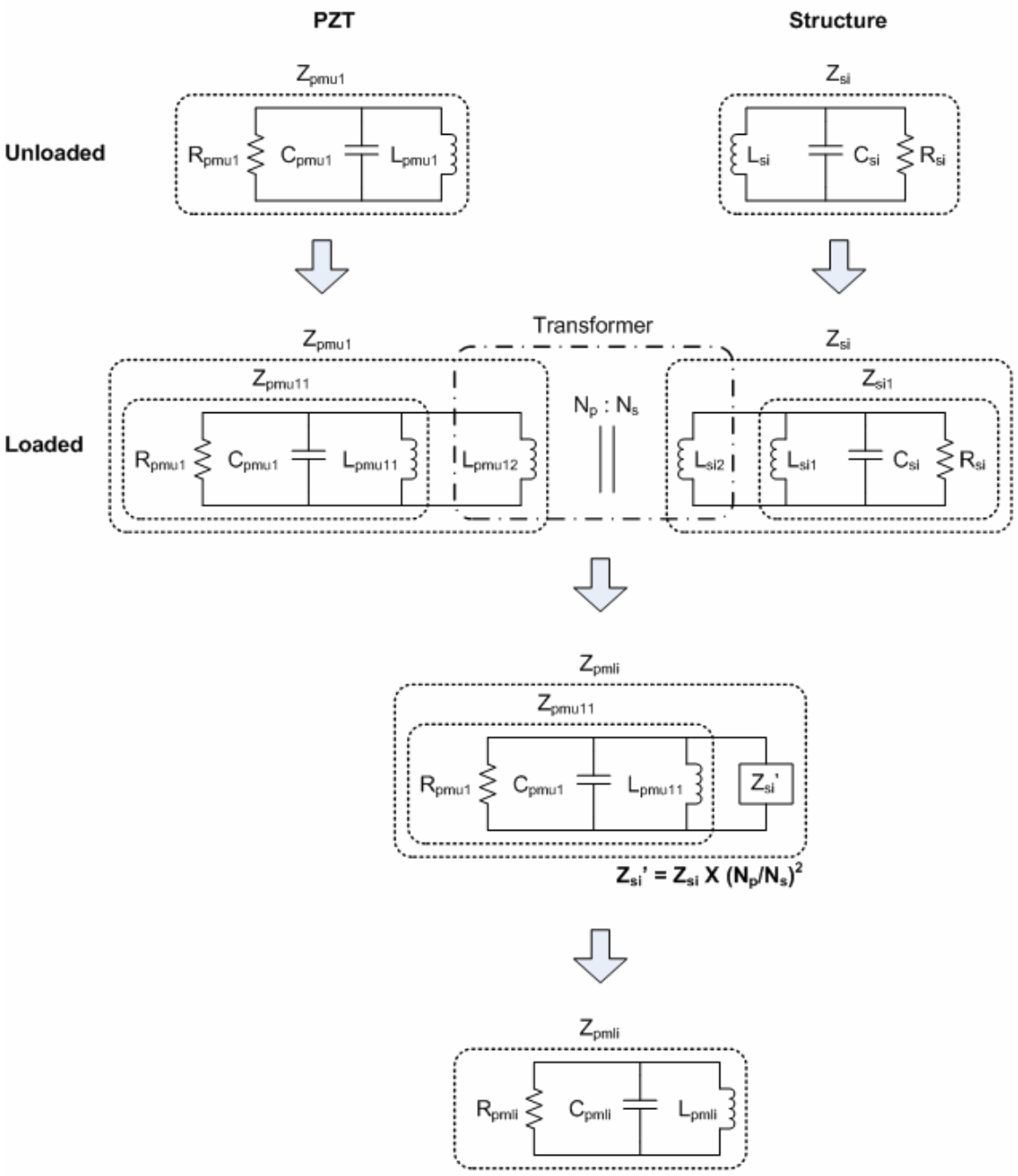

Figure 3.12 PZT and structure as a transformer

The same procedure presented in Figure 3.12 is applied to all resonant frequencies of the structure, and the Easy Model shown in Figure 3.9 is extended as shown in Figure 3.13 to compose the Easy Model for loaded PZT. Note the values of R_0 and C_0 should be adjusted according to the measured impedance of a loaded PZT, rather than by

duplicating the values determined for an unloaded PZT model. The total estimated impedance of the loaded PZT patch from the equivalent circuit model $Z_{pm,loaded}(\omega)$ becomes

$$Z_{pm,loaded}(\omega) = R_0 + \frac{1}{j\omega C_0} + \sum_{i=1}^{n} \frac{1}{\frac{1}{R_i} + \frac{1}{j\omega L_i} + j\omega C_i} \tag{3.6}$$

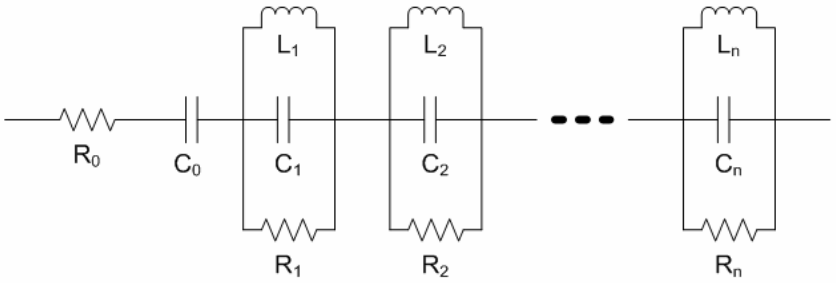

Figure 3.13 Easy Model for loaded PZT

Figure 3.14 shows the measured impedance of a loaded PZT exhibiting multiple resonant frequencies especially in frequency ranges from 12 KHz to 20 KHz and from 65 KHz to 72 KHz. To demonstrate the appropriateness and estimate the performance of the Easy Model for loaded PZT, a representative frequency range from 12 KHz to 20 KHz is selected.

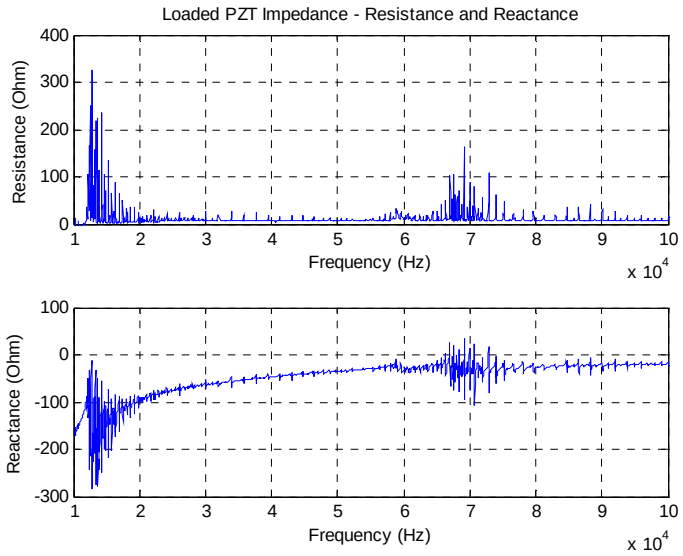

(a) Resistance and Reactance

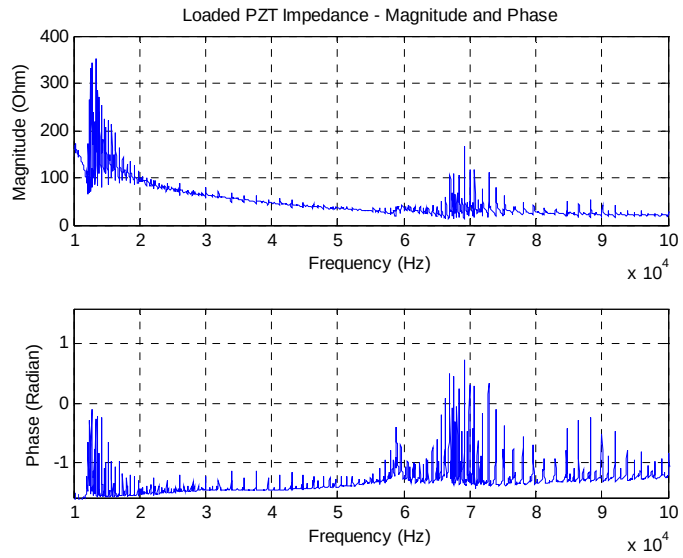

(b) Magnitude and Phase

Figure 3.14 Loaded PZT Impedance

Through the determination and calculation procedure used for unloaded PZT covered in Section 3.3.2, component values for loaded PZT are acquired. There are 50 resonant frequencies in the selected frequency range. The dotted lines in Figure 3.15 show the estimated impedance of the loaded PZT based on the Easy Model, whose total

impedance is expressed in equation (3.6). From a visual inspection, the Easy Model follows the trends of the measured impedance of loaded PZT in four aspects, which are resistance, reactance, magnitude and phase. For a quantitative comparison, correlation coefficients between the measured impedance and the modeled impedance are calculated for resistance, reactance, magnitude and phase, separately as summarized in Table 3.3. The Easy Model estimates the loaded PZT impedance with an average agreement rate of 93%.

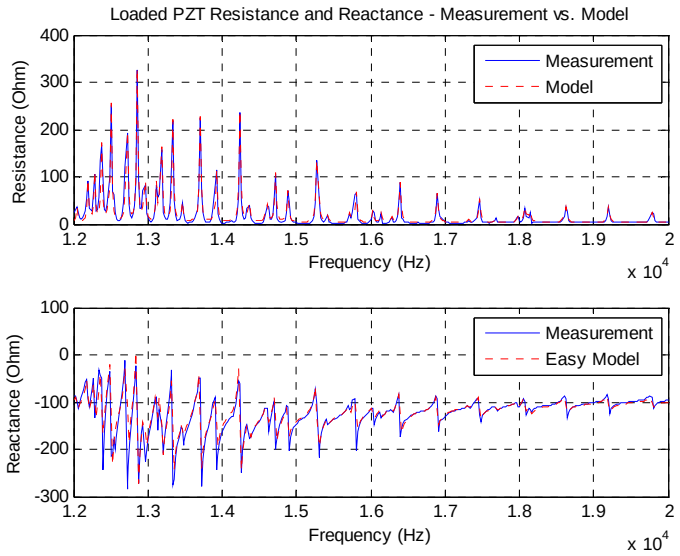

(a) Resistance and Reactance

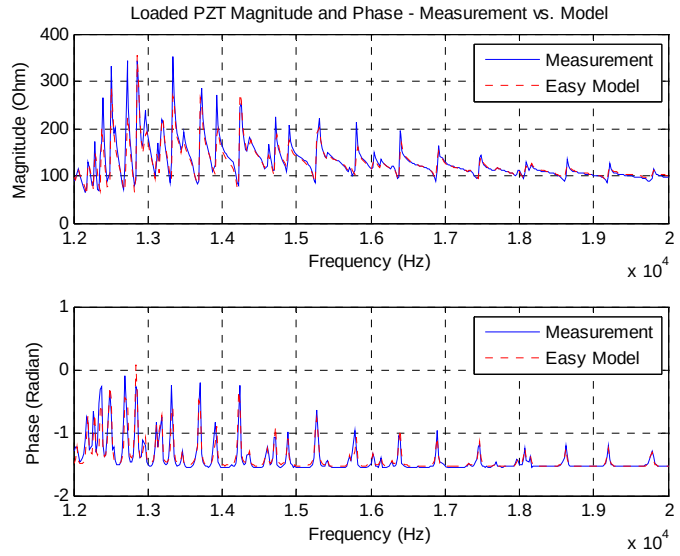

(b) Magnitude and Phase

Figure 3.15 Loaded PZT impedance comparison – Measurement vs. Easy Model

Table 3.3 Loaded PZT impedance comparison with 50 resonant frequencies – Correlation coefficients between Measurement and Easy Model

Impedance Component	Correlation Coefficient
Resistance	0.9743
Reactance	0.8888
Magnitude	0.9269
Phase	0.9409

The Easy Model for loaded PZT shown in Figure 3.13 is then verified with a loaded PZT with a damage on the structure. Through the same procedure, component values for loaded PZT with a damage to the structure are acquired. There are 38 resonant frequencies in the selected frequency range. The dotted lines in Figure 3.16 show the estimated impedance of the loaded PZT based on the Easy Model. From a visual inspection, the Easy Model follows the trends of the measured impedance of loaded PZT with a damaged structure. For a quantitative comparison, correlation coefficients between the measured impedance and the modeled impedance are calculated for resistance, reactance, magnitude and phase, separately as summarized in Table 3.4. The Easy Model estimates the loaded PZT impedance with an average agreement rate of 97%.

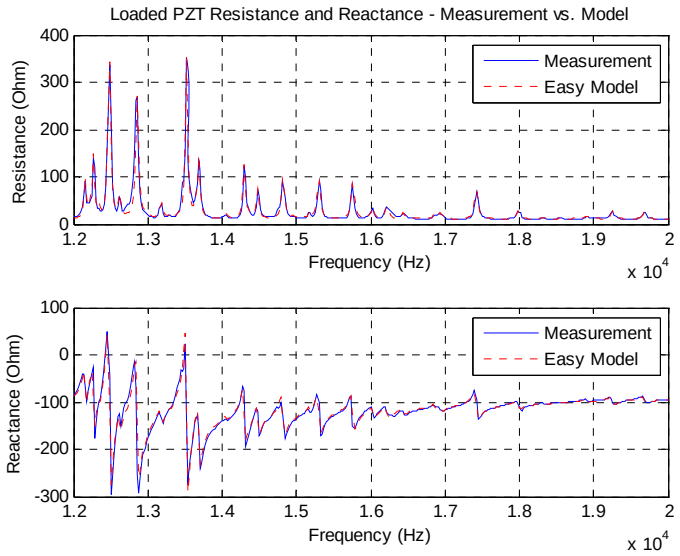

(a) Resistance and Reactance

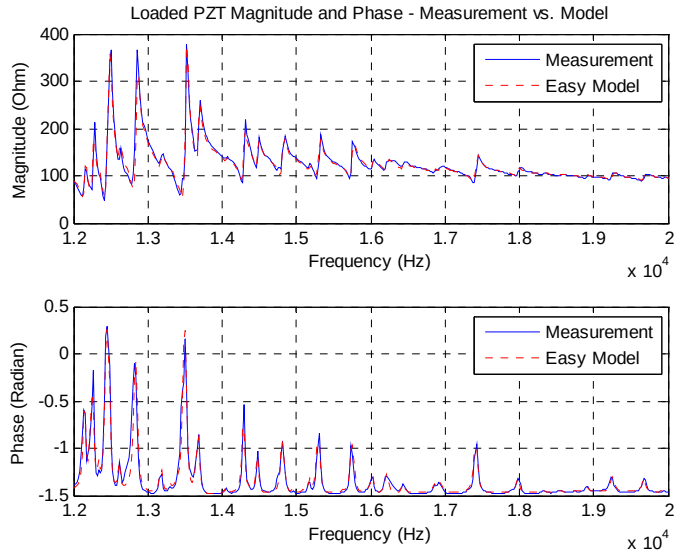

(b) Magnitude and Phase

Figure 3.16 Loaded PZT with damage impedance comparison – Measurement vs. Easy Model

Table 3.4 Loaded PZT impedance comparison with damage to the structure and with 38 resonant frequencies – Correlation coefficients between Measurement and Easy Model

Impedance Component	Correlation Coefficient
Resistance	0.9726
Reactance	0.9627
Magnitude	0.9738
Phase	0.9655

Based on the Easy Model accommodating multiple resonant frequencies, unloaded PZT estimation conducted in Section 3.3.2 is reconsidered to incorporate a local resonant frequency using the Easy Model illustrated in Figure 3.13, which was proposed for loaded PZT. By employing two RLC tank circuits, the estimated impedance has a higher degree agreement with the measured impedance as shown in Figure 3.17. Values of electrical components are summarized in Table 3.5, and calculated correlation coefficients for resistance, reactance, magnitude and phase are displayed in Table 3.6. The Easy Model estimates the unloaded PZT impedance with an average agreement rate of 100%.

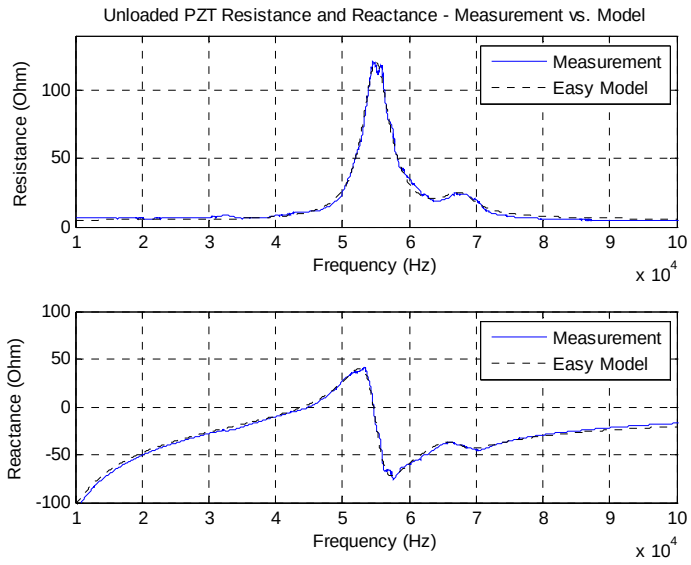

(a) Resistance and Reactance

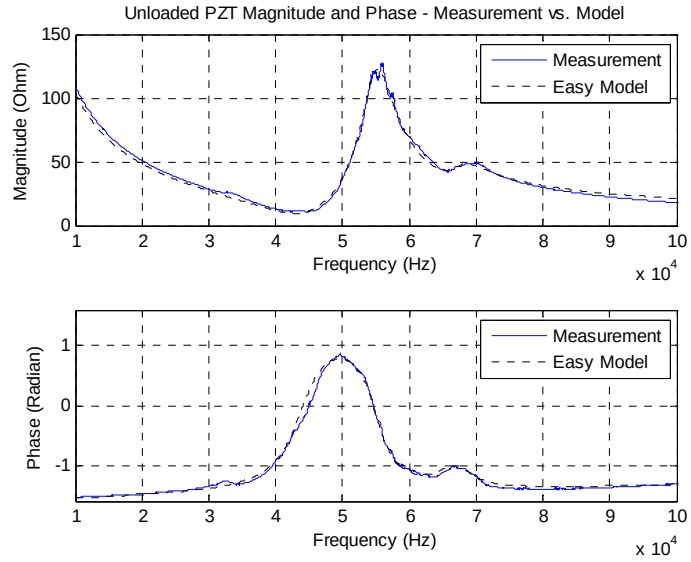

(b) Magnitude and Phase

Figure 3.17 Unloaded PZT impedance comparison with two resonant frequencies – Measurement vs. Model

Table 3.5 Unloaded PZT Easy Model circuit component values with two resonant frequencies

R_0 (Ω)	5	R_1 (Ω)	115	R_2 (Ω)	15
C_0 (μF)	0.15	C_1 (μF)	0.277	C_2 (μF)	1.727
		L_1 (μH)	30.253	L_2 (μH)	3.211

Table 3.6 Unloaded PZT impedance comparison with two resonant frequencies – Correlation coefficients between Measurement and Easy Model

Impedance Component	Correlation Coefficient
Resistance	0.9969
Reactance	0.9963
Magnitude	0.9958
Phase	0.9966

3.4 Concluding Remark

Since the Easy Model developed based on lumped elements is a linear system, the Easy Model can be used in a system level simulator to support high level system analysis and to accelerate performance evaluation procedure. The system level simulation and analysis using the Easy Model is covered in Chapter 6.

Chapter 4:
Wideband Method

4.1 Motivation

As covered in Section 2.3, there are two distinct approaches in developing compact autonomous SHM systems. The first approach is to develop a self-contained system that can process all operations of SHM with a system enclosing all hardware components and can provide the structural condition assessment result, which is just an indication of healthy or damaged to the end user. A good example is the prototype system implementing the Sinc Method explained in Section 2.3.3. The second approach is to develop an SHM system consisting of two separate physical parts; one part performs excitation and sensing at the actuator / sensor location, and the other part manages structural condition assessment at the user location. A long stream of sensed data is wirelessly transmitted from the actuator / sensor location to the user location. An example is the prototype system which realizes the Impedance-Chip Method described in Section 2.3.4. These two approaches are both claimed as autonomous SHM techniques, but the second approach relying on a separate computational unit at the user location is not an autonomous system in a rigorous sense. Therefore, this work focuses on the first approach, which pursues a self-contained autonomous SHM system.

As an improvement of the Low-Cost Method, the Sinc Method employs a DSP to perform operations of excitation signal generation and structural condition assessment, instead of relying on external equipment such as a signal generator and an FFT analyzer. For excitation and sensing, a DAC and an ADC are located at the input and output of the collocated actuator / sensor. Though the Sinc Method was a valuable attempt to realize an autonomous SHM system, and indeed made the first stand-alone SHM system possible, improvable factors still exist.

First, generation of the sinc wave excitation signal involves creation of multiple sine wave sequences with different frequencies and storage of a sinc wave sequence in memory. Consequently, complicated computation and large memory space are necessary and transmission of the excitation signal requires memory access. Second, the Sinc Method requires a DAC between the DSP and the PZT patch to provide an exact sinc waveform excitation signal to the structure. Excluding the DAC will shrink the form factor and lower the power dissipation. Third, the voltage divider actuator / sensor configuration provides a nonlinear structural response, which introduces a distortion to the damage metric. This work proposes the Wideband Method to address the first and second drawbacks of the Sinc Method, based on the fact that in the impedance-based SHM, the critical aspect of the excitation signal is the frequency range where the structure gets actuated, rather than the waveform of the excitation signal stimulating the structure. Additionally a linear excitation and sensing configuration is adapted to tackle the third drawback of the Sinc Method.

4.2 Basic Idea and Overall Architecture

The most important property of the excitation signal that should be maintained carefully is the frequency range. Structural health monitoring utilizes the frequency dependent interaction between the piezoelectric patch and the structure, and the structure has a unique frequency range where it is sensitive to the external excitation and damage. In a certain frequency range, the structure is highly responsive to the excitation, and the response alters in high degree upon damage to the structure. Therefore, as proved by the Sinc Method, the SHM system can detect damage if the frequency spectrum of the excitation signal is maintained as desired, regardless of the time domain excitation signal waveform. As we wanted to simplify the excitation signal generation algorithm, reduce the memory space required to store the excitation signal sequence, and remove the DAC from the SHM system, we adopt a digital wideband signal for structural excitation purpose.

The key idea of the Wideband Method is to use a digital wideband signal created by a pseudo noise sequence generator for structural excitation exploiting independency of impedance-based SHM on the excitation signal waveform. A PN sequence is a digital signal that occupies a certain frequency range in a frequency domain but has a random waveform in a time domain with a simple calibration. Thus, the PN sequence mitigates the computational complexity in generation of the excitation signal, excludes storage of the excitation signal in memory and memory access in sending out the excitation signal, and eliminates the DAC compared to the Sinc Method. These amendments resultantly reduce the power dissipation and decrease the SHM system dimension.

The Wideband Method, whose overall operation is illustrated in Figure 4.1, sends out an excitation signal to the actuator / sensor configuration and creates a structural response representing the electrical admittance of PZT. The waveform of the structural response is then detected, and an impedance signature is generated based on the structural response by an FFT operation, and the current impedance signature is compared with the baseline impedance signature, which is the first impedance signature stored as a reference representing the structural integrity. The impedance signature is a real part of the structural response after the FFT, which expresses the conductance of PZT. The comparison between the baseline and current impedance signature generates a damage metric, which is a quantity indicating structural integrity.

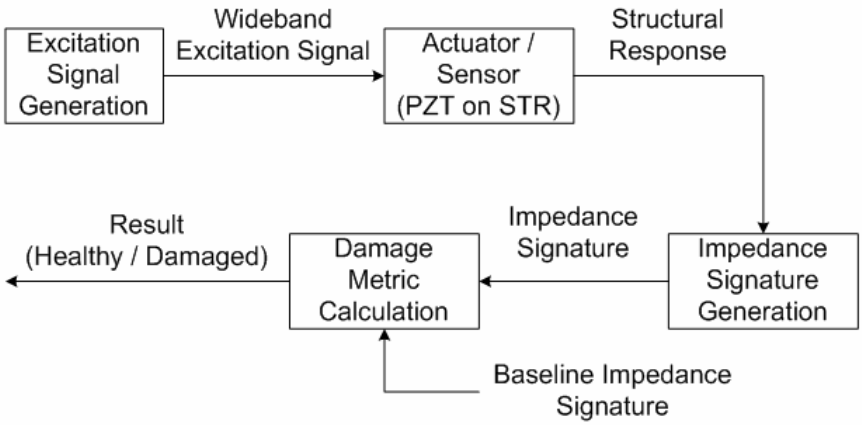

Figure 4.1 Wideband Method overall operation block diagram

As depicted in Figure 4.2, for a system development, the Wideband Method uses a DSP for excitation signal generation and structural condition assessment, and employs an inverting op amp configuration for excitation of the structure and sensing the structural response. Since the Wideband Method uses an FFT-based structural condition assessment, which has been accommodated in previous impedance methods including the Low-Cost Method and the Sinc Method, a *k*-bit ADC is placed between the excitation and sensing configuration and the DSP to detect the waveform of the structural response.

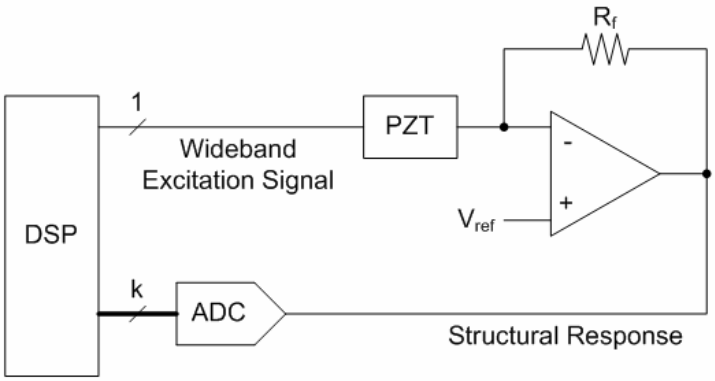

Figure 4.2 Wideband Method overall architecture

Unlike the sinusoidal and the sinc wave excitations, the proposed method does not require DAC, which is normally located in between a DSP and PZT in Figure 4.2. The proposed excitation method does not rely on any specific signal shape, but on noise-like signal behavior whose signal shape is not predictable in theory. The excitation and sensing block will be covered in detail later. The absence of the DAC clearly has advantage over the previous methods in regard to power dissipation.

4.3 Excitation Signal

A noise signal is generally used in direct sequence spread spectrum communication systems in order to spread the energy of the original signal into a much wider band [5][7]. An ideal noise signal, which is also called white noise, should be

random in a time domain and have a constant power spectral density in a frequency domain, but in reality white noise does not exist. Thus, a pseudorandom noise sequence is generally used in digital systems. A PN sequence is a sequence of binary numbers, which appears to be random but is in fact perfectly deterministic. A PN sequence is random in a certain length of the binary values, but the group of random binary sequence repeats, which is why the sequence is called PN sequence. A PN sequence can be generated utilizing a linear feedback shift register (LFSR), which is a shift register whose input bit is a linear function of its previous state. The only two linear functions of single bits are exclusive-OR (XOR) and inverse-XOR, thus the LFSR is a shift register whose input bit is determined by an XOR of some bits of the overall shift register values. The LFSR can be implemented in hardware as well as in software. The Wideband Method employs a PN sequence as a binary excitation signal with a wide bandwidth.

Let us consider a PN sequence, which is a binary discrete-time signal, $x[n]$, where n is the time index. The signal value $x[n]$ is either +1 or -1, and $x[n]$ has a sampling period of $T_{s,PN}$ as shown in the time domain signal of Figure 4.3 (a). The value of $x[n]$ is determined based on the sequence generated by a PN sequence generator. The discrete-time PN sequence $x[n]$ occupies a bandwidth as wide as the sampling rate $f_{s,PN}$, which equals to $1/T_{s,PN}$, around DC as shown in the magnitude response $|X(f)|$ of Figure 4.3 (b). The magnitude response $|X(f)|$ of the PN sequence spreads from the negative half of the sampling rate to the positive half of the sampling rate with an even symmetry, and appears at every harmonic of $f_{s,PN}$, as shown in Figure 4.3 (b). Therefore, the bandwidth of the target frequency range can be determined based on the sampling frequency $f_{s,PN}$ of a PN sequence, which is, in other words, the time domain resolution of the PN sequence $x[n]$.

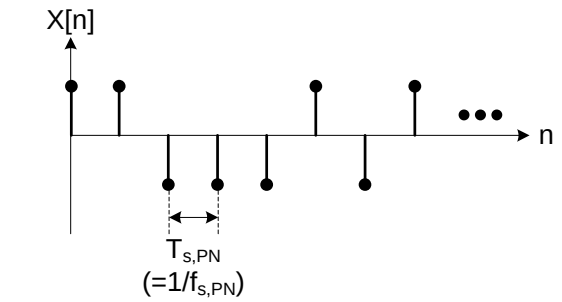

(a) Time domain

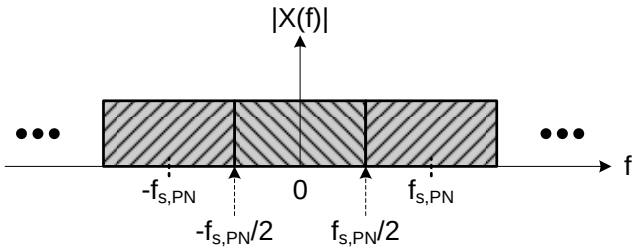

(b) Frequency domain

Figure 4.3 PN sequence in time domain and frequency domain

For further examination of the PN sequence, consider the frequency domain resolution. As shown in Figure 4.4, the PN sequence has a length of 2^N-*1*, which is the repetition period of the wideband excitation signal where *N* is the length of the LFSR of a PN sequence generator. After determining the excitation bandwidth, which is the same as the sampling frequency of the PN sequence $f_{s,PN}$, the frequency resolution of the excitation signal is decided as $f_{s,PN} \big/ \left(2^N - 1\right)$ by choosing the length of the PN sequence as 2^N-*1* as shown in Figure 4.4. Note that the magnitude response of the PN sequence is not perfectly constant unlike the white noise because the PN sequence is not an ideal noise signal and has a periodicity in its sequence.

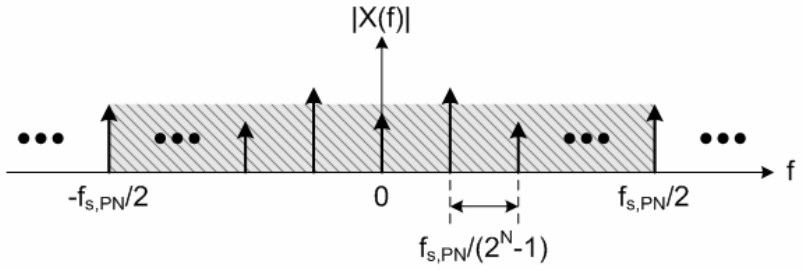

Figure 4.4 Frequency resolution of a PN sequence

Since, typically, the target frequency range is positioned at several tens of KHz, the frequency range of a generated PN sequence needs an up-conversion. Considering a target frequency range centered at f_c, the spectrum of a baseband PN sequence should be translated upward in a frequency domain to locate the center frequency of the up-converted PN sequence at f_c. An easy way to translate the spectrum of a baseband signal to a higher frequency is to multiply or heterodyne the baseband signal with a carrier signal as shown in Figure 4.5 [7]. When the carrier signal $c(t)$ is $\cos(2\pi f_c t)$, a modulated signal or a bandpass signal $m(t)$ becomes $x(t)\cdot\cos(2\pi f_c t)$ and the spectrum $|M(f)|$ consists of two copies of $|X(f)|$ at f_c and $-f_c$ as shown in Figure 4.6.

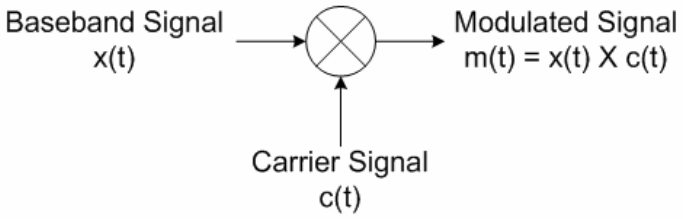

Figure 4.5 Frequency up-conversion

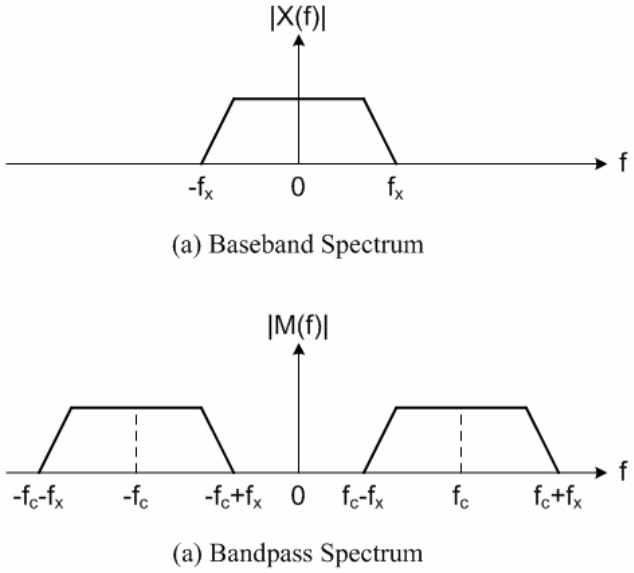

Figure 4.6 Baseband and bandpass signal spectrums [7]

In case of the Wideband Method, all signals involved in the excitation signal generation are discrete in a time domain, and a digital up-converting technique should be applied. Thus, the carrier signal is a sequence of alternating 1 and -1 with a sampling period of T_c (=1/f_c), as shown in Figure 4.7 (a), where f_c is the center frequency of the target frequency range. The spectrum of carrier sequence contains two delta functions at f_c and $-f_c$.

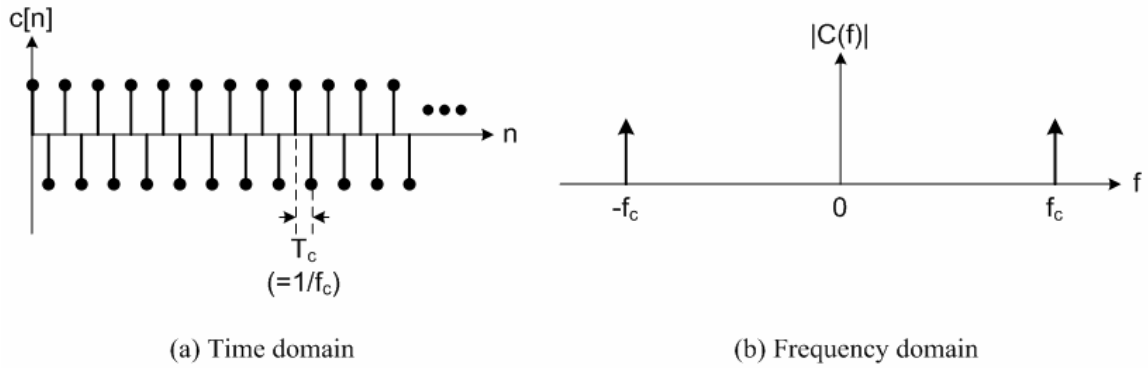

Figure 4.7 Carrier signal in time domain and frequency domain

To multiply the carrier sequence $c[n]$ to the PN sequence $x[n]$, the sampling periods of those two sequences should be matched. Since the carrier sequence has higher sampling frequency, the PN sequence is up-sampled before multiplication as shown in Figure 4.8. Upon up-sampling of the PN sequence, as shown in Figure 4.8 (b), each sample $x[i]$ of the PN sequence creates a sequence $y[k \cdot i] \sim y[k \cdot (i+1) - 1]$ that can be considered as a square waveform after a zero-order hold, where k is the up-sampling ratio as $k = f_c / f_{s,PN}$. Since the spectrum of a square wave is a sinc function, the spectrum of the up-sampled PN sequence $|Y(f)|$ has the envelope of a sinc function. As noted in Figure 4.4, the spectrum of PN sequence is not perfectly flat, and consequently the spectrum of up-sampled PN sequence is also not a perfect sinc function. Thus, spectrums $|X(f)|$ and $|Y(f)|$ shown in Figure 4.8 illustrate envelopes of actual spectrums.

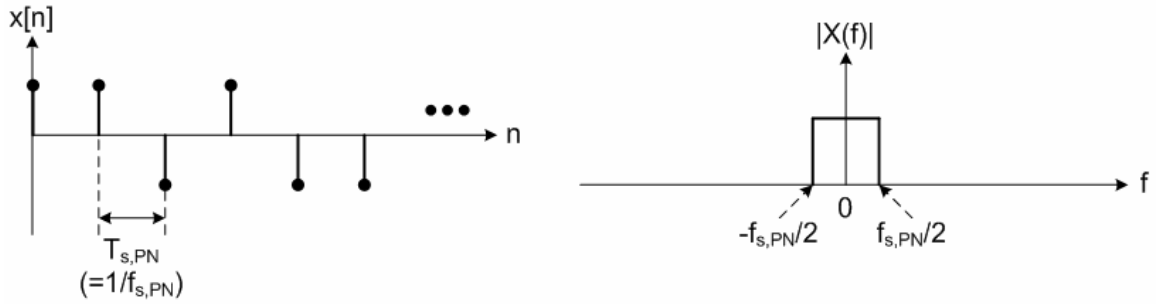

(a) PN sequence

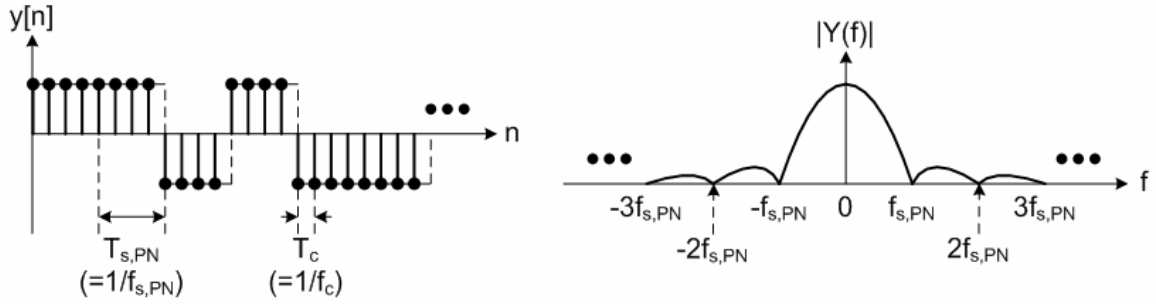

(b) Upsampled PN sequence

Figure 4.8 PN sequence up-sampling

The up-sampled PN sequence $y[n]$ is finally multiplied with the carrier sequence $c[n]$ to create the desired wideband excitation sequence $m[n]$ as shown in Figure 4.9 (a). As illustrated in Figure 4.9 (b), the spectrum of created excitation sequence $|M(f)|$ covers the target frequency range centered at f_c with an approximated 3-dB bandwidth of $f_{s,PN}$.

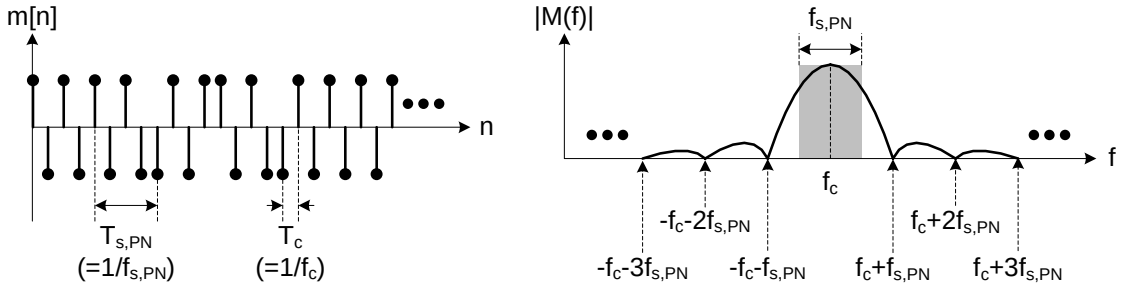

(a) Time domain (b) Frequency domain

Figure 4.9 Resulting wideband excitation signal

Since the PN sequence occupies a limited bandwidth, the digital up-converting technique brings the baseband PN sequence up to certain center frequency, which is determined by an alternating digital carrier sequence. The procedure of wideband excitation signal generation is summarized in Figure 4.10.

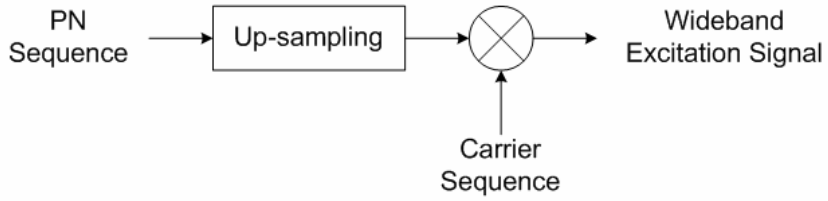

Figure 4.10 Digital wideband excitation signal generation procedure

4.4 Sensor Actuation and Sensing

The actuator / sensor configuration employed in the Low-Cost Method and the Sinc Method is a voltage divider configuration that uses a sensing resistor connected to the piezoelectric patch in series as shown in Figure 4.11. In the Low-Cost Method and the Sinc Method, this voltage divider configuration is located between the DAC and the ADC, so that V_{in} is the excitation signal from the DAC and V_{out} is the structural response into the ADC.

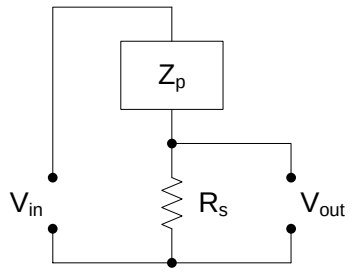

Figure 4.11 Actuator / Sensor Configuration – Voltage Divider

The voltage divider configuration was proposed in the Low-Cost Method to replace an expensive and bulky impedance analyzer in developing an impedance-based SHM system [10]-[12]. The piezoelectric patch bonded to the structure is excited with a voltage input V_{in}, and the response through the structure is sensed via a sensing resistor R_s in terms of a voltage V_{out}. The relationship between the input excitation V_{in} and the structural response across the sensing resistor V_{out} is

$$V_{out} = \frac{R_s}{R_s + Z_p} V_{in} \tag{4.1}$$

where R_s is the resistance of the sensing resistor and Z_p is the electrical impedance of the piezoelectric patch bonded to the structure. Since the purpose of impedance-based SHM is to detect damage to a structure by observing any changes on the impedance of the structure, it is important to clearly catch variations on the impedance, rather than the impedance itself, of the piezoelectric patch through measuring the sensed voltage V_{out}.

When the electrical impedance of the piezoelectric patch Z_p is much greater than the resistance of the sensing resistor R_s ($Z_p / R_s >> 1$), equation (4.1) can be simplified as

$$V_{out} = \frac{1}{1 + \frac{Z_p}{R_s}} V_{in} \approx \frac{R_s}{Z_p} V_{in} = R_s \frac{V_{in}}{Z_p} = R_s I_p \tag{4.2}$$

where I_p is the current through the piezoelectric patch. Thus, the voltage across the sensing resistor V_{out} is proportional to the current through the piezoelectric patch attached to the structure, and consequently V_{out} effectively indicates changes on the electrical admittance of the piezoelectric patch, which represents the mechanical admittance of the structure. In this case, as the size of a sensing resistor R_s is considered to be very small, the voltage divider configuration can have a problem of large ADC quantization noise. Though variations on the sensed voltage V_{out} is an approximation of the variation on the structure's admittance, too small sensing resistor R_s shrink the variation range of V_{out} and results in a structural response dominated by an ADC quantization noise.

On the other hand, when the sensing resistor size R_s is large enough to make the sensed voltage V_{out} overcome the ADC quantization noise, the relationship between the excitation voltage V_{in} and the sensed voltage V_{out} expressed in equation (4.1) cannot be simplified to equation (4.2). As shown in equation (4.1), V_{out} loses its linear relationship to the admittance of the structure with the growth of R_s. Thus, the sensed voltage Vout cannot represent variations on the admittance of the structure linearly, though V_{out} still approximates admittance of the structure.

Based on the impedance measurement data of the Sinc Method [13][14], changes on the admittance cased by damage vary approximately from 10Ω to 560Ω within the damage-sensitive frequency range (10 KHz ~ 20 KHz), and it makes the sensed voltage V_{out} nonlinear to the variation of Z_p depending on the size of R_s. Figure 4.12 shows the variation on the sensed voltage V_{out} according to the actual changes on the structure's admittance. The independent axis values are taken from the actual admittance measurement, and the dependent axis values are calculated from equation (4.2). The

sensing resistor values are varied from 1Ω to 200Ω, and 47Ω is the value used in the prototype [13][14]. As we can observe, small sensing resistor value (1Ω) provides a linear-like relationship between the actual admittance Z_p variation and the sensed voltage V_{out} changes. However, the voltage gain obtained with 1 Ω sensing resistor is very small (1/560 in the worst case), it resultantly provides low sensitivity to the damage due to the domination by quantization noise in ADC. As the value of the sensing resistor is increased, the nonlinearity of the indicator to the PZT impedance variation becomes severe, so it becomes more difficult to adjust the size of R_s in terms of the different impedance range for the various structural materials.

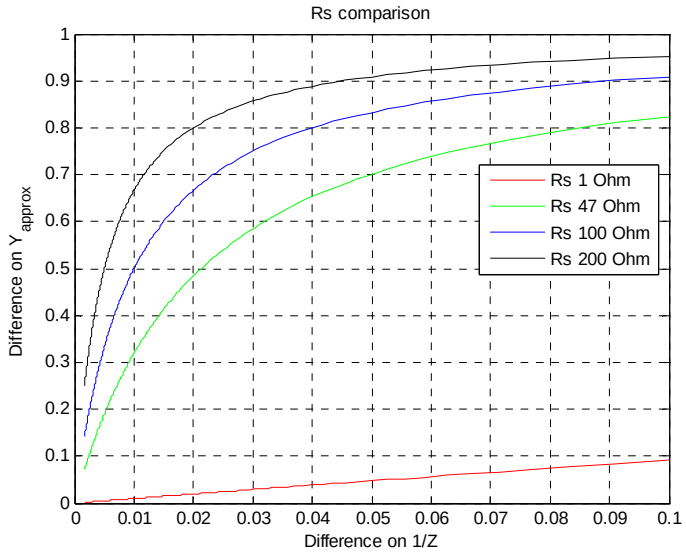

Figure 4.12 Detection performance comparison with different sensing resistor values with traditional low cost impedance based method

To address a nonlinear problem, the Wideband Method employed an inverting op amp configuration for an actuator / sensor configuration as shown in Figure 4.13. In an inverting op amp configuration, the generated excitation signal is directed to the piezoelectric patch, so that the PZT is excited with a rather clean and stable rectangular pulse with less unexpected frequency components. This configuration was also used in Analog Devices impedance measurement chip [56].

The op amp's output signal, which is the structural response through the piezoelectric patch, is linearly proportional to the admittance of the PZT as shown in equation (4.3).

$$v_{sense}(t) \approx -\frac{R_f}{Z_{PZT}} v_{excite}(t) \tag{4.3}$$

Z_{PZT} indicates the impedance of PZT, and R_f denotes the feedback resistor. v_{excite} and v_{sense} are the output voltage from the DSP through a buffer and the input voltage to the comparator, respectively.

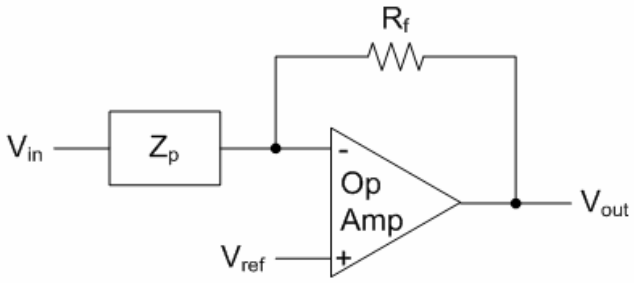

Figure 4.13 Actuator / Sensor Configuration – Linear Response

4.5 Structural Condition Assessment

Structural condition assessment of the Wideband Method includes analog-to-digital conversion, impedance signature generation, and damage metric calculation as illustrated in Figure 4.14.

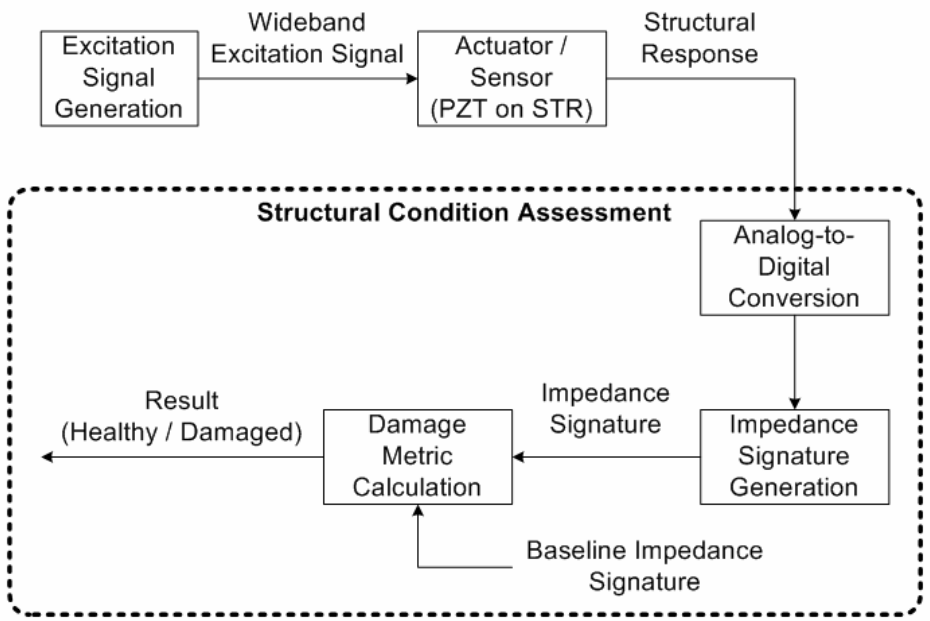

Figure 4.14 Structural condition assessment operation block diagram

The proposed Wideband Method adopts an FFT-based structural condition assessment technique, which was used by all previous impedance-based SHM methods including the traditional impedance-based method, the Low-Cost Method, the Sinc Method, and the Impedance-Chip Method. The FFT-based structural condition assessment first records the structural response through an ADC in a time domain. The time domain structural response is recorded several times for an average to mitigate the noise effect on the structural response. The averaged time domain structural response is converted into a frequency domain through FFT, and a real part of the FFT result is taken to create an impedance signature. An impedance signature is a frequency domain representation of the structural response that varies depending on the structure's mechanical impedance, and the first signature, called a baseline, is stored as a reference. The baseline impedance signature is compared with upcoming signatures instantaneously under an assumption that the structure is initially intact to calculate a damage metric. Since the structural response, which is an output of the actuator / sensor configuration, is proportional to an electrical admittance of PZT, the impedance signature represents the conductance of PZT.

The damage metric used in the Wideband Method is a RMSD between baseline and instantaneous impedance signatures normalized to the mean of the absolute baseline signature. The damage metric indicates how much the freshly measured impedance deviates from the reference. The expression of the damage metric is

$$RMSD = \frac{\sqrt{\frac{\sum_{m=1}^{M}\left(G_{base}(m) - G_{curr}(m)\right)^2}{M}}}{\frac{\sum_{m=1}^{M} abs\left\{G_{base}(m)\right\}}{M}} \tag{4.4}$$

where G_{base} is the baseline impedance signature, G_{curr} is the current impedance signature, and M denotes the number of frequency components in the target frequency range. Notice that the RMSD represented in equation (4.4) is not a mathematical RMSD. It is a mathematical RMSD value normalized by a baseline signature.

Finally, the damage metric is compared to a preset threshold value to determine if the structure has been damaged. When the structure stays in a healthy state, the variation on the RMSD value will remain under a certain threshold level. Upon occurrence of damage to the structure, the fresh impedance signature diverges from the baseline. Therefore, the RMSD value increases, and the system indicates damage to an end user if the RMSD value exceeds the pre-determined threshold level.

4.6 Performance Analysis

4.6.1 Prototype Development

To verify the operation and evaluate the performance of the Wideband Method, a prototype system is developed. The Wideband Method requires a DSP that can perform excitation signal generation and structural condition assessment, an ADC, and some external circuitry to compose an actuator / sensor block. The prototype system is mainly assembled from a TMS320C6713 DSP EVM, and an ADS8364 ADC EVM as shown in Figure 4.15. Each EVM is stackable and connected via general purpose ports. In

addition to the DSP and ADC, there is one more IC device involved for PZT excitation and sensing operation. The excitation and sensing operation requires one buffer as well as an op amp. A dual-channel op amp TLV2772 from Texas Instruments is employed to implement a buffer and an op amp [36]. Some miscellaneous components, such as resistors and an LED, are also included.

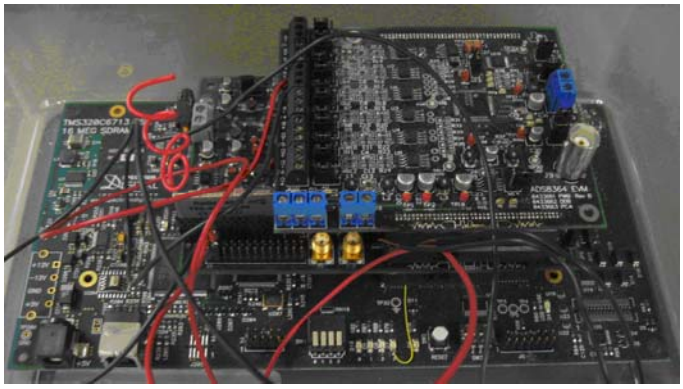

Figure 4.15 Evaluation system

4.6.2 Test Structure and Preliminary Measurements

A test structure used in experiments is an aluminum beam with a PZT patch bonded to one end as shown in Figure 4.16 (a). In the experimental setup, a damage to the structure is simulated by applying two magnets to either side of the beam as an added weight and pressure to the structure [58][59]. Using magnets attracted through the beam thickness direction, the damage is non-permanent and repeatable. The magnets are applied to near, center, and far locations with respect to the PZT patch, and the exact damage locations along with detail dimensions of the test structure are illustrated in Figure 4.16 (b).

(a) Structure with a damage

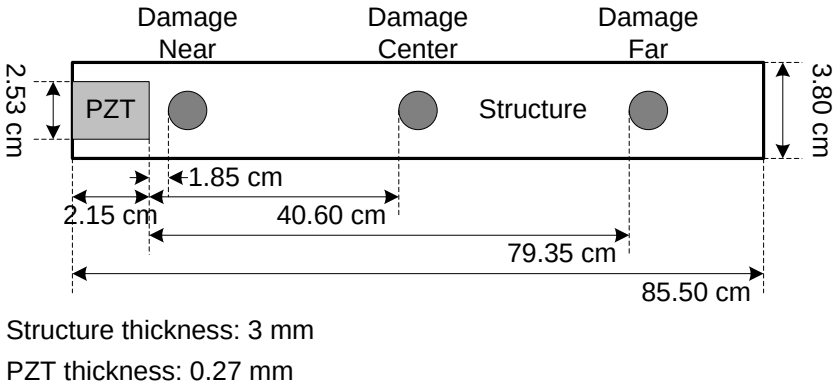

(b) Test scenario and dimension

Figure 4.16 Test structure

Before evaluating the performance with the prototype, a preliminary measurement is performed to determine the target frequency range as well as to evaluate the characteristics of the structure and damage. The impedance measurement frequency range is from 100 Hz to 100 KHz with a frequency step size of 10 Hz, and an HP 4194A impedance analyzer performs the impedance measurement of the PZT bonded to the structure. Measurements are taken on both healthy and damaged structures with damage locations seen in Figure 4.16 (b). To alleviate noise effects, 35 measurements were taken, and the maximally occurring value was selected at each frequency through a histogram analysis. Values of resistance, the real parts of the measured impedance, are shown with four different structural conditions in Figure 4.17. After analysis, it is observed that the frequency range from 12 KHz to 20 KHz is highly sensitive to excitation, and damage at each of the locations alters the resistance at certain frequencies by arbitrary amounts.

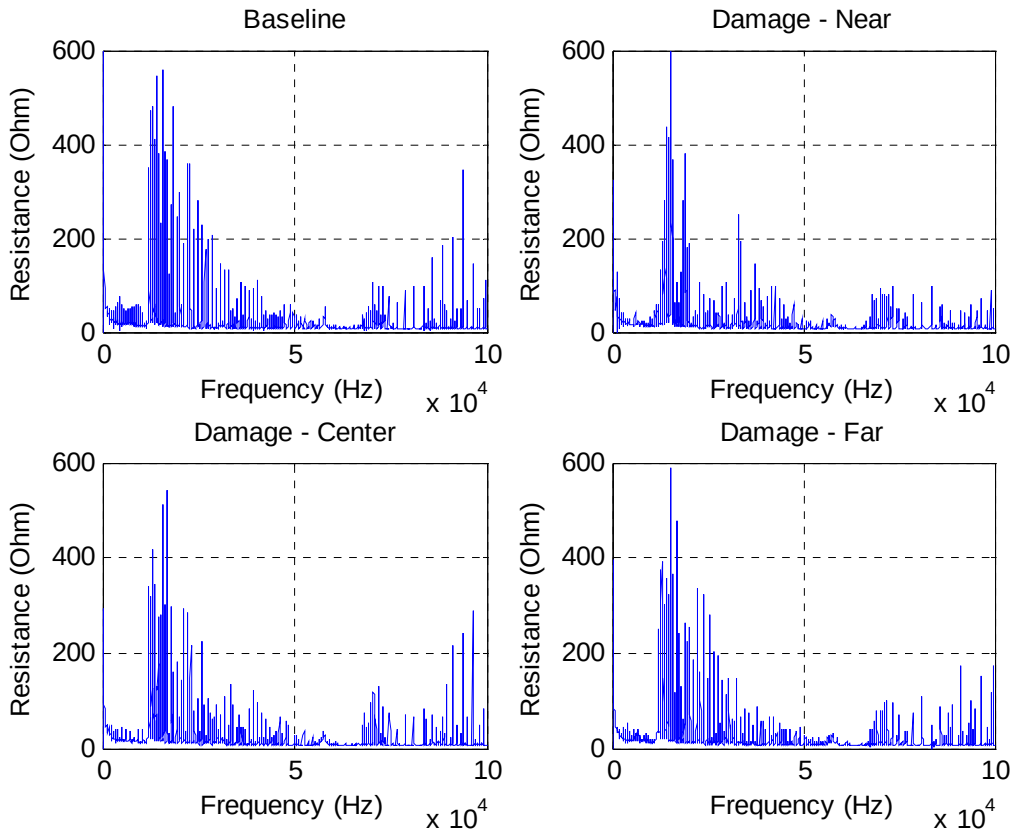

Figure 4.17 Measured impedance at different structural conditions

Based on this measured impedance, an experiment using the prototype system shown in Figure 4.15 has been performed with the following specifications: The target frequency range is from 12 KHz to 20 KHz, where the structure is highly sensitive to the excitation, and the frequency resolution within the detection frequency range is 125 Hz by choosing the length of PN sequence as 64. The excitation digital wideband signal is produced by being up-converted at a center frequency of 16 KHz, and the actual excitation signal through a buffer at the output of the DSP occupies approximately 10 dB bandwidth within the target frequency range as shown in Figure 4.18. An Anritsu MS2665C performed spectrum analysis of the resulting digital wideband excitation signal.

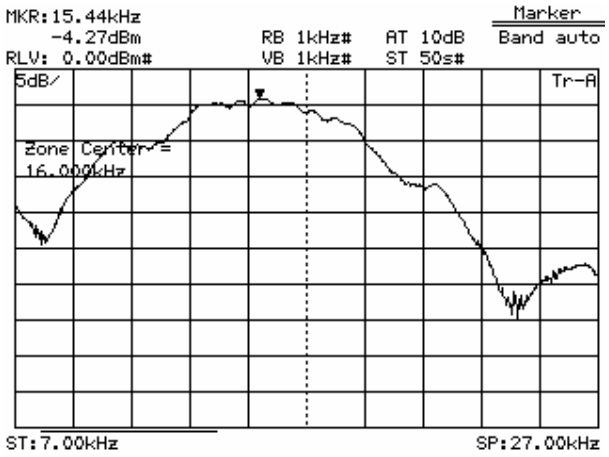

Figure 4.18 Digital wideband excitation signal in frequency domain

4.6.3 Performance

As summarized in Table 4.1, the comparison of the measured RMSD values for the Wideband Method, the traditional impedance-based method, and the Sinc Method clearly indicates that the proposed digital wideband excitation method reveals the structural defects to a higher degree. The trend in damage metrics with different damages from the Wideband Method exactly follows that of the traditional impedance-based method, while the Sinc Method has a weaker distinction of damage compared to the traditional impedance-based method. This improved performance is due to positive gain and the linear response to the variation of the PZT relying on an inverting op amp excitation and sensing configuration as discussed in Section 4.4. One can notice that the RMSD values measured with the sinc wave excitation method are very small, so that quantization noise added by an ADC and the limited numbering resolution in a DSP can affect the detection performance.

Table 4.1 Damage detection performance comparison

Damage Location	Wideband Method	Traditional Impedance-Based Method	Sinc Method
Near	1.6734	1.6111	1.2173
Center	1.2622	1.2225	1.0494
Far	1.0000	1.0000	1.0000

The most significant advantage of the proposed wideband excitation technique over the previous sinusoidal or sinc wave excitation methods is the power reduction due to the elimination of the DAC. This decrease in power dissipation is achieved with an improvement on the performance. As summarized in Table 4.2, the power consumed by the DAC, which was 17% of the total power dissipation in the prototype of the Sinc Method [14], can be completely removed. Also worth mentioning are two other affiliated advantages: lower hardware complexity and decreased memory requirement. A byproduct of using a digital excitation signal is that less memory is required as compared to sinc wave excitation. The sinc wave excitation method should store at least one period of the pre-calculated excitation signal in memory, and each excitation sample requires multiple bits as small as a resolution of the DAC to represent the exact signal voltage level. Furthermore, the reduced bus width, which is a result of not needing a DAC in the proposed wideband method, simplifies the system complexity in addition to the power benefits.

Table 4.2 Power dissipation comparison

Component	Power Dissipation (W)	
	Sinc Method [14]	Wideband Method
DSP	1.58	1.58
DAC	0.75	N/A
ADC	1.68	1.68
Total	4.01	3.26

Chapter 5:
Binary Method

5.1 Motivation

The Wideband Method that employs a binary wideband excitation signal circumvents reliance on a DAC, simplifies the algorithm for excitation signal generation, and relaxes the memory requirements on storing the excitation signal. An actuator / sensor configuration applied to the Wideband Method is an inverting op amp configuration that provides a linear structural response as opposed to a voltage divider configuration. Resultantly, the Wideband Method achieves a smaller hardware form-factor, lower power dissipation, and a more precise impedance signature compared to the Sinc Method. However, the Wideband Method performs a traditional FFT-based structural condition assessment utilizing the waveform of the structural response, and extracts the resistance of PZT to create an impedance signature. Thus, the Wideband Method requires an ADC at the receiver front-end of a core computation unit, and high computational power with a large memory space for the core computation unit itself to support FFT operation. This work examines properties of the electrical admittance of the PZT bonded to the structure in order to establish a breakthrough structural condition assessment methodology that can exclude FFT operation and lead to a compact and low-power consuming SHM system.

As discussed in Section 2.3.1, traditional FFT-based structural condition assessment employs the conductance of PZT as an impedance signature, and the damage metric exploits the deviation of the current impedance signature from the baseline impedance signature in terms of RMSD. Hence, when redefining the electrical admittance of PZT expressed in equation (2.2) as $Y_p = G_p + jB_p$, baseline impedance signature as $G_{p,base}$, and current impedance signature as $G_{p,curr}$, the difference between

baseline and current impedance signatures, $G_{p,base} - G_{p,curr}$, becomes the major quantity indicating the significance of damage. Let us name the impedance signature difference $G_{p,base} - G_{p,curr}$ as a damage indicator. Thus, if the damage indicator can be estimated in a simpler way without actually calculating the conductance of PZT through an FFT operation, the computational complexity of structural condition assessment can be decreased.

As $G_p = B_p / \tan\phi_p$, where ϕ_p is the phase of Y_p,

$$\begin{aligned} G_{p,base} - G_{p,curr} &= \frac{B_{p,base}}{\tan\left(\phi_{p,base}\right)} - \frac{B_{p,curr}}{\tan\left(\phi_{p,curr}\right)} \\ &= \frac{B_{p,base}\tan\left(\phi_{p,curr}\right) - B_{p,curr}\tan\left(\phi_{p,base}\right)}{\tan\left(\phi_{p,base}\right)\cdot\tan\left(\phi_{p,curr}\right)} \\ &= \frac{B_{p,base}\sin\left(\phi_{p,curr}\right)\cdot\cos\left(\phi_{p,base}\right) - B_{p,curr}\cos\left(\phi_{p,curr}\right)\cdot\sin\left(\phi_{p,base}\right)}{\sin\left(\phi_{p,base}\right)\cdot\sin\left(\phi_{p,curr}\right)} \end{aligned} \tag{5.1}$$

Since the susceptance B_p has less variation to damage on the structure compared to the conductance G_p [20], $B_{p,curr}$ can be approximated as $B_{p,curr} \approx B_{p,base}$. Thus,

$$G_{p,base} - G_{p,curr} \approx B_{p,base}\frac{\sin\left(\phi_{p,curr} - \phi_{p,base}\right)}{\sin\left(\phi_{p,base}\right)\cdot\sin\left(\phi_{p,curr}\right)} \tag{5.2}$$

Since $B_{p,base}$ and $\sin\left(\phi_{p,base}\right)$ are constant for any instantaneously measured $Y_{p,curr}$ regardless of the existence of damage on the structure, $B_{p,base}$ and $\sin\left(\phi_{p,base}\right)$ are ignorable in a damage indicator. Thus, equation (5.2) can be further simplified as

$$G_{p,base} - G_{p,curr} \propto \frac{\sin\left(\phi_{p,curr} - \phi_{p,base}\right)}{\sin\left(\phi_{p,curr}\right)} \tag{5.3}$$

Note that $\sin\left(\phi_{p,curr}\right)$ is close to one because PZT is mostly capacitive, which makes the admittance phase of PZT close to $\pi/2$, and $\sin\left(\phi_{p,curr} - \phi_{p,base}\right)$ becomes the dominant quantity indicating the damage. Therefore, the phase difference $\phi_{p,curr} - \phi_{p,base}$ is a strong

candidate proportional to the traditional damage indicator $G_{p,base} - G_{p,curr}$ used in FFT-based structural condition assessment.

To verify the suitability of an admittance phase difference instead of a conductance difference as a damage indicator, the impedance of a PZT patch bonded to a test structure is measured using an impedance analyzer, HP 4194A, without and with damage. The test structure is an aluminum beam, and two magnets are used to simulate damage by applying pressure to the structure as shown in Figure 5.1. Figure 5.1 (a) shows the top view of the test structure with a PZT patch and the top magnet, and Figure 5.1 (b) shows the side view. *M* indicates a cylindrical magnet in Figure 5.1.

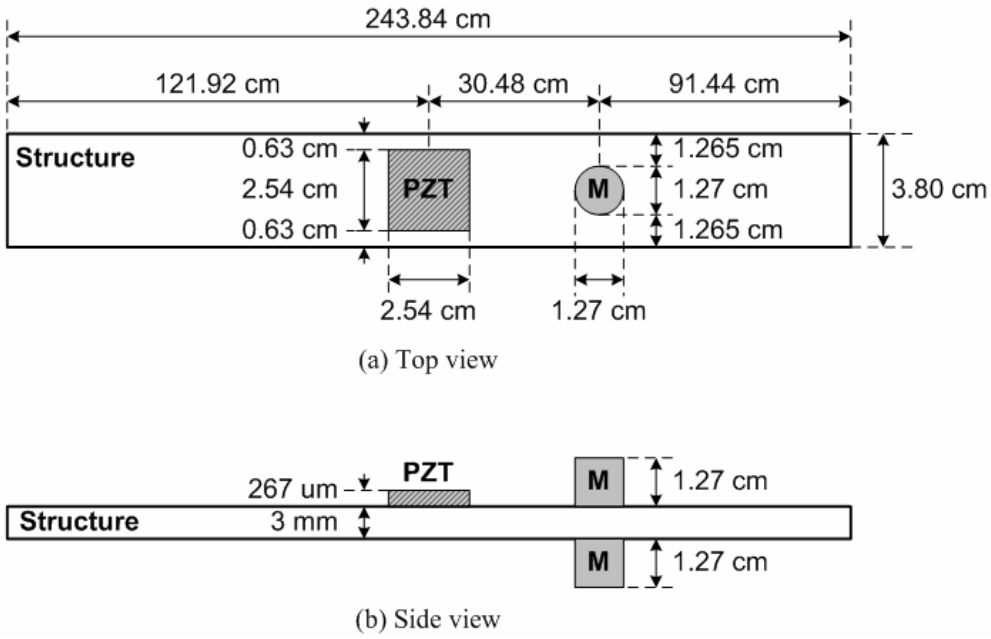

Figure 5.1 Test structure with two magnets as a simulated damage (not to scale)

As shown in Figure 5.2, the waveforms of the admittance phase follow those of the conductance either without damage, which is denoted as Baseline, or with damage, which is denoted as Damage.

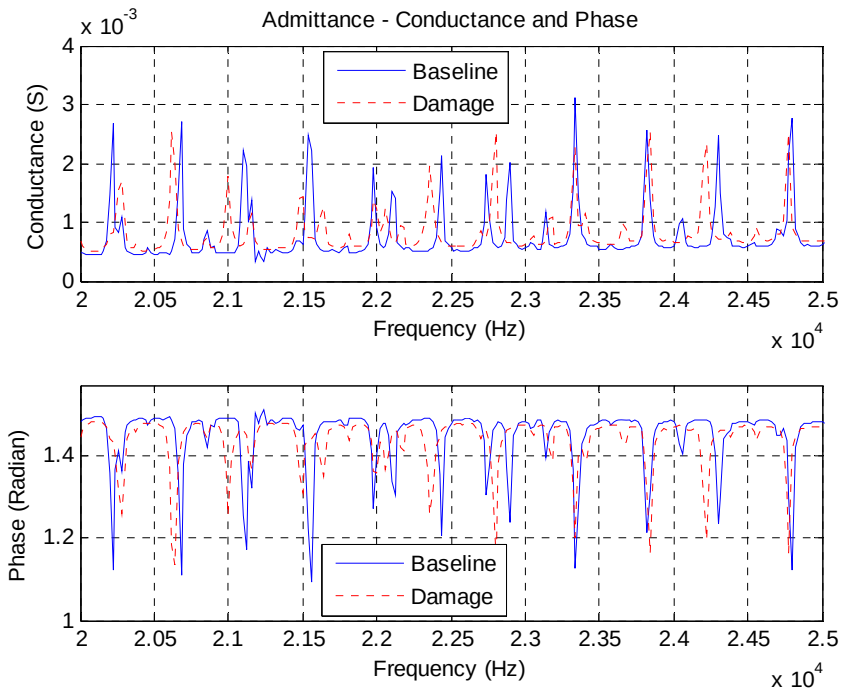

Figure 5.2 Conductance and phase of the admittance with / without damage

The traditional damage indicator $G_{p,base} - G_{p,curr}$ and the proposed damage indicator $\phi_{p,curr} - \phi_{p,base}$ are compared in Figure 5.3 for the case with damage. It is manifest that the proposed damage indicator, which is the phase difference, is proportional to the traditional damage indicator, which is the conductance difference. The correlation coefficient between the traditional and the proposed damage indicators is 0.7495. Therefore, it is confirmed that structural condition assessment relying on the admittance phase difference has a chance to replace the traditional FFT-based structural condition assessment depending on the conductance difference, if the excitation signal is altered appropriately to support the measurement of an admittance phase of PZT.

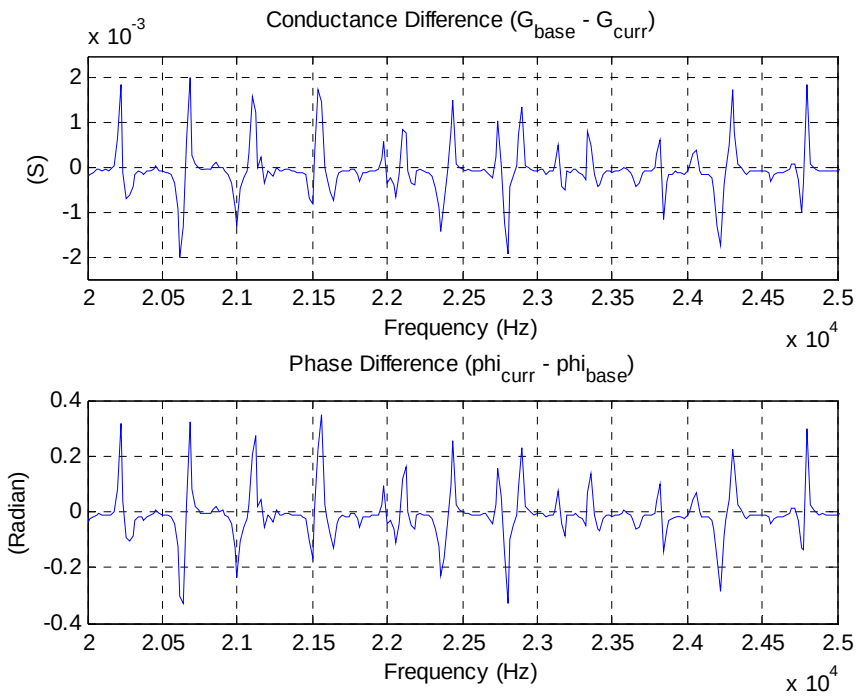

Figure 5.3 Difference between admittances with / without damage – conductance and phase

5.2 Basic Idea and Overall Operation

As a further improved method to develop an autonomous impedance-based SHM system than the Wideband Method discussed in Chapter 4, a new method is expected to be capable of circumventing the reliance on an ADC and possibly of decreasing the computational complexity, while keeping a DAC outside of the picture. Thus, this work proposes a new method for performing impedance-based SHM, the Binary Method. As demonstrated in the name, the Binary Method excites the structure with a binary excitation signal and measures the structural response in a binary format, both of which become feasible by embracing the admittance phase difference as a major damage indicator.

The Binary Method, whose overall operation is illustrated in Figure 5.4, uses a rectangular pulse train, which resembles a clock signal, as an excitation signal, and excites the structure with one frequency at a time by changing the frequency of the rectangular pulse train at regular time intervals. The rectangular pulse train excitation

signal passes through the actuator / sensor configuration and creates a structural response representing the electrical admittance of PZT. The voltage level of the structural response from the actuator / sensor configuration is compared with a reference voltage, which is an average of the high and low voltages of the excitation signal, to represent the structural response in a binary format. The binary structural response is compared with the binary excitation signal to obtain the amount of phase shift through an actuator / sensor configuration and a comparator, which mainly represents the PZT admittance phase and is used to calculate an impedance signature. The baseline impedance signature, which is the first impedance signature generated at the beginning of the SHM operation, is stored as a reference, and the upcoming impedance signatures are compared with the baseline signature to calibrate a damage metric for structural condition assessment.

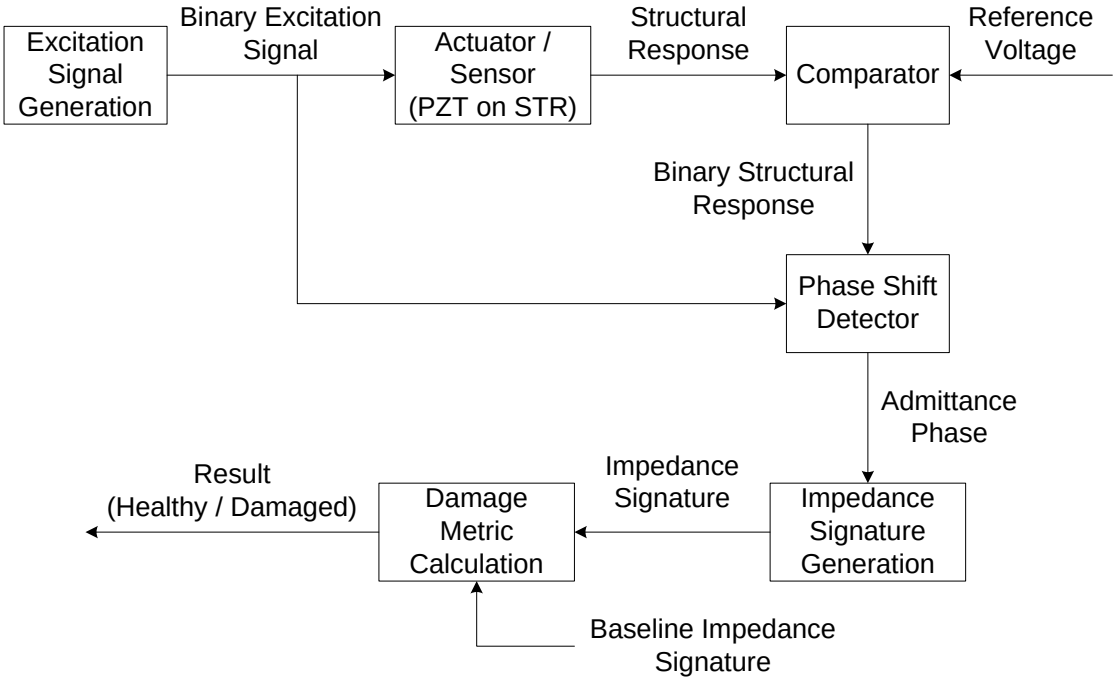

Figure 5.4 Binary Method overall operation block diagram

As depicted in Figure 5.5, in system development, an inverting op amp configuration used in the Wideband Method is employed as an actuator / sensor configuration in the Binary Method again. The rectangular pulse train is generated by a

pulse width modulation (PWM) signal generator included in a DSP (or a microcontroller), and the phase shift through an inverting op amp configuration and a comparator is detected by an XOR operation. A DSP (or a microcontroller) also performs impedance signature generation and damage metric calculation. Details of each operation are covered in the following subsections.

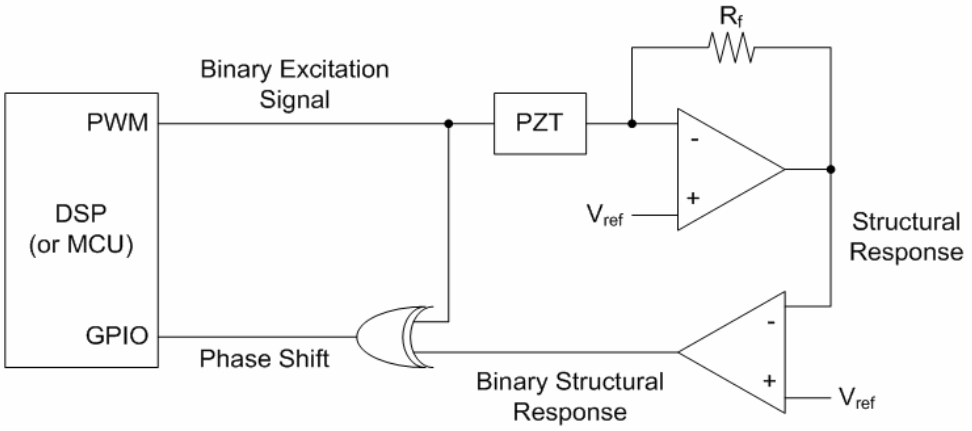

Figure 5.5 Binary Method overall architecture

5.3 Excitation Signal

5.3.1 Rectangular Pulse Train

The Binary Method exploits a simple binary rectangular pulse train in order to excite the structure. Let us first consider a rectangular pulse as shown in Figure 5.6. Figure 5.6 (a) shows the waveform of a rectangular pulse $r(t)$ with a period of T_0 and 50 % duty cycle in time domain, and the magnitude response of $r(t)$, which is $|R(f)|$, is presented in Figure 5.6 (b). The magnitude response of a rectangular pulse $|R(f)|$ has a main lobe peak around f_0 (=1/T_0), and side lobes at odd integer multiples of f_0, while the magnitude at even integer multiples of f_0 becomes zero.

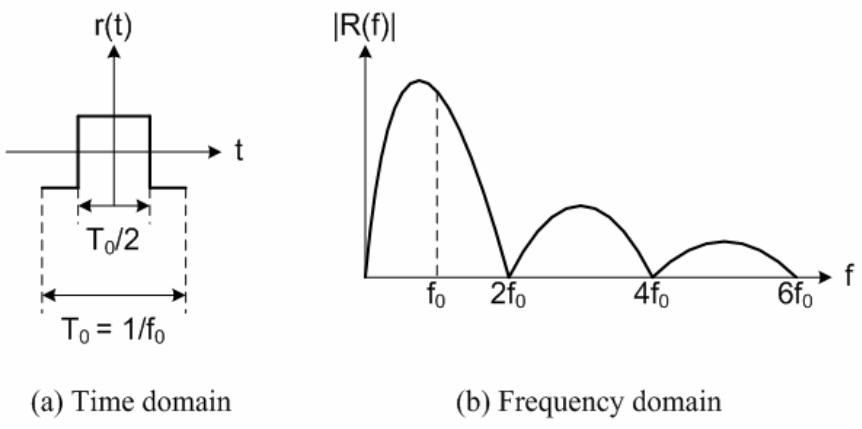

Figure 5.6 A rectangular pulse in the time and frequency domains

As a second step to generate an excitation signal, consider the repetition of a rectangular pulse to create a rectangular pulse train. Figure 5.7 (a) shows a rectangular pulse train of a frequency f_i and a 50 % duty cycle in time domain as $m_i(t)$. The corresponding magnitude response $|M_i(f)|$, which has a strong line spectrum at odd integer multiples of f_i, is shown in Figure 5.7 (b).

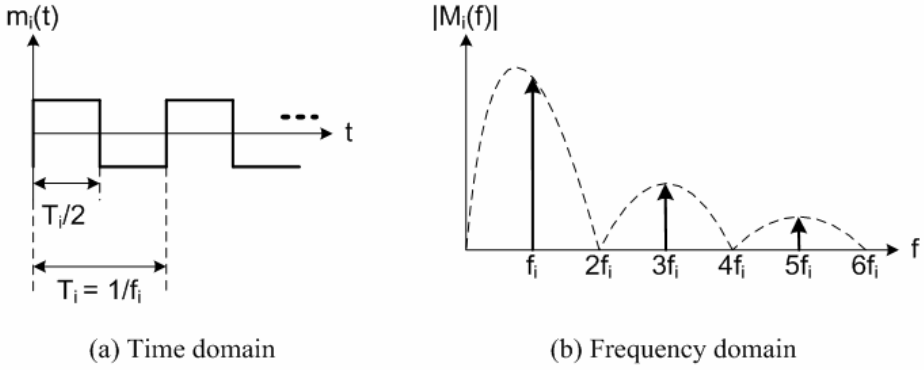

Figure 5.7 A rectangular pulse train in the time and frequency domains

Finally, to create a desired excitation signal $m(t)$ that can excite the structure in a target frequency range from f_l to f_h, the fundamental frequency f_i of the rectangular pulse train is incrementally changed from f_l to f_h. Depending on the necessary frequency

resolution of a structural excitation, the required number of frequency components in the target frequency range k is determined. Then, the fundamental frequency f_i of the rectangular pulse train is changed from f_1 to f_k as shown by the time domain excitation signal $m(t)$ in Figure 5.8 (a), where $f_1 = f_l$ and $f_k = f_h$, so that the resulting excitation signal can cover the entire target frequency range from f_l to f_h with a frequency resolution of $(f_h - f_l)/k$ as shown by the magnitude response of the excitation signal $|M(f)|$ in Figure 5.8 (b). Notice that the excitation frequency is altered at a constant time interval to excite the structure with the same amount of energy at each frequency.

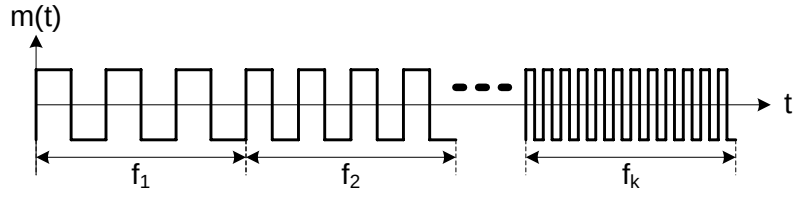

(a) Time domain

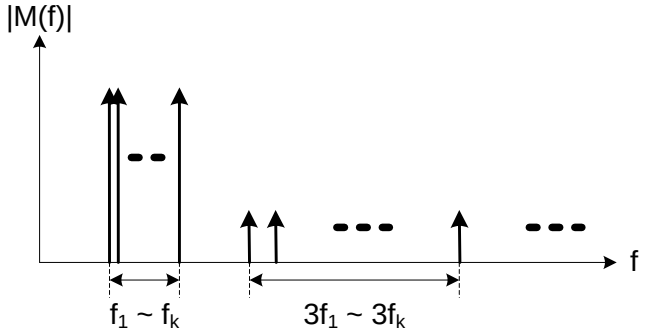

(b) Frequency domain

Figure 5.8 Excitation signal

The proposed excitation signal has odd harmonics outside the target frequency range, as well as desired frequency components in the target frequency range as shown in Figure 5.8 (b). Physically, a rectangular pulse train with a frequency f_i and 50 % duty cycle $m_i(t)$ is a superposition of a sinusoid with a fundamental frequency f_i and

sinusoids with odd integer multiples of f_i and decreasing amplitudes as expressed in equation (5.4), where A denotes an arbitrary amplitude gain.

$$m_i(t) = A\left[\sin(2\pi f_i t) + \frac{1}{3}\sin(6\pi f_i t) + \frac{1}{5}\sin(10\pi f_i t) + \cdots\right] \tag{5.4}$$

Thus, the even harmonics are effectively suppressed, while the energy levels of the third and fifth harmonics are −9.5 dBc and −14.0 dBc respectively, compared to that of the fundamental frequency component. This work will estimate the precise rectangular pulse train expressed in equation (5.4) into a simplified form that includes frequency components up to the third harmonic as represented in equation (5.5) by ignoring harmonics whose energy level is more than 10 dB lower than the energy level at the fundamental frequency component.

$$m_i(t) \cong A\left[\sin(2\pi f_i t) + \frac{1}{3}\sin(6\pi f_i t)\right] \tag{5.5}$$

It appears in Figure 5.8 (b) that there is a possibility of interference by the third harmonic frequency range on to the target frequency range, when $f_k > 3f_1$. However, it is not critical whether the target frequency range and the frequency range occupied by the third harmonics conflict or not because the Binary Method excites the structure with only one frequency at a time, and the third harmonic of one frequency cannot occur simultaneously with the first harmonic of another frequency. Figure 5.8 (b) shows a cumulative magnitude response of the excitation signal after all frequency components from f_1 to f_k are covered once. Therefore, the third harmonic of a particular excitation frequency f_i cannot affect the excitation quality of another excitation frequency f_j.

Keeping the duty cycle of the rectangular pulse train as 50 % is important to effectively suppress the harmonics at DC and even integer multiples of the fundamental frequency, and to maximize the energy at the fundamental frequency. The rectangular pulse train with anything other than a 50 % duty cycle spreads the energy on the odd harmonics over DC and even harmonics, as illustrated in Figure 5.9 with an example duty cycle of 30 %. Thus, the resulting excitation signal composed with a rectangular pulse train of a non-50 % duty cycle contains less energy than that with a 50 % duty cycle at the desired frequency range and becomes vulnerable to background noise.

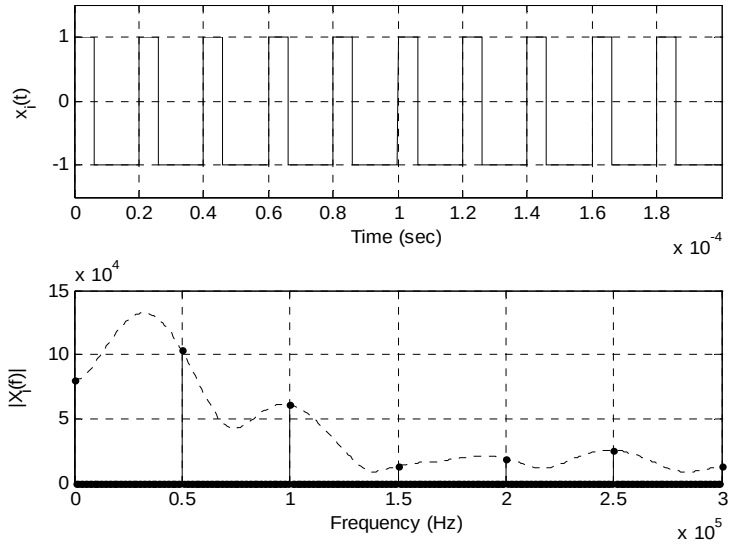

Figure 5.9 Example rectangular pulse train with 30 % duty cycle and a frequency of 50 KHz

The proposed excitation signal, which is a rectangular pulse train with a varying fundamental frequency, is capable of exciting the structure in a specific frequency range with a comparable excitation quality to other analog excitation signals such as a swept sinusoid and a sinc wave, but with a simpler generation algorithm, while providing enough information for structural condition assessment utilizing the phase difference of PZT's electrical admittance.

5.4 Excitation and Sensing

5.4.1 Estimation of PZT Admittance Phase

The rectangular pulse train excitation signal passes through an excitation and sensing block, which consists of an actuator / sensor block, a comparator, and a phase detector as shown in Figure 5.10. The actuator / sensor block is in charge of exciting a collocated actuator / sensor with an electrical excitation signal, actuating the structure by transforming the received electrical excitation signal into a mechanical stress, and sensing the structure's mechanical response transformed back into a format of an electrical signal.

The sensed electrical response of the structure is then converted into a binary format through a comparator. The binary structural response is compared with the original excitation signal to draw out the information on phase shift through the actuator / sensor block and a comparator.

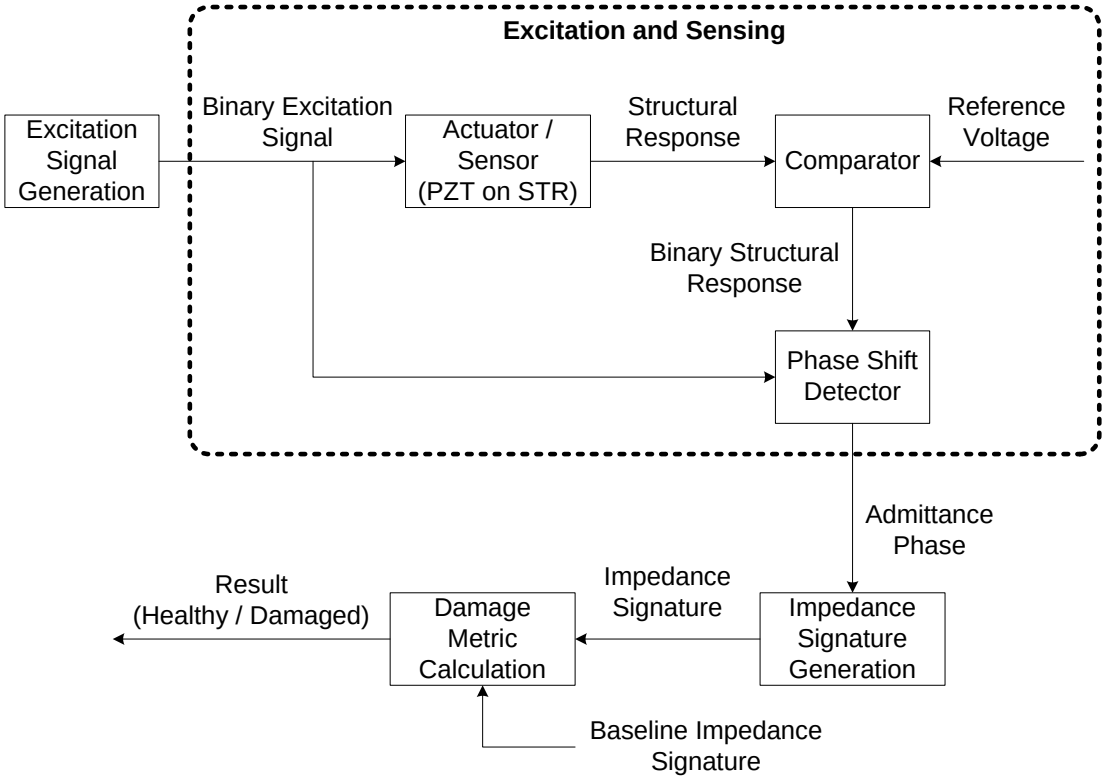

Figure 5.10 Overall operation block diagram – Excitation and sensing operations are boxed.

An inverting op amp configuration employed by the Wideband Method is used again in the Binary Method as an actuator / sensor configuration, and as opposed to the Wideband Method, a comparator follows the inverting op amp configuration instead of an ADC as shown in Figure 5.10. As discussed in Section 4.4, the structural response through an inverting op amp configuration represents the electrical admittance of PZT, as expressed in equation (5.6).

$$Y_p(j\omega) \cong H_{ioc}(j\omega) \tag{5.6}$$

$Y_p(j\omega)$ is the electrical admittance of PZT, and $H_{ioc}(j\omega)$ is the frequency response of the inverting op amp configuration. Therefore, PZT's admittance phase, which the structural condition assessment of the Binary Method depends on, can be estimated by the phase response of the inverting op amp configuration as expressed in equation (5.7).

$$\phi_p(j\omega) = \angle Y_p(j\omega) \cong \angle H_{ioc}(j\omega) \tag{5.7}$$

$\phi_p(j\omega)$ and $\angle Y_p(j\omega)$ denote the phase of PZT's electrical admittance, and $\angle H_{ioc}(j\omega)$ denotes the phase response of the inverting op amp configuration. The phase response of the inverting op amp configuration $\angle H_{ioc}(j\omega)$ can be found by comparing phases of the input and output of the inverting op amp configuration, as expressed in equation (5.8).

$$\angle Y_p(j\omega) \cong \angle H_{ioc}(j\omega) = \angle P(j\omega) - \angle M(j\omega) \tag{5.8}$$

$\angle P(j\omega)$ and $\angle M(j\omega)$ denote phase responses of the output and input of the inverting op amp configuration, respectively. Thus, the structural response, which is the output of the inverting op amp configuration, passes through a comparator to transfer only the minimum information required to monitor the phase. Finally, the binary structural response is compared with the binary excitation signal by an XOR gate to detect the phase shift through an inverting op amp configuration and a comparator, which is an estimated admittance phase of PZT as expressed in equation (5.9).

$$\angle Y_p(j\omega) \cong \angle P(j\omega) - \angle M(j\omega) \cong \angle Q(j\omega) - \angle M(j\omega) \tag{5.9}$$

$\angle Q(j\omega)$ is the phase response of the binary structural response, which is an output of the comparator. As presented in equation (5.9), only the relative phase of the structural response referenced to the binary excitation signal, instead of the absolute phase, can estimate PZT's admittance phase, which is why the structural response can be simplified into a binary format and a straightforward method based on an XOR gate. This, in turn, can be applied to monitor PZT's admittance phase rather than a complicated FFT operation.

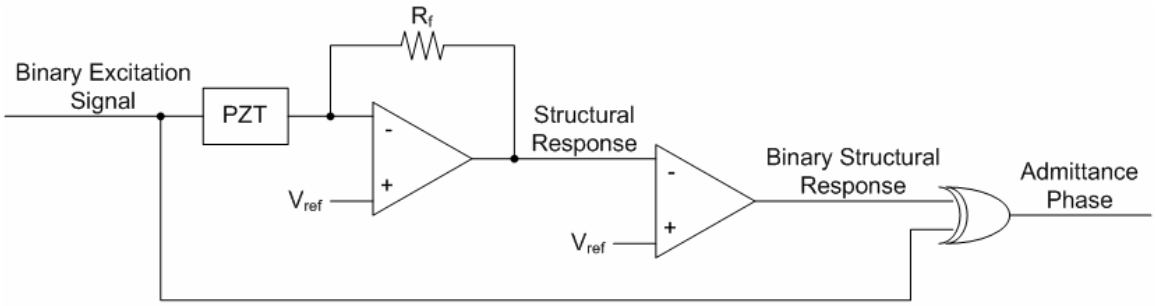

Figure 5.11 Excitation and sensing block structure

Notice that by passing the structural response through a comparator, a propagation delay caused by the comparator is added to the analog structural response. Since a phase response is a frequency domain characteristic and a propagation delay is a time domain characteristics, it is convenient to transform one of them into another domain and analyze them together. Thus, the phase response is converted into a time domain quantity, the phase delay.

The phase response of an arbitrary linear system $\angle H_a(f)$, as expressed in equation (5.10), has a linear relationship to the phase delay $T_d(f)$, which is the time delay experienced by a signal of a particular frequency f_0.

$$T_d(f_0) = -\frac{\angle H_a(f_0)}{2\pi f_0} \tag{5.10}$$

Thus, the phase response of the inverting op amp configuration can be estimated by accumulating the phase delay for a fixed identical time duration at each frequency. For instance, consider two different excitation frequencies f_1 and f_2, where f_2 equals to $2f_1$, and the phase delays where $T_d(f_1)$ is the same as $T_d(f_2)$, as shown in Figure 5.12. Then, the phase rotation experienced by the signal of a frequency f_2 $\angle H_a(f_2)$ should be twice that experienced by the signal of a frequency f_1 $\angle H_a(f_1)$. In Figure 5.12, $x(t)$ and $y(t)$ are the input and output of an arbitrary linear system $H_a(f)$ represented in time domain, respectively. Thus, instead of measuring the actual phase response $\angle H_a(f)$ at both frequencies f_1 and f_2, by measuring and accumulating the phase delay

for identical time duration *T*, the relative phase rotation at each frequency can be estimated.

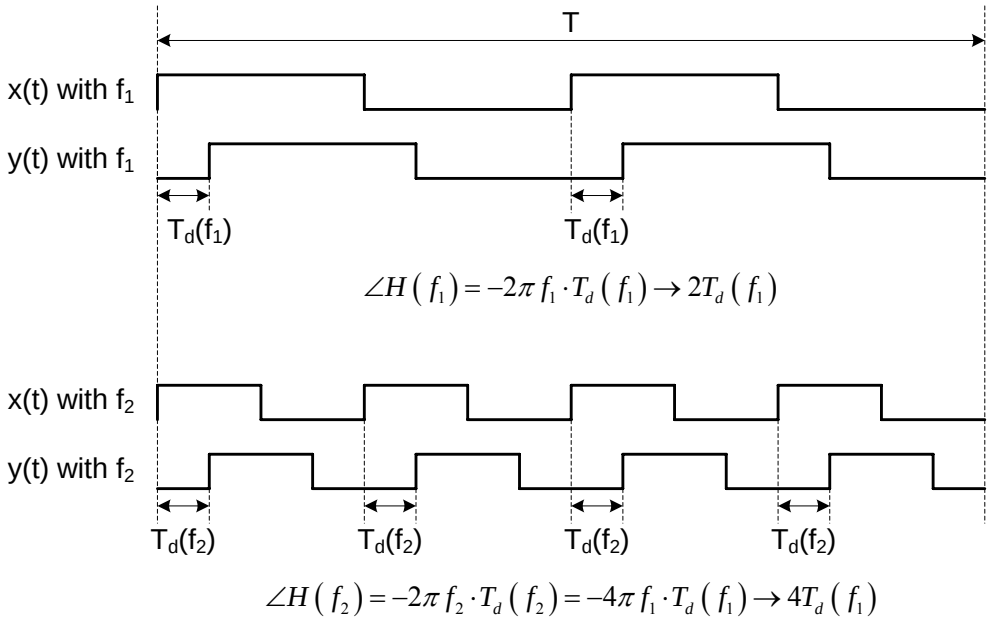

Figure 5.12 Phase rotation and phase delay

As seen in the waveforms of Figure 5.13, a simple way of measuring the phase delay is using an XOR gate, and accumulation of the phase delay can be performed by counting the period of high on the XOR result. The result of an XOR, which takes $x(t)$ and $y(t)$ as its two inputs, doubles the amount of phase rotation as shown in Figure 5.13, but it does not degrade the phase detection performance as long as the time duration for an accumulation is kept identical and the relative phase can be recognized.

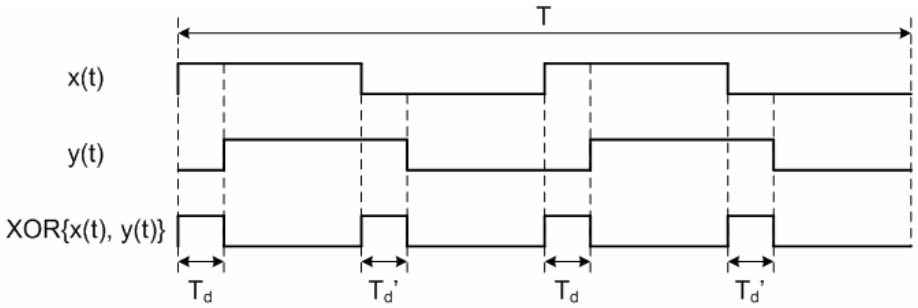

Figure 5.13 Phase estimation using an XOR gate

In the phase detection operation of this work, the two inputs to the XOR gate are the binary excitation signal and the binary structural response. The time delay on the binary structural response relevant to the binary excitation signal includes the propagation delay through the comparator, as well as the phase delay through the inverting op amp configuration. Thus, the XOR and accumulation result is an approximated electrical admittance phase of PZT. It was mentioned in Section 5.3 that the excitation period of each frequency was kept identical to excite the structure with the same amount of energy. The identical time period per excitation frequency is also desired in obtaining the phase of PZT's electrical admittance as covered in this section.

5.4.2 Binary Structural Response

The procedure driving the relationship between the admittance phase of PZT and the relative phase shift on the binary structural response compared to the binary excitation signal goes through several stages of approximation. Though the detected phase through an XOR gate is considered as an approximate of the admittance phase of PZT, nobody can disagree that there is more information contained in the detected phase. Therefore, it is crucial to analyze the actual information included in the measured relative phase shift, in order to understand the physical meaning of the measured quantity at the output of the excitation and sensing block and to propose appropriate damage metrics.

The inverting op amp configuration has frequency-dependent effects, which can be characterized by the frequency response of PZT on the excitation signal, and the

comparator has input signal waveform dependent effects, which can be explained by the hysteresis of a comparator, on the output of the inverting op amp configuration. Hence, the binary structural response is a combined function of the phase response of the inverting op amp configuration, which is an estimate of PZT's admittance phase, and the propagation delay through the comparator.

To understand frequency dependent characteristics of the inverting op amp configuration and to derive the relationship presented in equation (5.6), the frequency response of PZT, which is under the main interest to monitor structural integrity, is analyzed. As shown in Figure 5.14, an inverting op amp configuration is a voltage-sampling current-mixing amplifier, with the PZT as a feed-forward impedance and the excitation signal $m(t)$ as a voltage source. The output current $n(t)$ of the PZT is mixed with the feedback current through the feedback resistance R_f at the inverting input of the op amp.

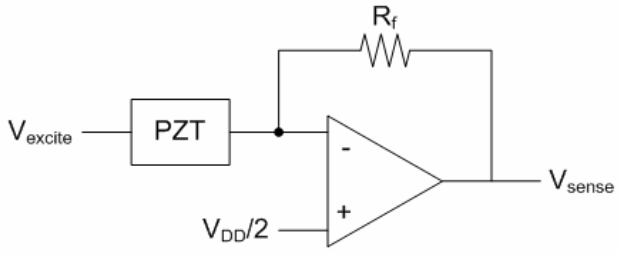

Figure 5.14 Inverting op amp configuration

As the input to the PZT $M(j\omega)$ is a voltage signal that excites the PZT, and the output of the PZT $N(j\omega)$ is a current signal that drives a negative input of the op amp from the relationship formulated in equation (5.11), the frequency response of the PZT $H_p(j\omega)$ can be defined as an admittance of the PZT $Y_p(j\omega)$.

$$H_p(j\omega) = \frac{N(j\omega)}{M(j\omega)} = \frac{I_{PZTout}}{V_{excite}} = Y_p(j\omega) \tag{5.11}$$

V_{excite} denotes the PZT excitation voltage changing between 0 V and Vdd and I_{PZTout} is the current output of the PZT.

The frequency response of the inverting op amp configuration $H_{ioc}(j\omega)$ is

$$H_{ioc}(j\omega) = \frac{P(j\omega)}{M(j\omega)} = \frac{V_{sense}}{V_{excite}} \tag{5.12}$$

where $P(j\omega)$ is a voltage signal at the output of the op amp, V_{excite} denotes the PZT excitation voltage, and V_{sense} is the sensed voltage representing the structural condition at the output of the op amp. The ideal inverting op amp configuration provides a linear transfer relationship of

$$V_{sense} = H_{ioc}(j\omega) \cdot V_{excite} = -R_f \cdot Y_p(j\omega) \cdot V_{excite} \tag{5.13}$$

Hence, the frequency response of the inverting op amp configuration $H_{ioc}(j\omega)$ becomes a linear function of the frequency response of the PZT $H_p(j\omega)$ as expressed in (5.14).

$$H_{ioc}(j\omega) = -R_f \cdot H_p(j\omega) \tag{5.14}$$

The frequency response of the inverting op amp configuration $H_{ioc}(j\omega)$ is dominated by the frequency response of the PZT $H_p(j\omega)$, as the feedback resistance R_f is frequency independent. Therefore, the frequency response of the inverting op amp configuration $H_{ioc}(j\omega)$ can be considered as a representation of the frequency response of PZT $H_p(j\omega)$ as expressed in equation (5.16).

$$H_{ioc}(j\omega) \cong H_p(j\omega) = Y_p(j\omega) \tag{5.15}$$

Equation (5.13) also confirms the relationship between the phase response of the inverting op amp configuration and admittance phase of PZT expressed in equation (5.7).

In order to understand input signal waveform dependent effects caused by a comparator, the comparator hysteresis is covered. Although a comparator is normally considered as having a single threshold value, practical comparators usually have hysteresis [1]. When a comparator has hysteresis, the comparator exhibits two threshold values, V_{TL} and V_{TH}, symmetrically placed about the desired reference level as illustrated in Figure 5.15.

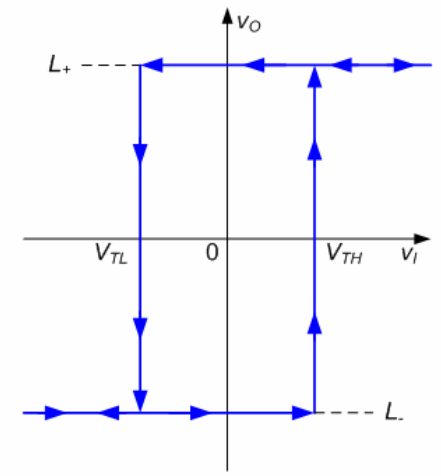

Figure 5.15 The complete transfer characteristics of a comparator with a reference level of 0 V

Depending on the input signal slope at the reference crossing, which is determined by the amplitude and the frequency of the input signal, the output step change has a different time delay. For instance, sinusoidal inputs with the same amplitude but with different frequencies have different reference crossing slopes. With the higher frequency, the input signal slope at the reference crossing becomes steeper, and the propagation delay through the comparator becomes shorter. Similarly, sinusoidal inputs with the same frequency but with different amplitudes also have different reference crossing slopes. The larger the amplitude, the steeper the slope at the reference crossing, which results in the shorter propagation delay through the comparator. Therefore, depending on the waveform of the comparator input *p(t)*, which is the output of the inverting op amp configuration, the total delay measured at the output of the excitation and sensing block *q(t)* will vary even if the delay through the inverting op amp configuration is constant.

5.4.3 PZT Frequency Response and Comparator Delay

Based on the relationship presented in equation (5.14) and the discussion regarding the comparator hysteresis, let us consider the phase shift as it appeared on the binary structural response in terms of a time delay, with a phase response of PZT, a

magnitude response of PZT, and a propagation delay of the comparator. As stated in equation (5.5), the rectangular pulse train excitation signal is considered to have the first and the third harmonics only.

5.4.3.1 PZT Phase Response and Comparator Delay

Assume a constant magnitude response of PZT over the frequency range from ω_0 to $3\omega_0$ to consider contributions from the phase response of PZT. If $H_{ioc}(j\omega)$ has a constant phase delay, which means that the PZT has a linear phase response, over the frequency band from ω_0 to $3\omega_0$, the waveform of the op amp output *p(t)* should be the same as the waveform of the PZT actuation signal *m(t)* except the polarity and a constant magnitude attenuation. Let us consider the time delay through the inverting op amp configuration measured at the op amp output *p(t)* of this case as a reference time delay $T_{ref,ioc}$, and name *p(t)* of this case as $p_{ref,phs}(t)$. The time delay through the comparator, when $p_{ref,phs}(t)$ is an input, is named as $T_{ref,comp}$.

Let us consider different phase delays at ω_0 and $3\omega_0$. If the third harmonic $3\omega_0$ encounters a longer phase delay through $H_{ioc}(j\omega)$ than the fundamental frequency component with an excitation frequency of ω_0, the overall time delay through $H_{ioc}(j\omega)$ T_{ioc} increases compared to $T_{ref,ioc}$. Similarly, in case the fundamental frequency component with an excitation frequency ω_0 provides a longer phase delay than the third harmonic $3\omega_0$ through $H_{ioc}(j\omega)$, the overall time delay through $H_{ioc}(j\omega)$ T_{ioc} also increases compared to $T_{ref,ioc}$.

Different phase delays at ω_0 and $3\omega_0$ also change the waveform of *p(t)* due to the phase distortion. Since the signal slope of a sinusoid is maximum at reference crossing, it is clear that the slope of a waveform that is a superposition of two sinusoids whose frequencies are ω_0 and $3\omega_0$ is maximized, when the reference crossing timings of those two frequency components are aligned. Therefore, if ω_0 and $3\omega_0$ have different phase delays through $H_{ioc}(j\omega)$, the slope of the op amp output waveform *p(t)* at reference

crossing is always gentler than that of $p_{ref,phs}(t)$. Consequently, the delay through the comparator T_{comp} is also affected. As the reference crossing slope of the comparator input $p(t)$ is decreased, the time required for $p(t)$ to propagate through the hysteresis of the comparator increases. Therefore, nonlinear phase delays at ω_0 and $3\omega_0$ increases the time delay through $H_{ioc}(j\omega)$, and resultantly increases the propagation delay through the comparator as well.

5.4.3.2 PZT Magnitude Response and Comparator Delay

The magnitude response of PZT $|H_p(j\omega)|$ becomes maximum at the resonant frequency ω_n of PZT. Thus, frequency components of the excitation signal $m(t)$ close to ω_n are transferred to the output of the op amp, while frequency components away from ω_n are filtered out. As discussed in Section 5.3, the excitation signal $m(t)$ has frequency components ω_0 and $3\omega_0$, so three possible relationships among ω_0, $3\omega_0$ and ω_n, and the resulting op amp output $p(t)$ are considered. Let us consider the op amp output signal without attenuation both at ω_0 and $3\omega_0$ as a reference output waveform $p_{reg,mag}(t)$.

The first possible relationship between the excitation signal frequency components and the PZT resonant frequency is when the fundamental frequency ω_0 of the excitation signal falls at the resonant frequency ω_n of the PZT. In this case, ω_0 becomes the dominant frequency component at the output of the op amp because the rest of the frequency components are filtered out while ω_0 has the maximum transfer rate from input to output. Notice that the reference crossing slope of the op amp output signal $p(t)$ of this case becomes gentler than the reference crossing slope of $p_{ref,mag}(t)$ because $p(t)$ lacks the $3\omega_0$ component that makes the reference crossing slope steeper. Thus, the delay caused by the hysteresis of the comparator is longer than the reference case.

If the 3-dB bandwidth is wide enough to cover the third harmonic $3\omega_0$ of the excitation signal, $3\omega_0$ component will be attenuated by less than 3 dB, but otherwise attenuation on $3\omega_0$ component will be large enough to filter out $3\omega_0$ through $H_{ioc}(j\omega)$. Depending on the 3-dB bandwidth, low ω_0 and high ω_0 can result in op amp output

signals with different waveforms as well as frequency components because $3\omega_0$ will experience different amounts of attenuation. Generally, higher ω_0 will cause more attenuation on $3\omega_0$ if there is no other resonant frequency or local resonant frequency near $3\omega_0$.

The second possible relationship between the excitation signal frequency components and the PZT resonant frequency is when the third harmonic $3\omega_0$ of the excitation signal falls at the resonant frequency ω_n of the PZT. In this case, $3\omega_0$ becomes the dominant frequency component at the output of $H_{ioc}(j\omega)$, because the rest of the frequency components are filtered out while $3\omega_0$ has the maximum transfer rate from input to output. The zero crossing slope of the op amp output signal *p(t)* of this case becomes steeper than the zero crossing slope of $p_{ref,mag}(t)$, because *p(t)* is short of the ω_0 component that makes the zero crossing slope gentler. The delay caused by the hysteresis of the comparator is shorter than the reference case.

Finally, when both fundamental excitation frequency ω_0 and its third harmonic $3\omega_0$ are away from a resonant frequency ω_n of the PZT, those two frequency components may have similar amounts of attenuation on their amplitude level. As the resonant frequency of the PZT does not have a distinctive effect on the output of the op amp *n(t)*, the time delay through the PZT, in other words the phase response of the PZT, becomes the dominant factor rather than the magnitude response of the PZT. This case was covered in Section 5.4.3.1, when considering the phase response of PZT.

5.4.3.3 Comparator Hysteresis

As discussed in Section 5.4.2, frequency response of the PZT changes the reference crossing slope of the comparator input signal, which changes the time required for the comparator input *p(t)* to stay in the hysteresis region. As the comparator input *p(t)* stays longer in hysteresis, *p(t)* is exposed to the thermal noise for a longer time. Thus, the signal-to-noise ratio of *p(t)* decreases, and the standard deviation on the binary structural response increases. The increased standard deviation is delivered through the XOR gate.

Since the slower signal stays longer in hysteresis, standard deviation on the delay increases as the excitation frequency ω_0 decreases. The gentler reference crossing slope of *p(t)* also increases the standard deviation, which typically happens when ω_0 is equal to ω_n as discussed in Section 5.4.3.1.

5.4.3.4 Mean and Standard Deviation of Phase

The accumulated XOR result should be averaged to remove the additive background noise. The time delays are determined based on the phase response of PZT, magnitude response of PZT, and the comparator propagation delay as discussed in Sections 5.4.3.1 and 5.4.3.2, and they can be observed through the averaged phase shift, which is considered as a primary impedance signature. The noise effect from the comparator hysteresis covered in Section 5.4.3.3 requires calculation of standard deviation of the accumulated XOR result. Thus, the standard deviation of the accumulated XOR result, which represents the standard deviation of the delay on the binary structural response, can be used as an auxiliary impedance signature.

If the overall delay through the inverting op amp configuration and the comparator $T_{overall}$ is same for healthy and damaged structural conditions, but the delay though $H_{ioc}(j\omega)\ T_{ioc}$ is different, the average of the accumulated XOR result will not change. In this case, if the standard deviation of the delay on the binary structural response is employed as a supplementary damage metric, the variations on the delay through $H_{ioc}(j\omega)\ T_{ioc}$ can be distinguished. A detailed analysis using the standard deviation of the measure phase is covered in Chapter 6.

5.5 Structural Condition Assessment

The XOR result, which represents the delay through the inverting op amp configuration and a comparator, from the excitation and sensing block is accumulated for a certain period to create an impedance signature mainly characterizing the admittance

phase of PZT. For structural condition assessment, the first impedance signature is stored as a reference structural condition, and each of the successively generated impedance signatures is compared with the baseline impedance signature to monitor the structural integrity as shown in Figure 5.16. The comparison between the baseline impedance signature and the current impedance signature calibrates a damage metric, and the damage metric is compared with a threshold level to determine if the structure is intact or damaged.

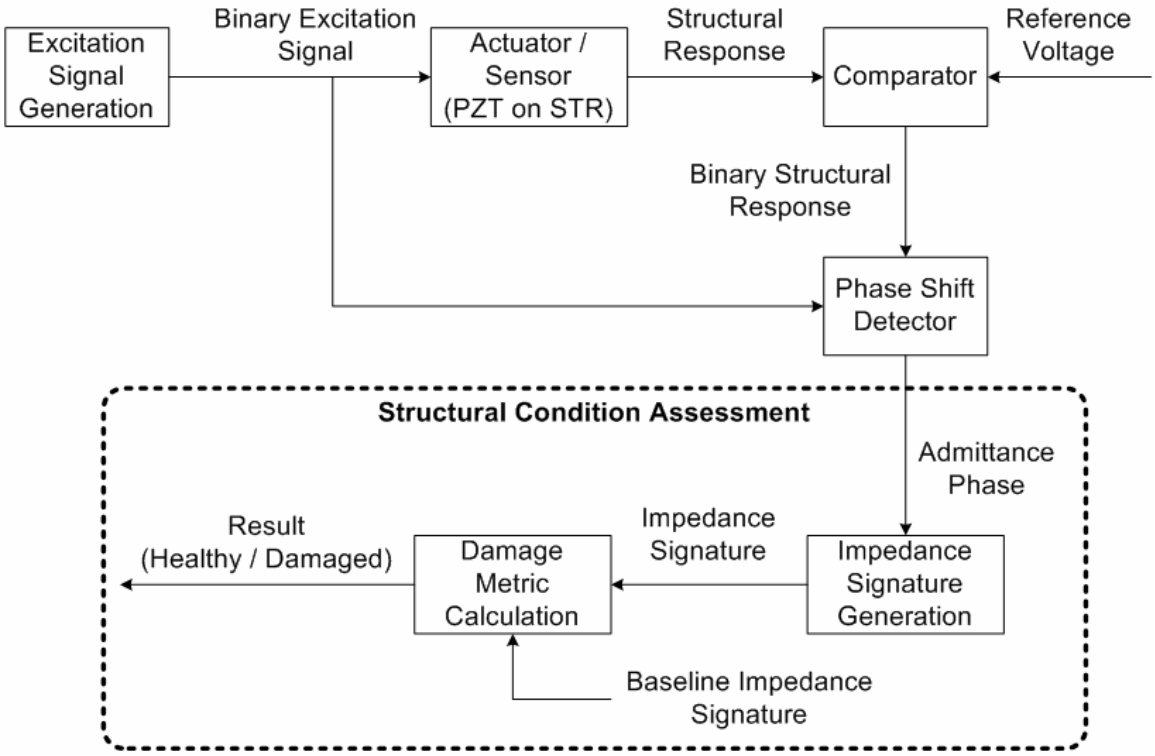

Figure 5.16 Overall operation block diagram – Structural condition assessment operations are boxed.

In actual system development, the structural condition assessment is performed by a DSP (or a microcontroller), and the XOR output is sampled by a one-bit signal. Note the XOR operation can either be performed by an external XOR gate outside the DSP (or a microcontroller), or by a software operation within the DSP. In either case, the XOR result is a sequence of one-bit data. The XOR result is accumulated for a certain time duration at each excitation frequency, and the accumulated XOR result is averaged to

create an impedance signature at each excitation frequency. The accumulated XOR result is named as a variation count. The averaged variation count at each frequency component within the target frequency range constitutes an impedance signature.

The damage metric is defined as a sum of squared difference (SSD) between the baseline and the current variation counts, as expressed in equation (5.17).

$$SSD = \sum_{f=0}^{N_{freq}-1} \left[VC_B(f) - VC_C(f) \right]^2 \tag{5.16}$$

VC_B is the baseline variation count, and VC_C is the current variation count. N_{freq} denotes the number of frequency components in the target frequency range. When the structure stays in a healthy condition, the SSD value will remain under a certain threshold level. Upon occurrence of damage to the structure, the fresh variation count diverges from the baseline due to the alteration on the mechanical impedance of the structure. When the increased SSD value becomes larger than the preset threshold value, the system indicates damage and warns the system operator.

As opposed to the FFT-based structural condition assessment method used in previous impedance-based SHM systems, the proposed method replaces memory-intensive ensemble average and computation-intensive FFT with a binary number accumulation on signature acquisition. Computational burden on damage metric calibration is also alleviated by adopting SSD instead of RSMD. A simplified assessment procedure contributes to reducing the power dissipation at the DSP by adopting a low-performance DSP operating at a low clock frequency.

5.6 Performance Analysis

5.6.1 Test Structure and Preliminary Measurements

In order to verify the operation of the proposed Binary method, a set of measurements has been performed. The test structure is an aluminum beam, and two cylindrical magnets are used to apply pressure to the structure as simulated damage. Using magnets attracted through the beam thickness, the damage is non-permanent and

repeatable. Two pairs of magnet with different forces are used. The magnets are applied to near, center, and far locations with respect to the PZT, and the exact damage locations, along with detail dimensions of the test structure, are illustrated in Figure 5.17.

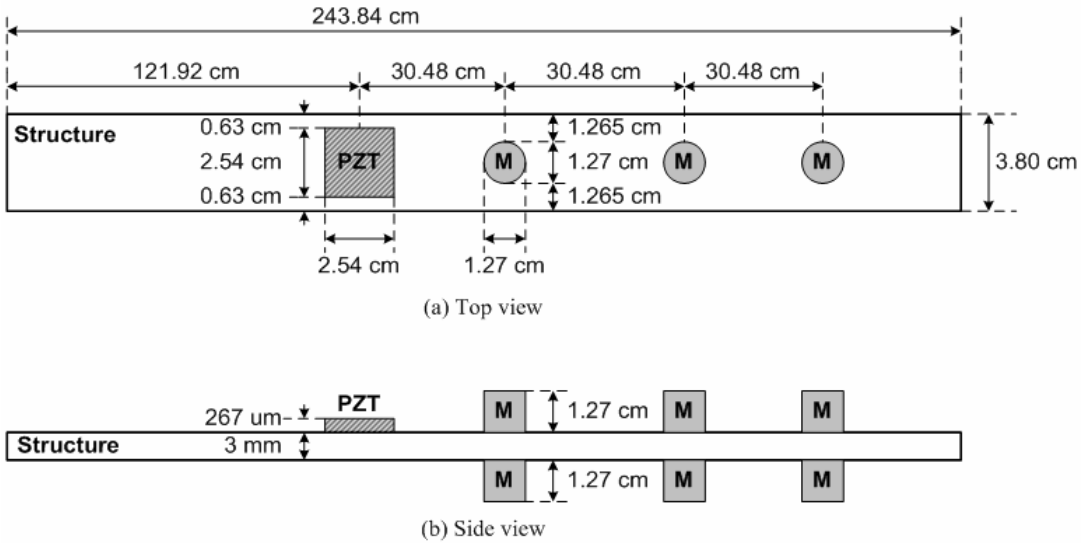

Figure 5.17 Test structure

Since the DSP utilized in our prototype has limited data memory size, it is efficient to focus on a frequency range sensitive to the structural excitation. Impedance analysis is performed on the PZT bonded to the test structure using a HP 4194A impedance analyzer to determine the detection frequency range. The impedance of the beam without and with damage is measured from 100 Hz to 100 KHz with a frequency resolution of 20 Hz. To alleviate noise effects, 35 measurements were taken, and the maximally occurring value was selected at each frequency through a histogram analysis. Figure 5.18 presents the conductance extracted from the measured impedance without damage. It is noticeable that the test structure is sensitive to the excitation in the frequency ranges from 12 KHz to 25 KHz and from 68 KHz to 76 KHz. The higher detection frequency requires a faster operating clock on generating the excitation signal, which in turn increases the power dissipation. Hence, the frequency range from 12 KHz to 25 KHz is chosen as a target frequency range.

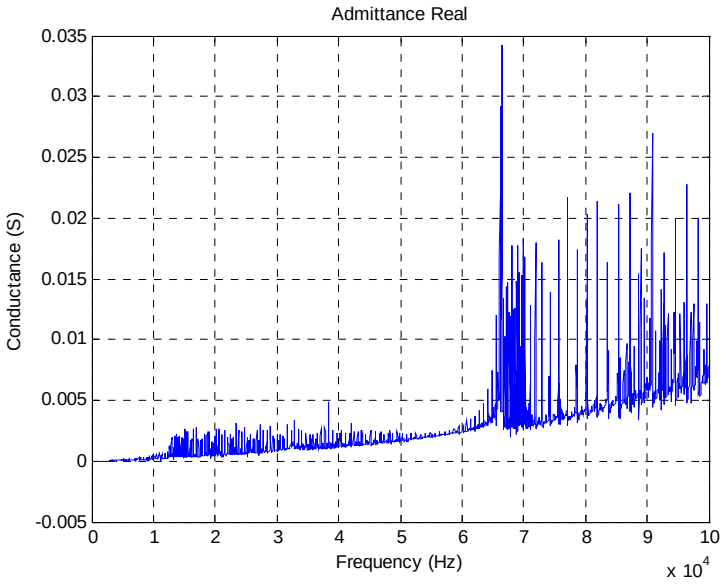

Figure 5.18 Conductance from the impedance analyzer measurement data

RMSD values, the damage metric generally used in traditional impedance-based SHM, are also calculated based on the admittance from the measured impedance as a reference performance for the verification purposes. Table 5.1 shows the calculated RMSD values for applied damage. We can observe that the damage metric decreases from Position 1 to Position 3, and Force 2 causes a damage metric larger than the Force 1. Therefore, the DSP prototype is expected to provide a larger damage metric for Force 2 than Force 1, as well as a decreasing damage metric from Position 1 to Position 3. in Table 5.1, Position 1, Position 2 and Position 3 indicate near, center and far locations in Figure 5.17, respectively.

Table 5.1 RMSD of the real admittance calculated based impedance measured by impedance analyzer

	Position 1	Position 2	Position 3
Force 1	280.17	273.61	253.89
Force 2	311.12	292.89	291.96

The feedback resistor R_f for excitation and sensing configuration shown in Figure 5.5 is selected as 100 Ω, based on the magnitude of the measured impedance within the selected target frequency range. The magnitude of the impedance for the Healthy status in the target frequency range varies from 95 Ω to 302 Ω in a 99 % confidence interval. As expressed in equation (4.3), the gain of the op amp is R_f / Z_{PZT}, and the op amp negative input voltage v_{excite} swings between 0 V and Vdd. Thus, to keep the excitation and sensing configuration operating as a rational amplifier, R_f is selected as 100 Ω, which is the lower boundary of the 99 % confidence interval maintaining an amplifier gain of less than unity.

5.6.2 Prototype Development with a DSP

5.6.2.1 System Design

The prototype implementing the Binary Method is based on the TMS320F2812 EVM from Texas Instruments [34]. TMS320F2812 is a 32-bit fixed point DSP supporting up to 150 million instructions per second (MIPS) operation. The maximum core operating clock frequency is 150 MHz and can be reduced down to 15 MHz by changing the phase locked loop (PLL) multiplier setting. The peripheral clock frequency can be selected as high as the core operating clock frequency or as low as the core operating clock frequency divided by 14. The supply voltage for the DSP core is 1.8 V at 130 MHz and 1.9 V at 150 MHz. For Input/Output utilization, the supply voltage is 3.3 V, while the recommended supply voltage for the entire EVM is 5 V. The low-power algorithm relies on binary signaling rather than multiple voltage levels for structural excitation, requires simple accumulation instead of FFT operations which involves intensive multiplications for signature generation, and takes advantage of subtraction instead of a square root operation for damage metric calculations. Hence, we can employ a low-power, relatively slow 32-bit fixed point DSP, while the previous sinc waveform based prototype required a power-hungry 225 MHz 64-bit floating point DSP.

In addition to the DSP, there are two more IC devices involved for PZT excitation and sensing operation. The excitation and sensing operation requires two buffers, a

comparator, and an op amp. A four-channel op amp OPA4342 from Texas Instruments is employed to implement two buffers and a comparator, and a single-channel op amp TLV2770 from Texas Instruments is adopted for the op amp [35][36]. Some miscellaneous components, such as resistors and an LED are also included.

One buffer is connected between the binary output from the DSP and the PZT on the measuring path, and the other buffer is connected between the binary output from the DSP and the binary input to the DSP on the reference path to avoid loading effects. If a buffer is not inserted between two components on a signal path, a voltage drop occurs due to the voltage dividing between the output impedance of the component transmitting the signal and the input impedance of the component receiving the signal. Thus, a buffer, whose ideal input impedance is infinite and ideal output impedance is zero, is inserted between them to ensure maximum voltage transfer. A comparator is connected to the output of the op amp to convert the structural response into a binary signal to be measured by the DSP. This comparator performs the function of a buffer as well. In the previous prototype, we did not have to insert buffers because the DAC EVM and ADC EVM had buffers on-board. For this Binary Method prototype, we effectively replace high-power consuming DAC EVM and ADC EVM with a buffer and a comparator, which resultantly reduces power dissipation significantly and miniaturizes the form factor.

The prototype is shown in Figure 5.19. TMS320F2812 EVM is 7.62 cm X 12.7 cm, and the external bread board consists of op amp ICs, resistors and an LED. The LED is turned on and off to indicate structural damage based on the detection result calculated by the DSP.

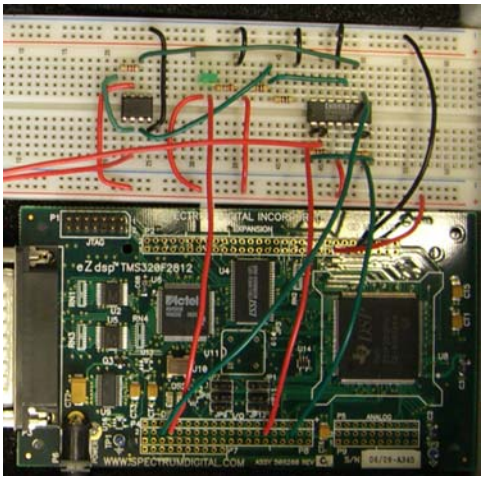

Figure 5.19 Prototype using TMS320F2812 EVM

5.6.2.2 Frequency Resolution

The frequency resolution in the detection frequency range mainly depends on the available data memory size and the peripheral clock frequency. Memory allowance for user data in TMS320F2812 is 960 × 16-bit. Since a signature is an ensemble average of a certain number of variation counts, a certain number of consecutive variation counts at each frequency component should be stored in the memory. The baseline, current signature, and the difference between them also have to be stored for a damage metric calculation. Thus, the required memory space N_{mem} is

$$N_{mem} = (3 + N_{avg}) \times N_{freq} \tag{5.17}$$

where N_{avg} is the number of variation counts per signature and N_{freq} is the number of frequency components per variation count. Setting N_{avg} as eight, we obtain the maximum number of frequency components per variation count $N_{freq,MAX}$ as 87 from the following relationship.

$$N_{freq,MAX} = \left\lfloor \frac{960}{(3+8)} \right\rfloor = 87 \tag{5.18}$$

The excitation frequency is controlled by changing the pulse width of the PWM output, and the pulse width is managed by decreasing the number of peripheral clock cycles per pulse. For example, when the default clock configuration is used, the

peripheral clock frequency is 75 MHz. As the pulse width of the lowest frequency component 12 KHz is 83 μsec, and that for the highest frequency component 25 KHz is 40 μsec, the number of peripheral clock cycles per pulse width is 6250 and 3000, respectively. To minimize the computational complexity of calculating the pulse width for each frequency component, the number of peripheral cycles per pulse width is decremented by a constant amount, instead of calculating decrement cycles to generate linearly increasing excitation frequency. As the maximum number of frequency components per variation count calculated based on the memory allowance is 87 from equation (5.18), the minimum decrement of pulse width, in terms of the number of peripheral clock cycles $N_{pclk,MIN}$, is

$$N_{pclk,MIN} = \left\lceil \frac{(N_{pclk,low} - N_{pclk,high})}{N_{freq,MAX}} \right\rceil = \left\lceil \frac{(6250 - 3000)}{87} \right\rceil = 38 \qquad (5.19)$$

where $N_{pclk,low}$ and $N_{pclk,high}$ are the number of peripheral clock cycles for the lowest detection frequency and the highest detection frequency. $N_{pclk,low}$ and $N_{pclk,high}$ are 6250 and 3000, respectively, in this example.

Figure 5.20 shows the number of peripheral clock cycles versus calculated excitation frequency and the frequency resolution at each excitation frequency component. Since the number of peripheral clock cycles is decremented linearly, the excitation frequency does not linearly increase. The frequency resolution increases as the excitation frequency increases instead of providing a constant frequency resolution within the detection frequency range. The average frequency resolution through the excitation frequency range is 151 Hz in this example.

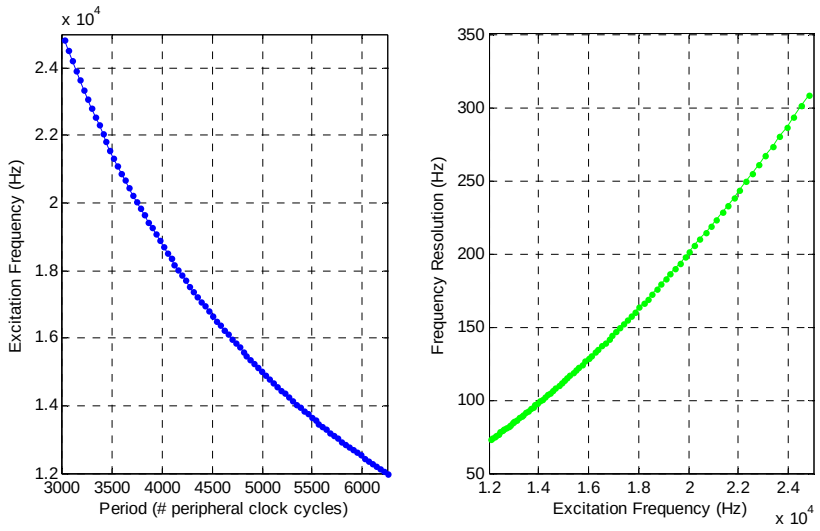

Figure 5.20 Example calculated excitation frequencies and frequency resolution – Peripheral clock frequency is 75 MHz and the number of frequency components in the detection frequency range is 87

5.6.2.3 Damage Detection Performance

The SSD damage metric obtained from the DSP prototype implementing the Binary Method is summarized in Table 5.2. The same test setup covered in Sections 5.1 is used. Clearly, the Binary Method can detect the damage on the structure as the SSD value is five to seven times larger for damaged structures than for healthy structure. Also, it is noticeable that the proposed approach can distinguish different types of damage because the SSD value is larger for Damage 1 than Damage 2 as predicted by the RMSD values calculated from the impedance analyzer measurement data.

Table 5.2 SSD of the variation count measured by the DSP prototype

	Position 1	Position 2	Position 3
Healthy	4554		
Force 1	29030	27354	23773
Force 2	31569	30592	27041

5.6.2.4 Power Dissipation

Power dissipation with different core operating clock frequencies is compared as shown in Table 5.3. The power dissipation was calculated based on the measured current dissipation and the EVM supply voltage. When the core operating clock frequency is 150 MHz, the power dissipation is 1.7 W. It is noticeable that the whole SHM system can operate under 1 W with a core operating clock frequency of 15 MHz. The total power dissipation will be further reduced when we enclose the miscellaneous external circuitry on to a single PCB and utilize miniaturized components, such as surface mount resistors and LEDs as well as small outline packaging for op amp ICs.

Table 5.3 Core operating clock frequency and power dissipation

Core Operating Clock (MHz)	Supply Voltage (V)	Current Consumption (mA)	Power Consumption (mW)
15	5	158	790
60	5	222	1110
105	5	285	1425
150	5	343	1715

5.6.3 Prototype Development with a Microcontroller

Another prototype for the Binary Method is developed based on a dsPIC30F6010A EVM from Microchip. dsPIC30F6010A is a 16-bit microcontroller supporting up to 30 MHz operation clock frequency. The peripheral clock frequency is the same as the operation clock frequency. The supply voltage for the microcontroller core and the EVM is 3.3 V. The same external circuitry used to compose the DSP based prototype is used for the microcontroller based prototype, but it is soldered on to the prototyping area on the microcontroller EVM as shown in Figure 5.21.

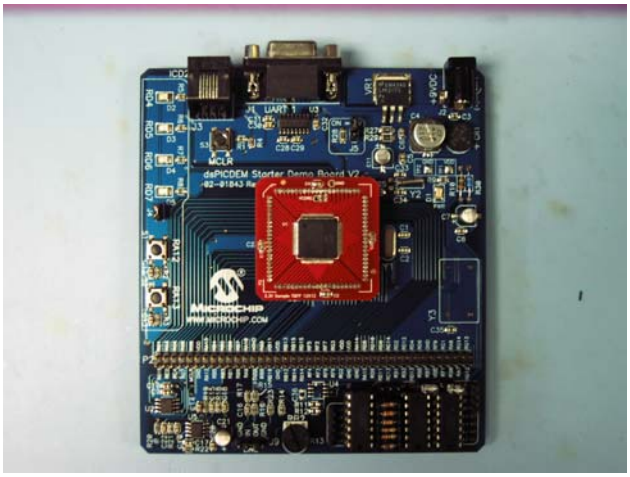

Figure 5.21 Prototype with a microcontroller EVM

The damage detection performance is summarized in Table 5.4. The power dissipation is 855 mW. Note that the operating clock frequency of the microcontroller prototype is twice as fast as that of the DSP prototype. Thus, the power dissipation of the microcontroller can be lower than that of the DSP prototype if the microcontroller operates at the same operating clock frequency as the DSP.

Table 5.4 SSD of the variation count measured by the DSP prototype

	Position 1	Position 2	Position 3
Healthy	1238		
Force 1	7259	6868	5933
Force 2	7902	7631	6730

5.7 Comparison

Two proposed methods, the Wideband Method and the Binary Method are compared with the Sinc Method and the Impedance-Chip Method, which were introduced in Section 2.3. The Sinc Method and the Impedance-Chip Method are the only methods realizing the impedance-based SHM with an autonomous hardware prior to the two proposed methods. The comparison criteria include computational complexity, memory requirements, damage detection speed, system form-factor and power dissipation. Note

that since the Impedance-Chip Method exploits a separate computer to process structural condition assessment, some comparison criteria listed in the following subsections are not fair.

5.7.1 Computational Complexity

Computational complexity can be examined from two points of view: Excitation signal generation and structural condition assessment. Table 5.5 summarizes types of excitation signals and methodologies of structural condition assessment of impedance-based SHM methods under comparison.

Table 5.5 Excitation signals and structural condition assessment methodologies

Method	Excitation Signal	Structural Condition Assessment
Sinc	Sinc wave	FFT and RMSD
Wideband	Wideband PN sequence	FFT and RMSD
Binary	Square wave	Accumulation and SSD
Impedance-Chip	Frequency-Sweep Sinusoid	FFT and RMSD

A sinc wave employed by the Sinc Method is a superposition of multiple sinusoidal signals whose frequencies are determined by frequency components of the target frequency range. When the number of frequency components in the target frequency range is N_{freq}, N_{freq} sinusoidal signals should be generated, which requires the same degree of computational effort as the Impedance-Chip Method. Since the Sinc Method accumulates the generated sinusoidal signals to compose a sinc signal, an additional accumulation operation is necessary compared to the Impedance-Chip Method. However, since the Sinc Method can store the generated sinc excitation sequence in a memory and use it repetitively, the excitation signal generation is required only once at system start-up, while the Impedance-Chip Method generates a sinusoidal excitation signal constantly with varying frequency through the operation.

The Wideband Method uses a PN sequence, which is relatively simple to generate compared to N_{freq} sinusoidal signals with different frequencies. A PN sequence is a binary outcome of an LFSR, which consists of an N_{LFSR}-bit register and several XOR operations. Thus, the only operations needed to produce one element of a PN sequence are a one-bit shift right plus a certain number of XORs. The number of frequency components N_{freq}, to which the computational complexities of the excitation signal generations for the Sinc Method and the Impedance-Chip Method are linearly proportional, is not a critical factor affecting the amount of calculations to generate a wideband excitation signal. N_{freq} is determined based on the length of the LFSR as $2^{N_{LFSR}}-1$, and larger N_{freq} requires a shift operation of a longer register and more XOR operations, which are trivial in terms of computational complexity compared to generating more sinusoidal signals.

Generating an excitation signal for the Binary Method is even simpler than those for other methods, as only two counters are necessary. The first counter determines the excitation frequency by counting the number of clock cycles to toggle the excitation signal output from positive to negative or from negative to positive at a specific temporal interval. The second counter changes the excitation frequency by counting the number of clock cycles to change the upper limit of the first counter that determines when to toggle the excitation output signal.

Table 5.6 Computational complexity of excitation signal generation

Method	Excitation Signal	Computational complexity
Sinc	Sinc wave	N_{freq} sinusoidal signals and accumulation
Wideband	Wideband PN sequence	1-bit Shift and XORs
Binary	Square wave	Two counters
Impedance-Chip	Sinusoid	N_{freq} sinusoidal signals

Structural condition assessments of the Sinc, Wideband and the Impedance-Chip Methods necessitate FFT to obtain an impedance signature and calibration of an RMSD of the baseline signature and the current signature. FFT operation involves (N_{freq}/2)

$\log_2 N_{freq}$ complex multiplications and $N_{freq}\log_2 N_{freq}$ complex additions when radix-2 N_{freq}-point FFT is performed [57]. The damage metric RMSD requires additional $2N_{freq}$ multiplications, N_{freq} divisions and a square root operation. As opposed to those three methods, on signature acquisition, the Binary Method replaces the computation-intensive FFT with a simple 1-bit number accumulation. Computational burden on damage metric calibration is also alleviated down to N_{freq} multiplications and a square root by adopting a vector distance instead of RMSD. The computational complexity of structural condition assessment is summarized in Table 5.7.

Table 5.7 Computational complexity of structural condition assessment

Method	Excitation Signal	Computational complexity
Sinc	Sinc wave	$(N_{freq}/2)\log_2 N_{freq}$ complex multiplications, $N_{freq}\log_2 N_{freq}$ complex additions $2N_{freq}$ multiplications, N_{freq} divisions and a square root
Wideband	Wideband PN sequence	Same as the Sinc Method
Binary	Square wave	Accumulation, N_{freq} multiplications
Impedance-Chip	Sinusoid	Same as the Sinc Method

5.7.2 Memory Requirements

Memory is mainly required to store the excitation signal for repetitive output and the structural response for impedance signature and damage metric generation. The Sinc Method and the Wideband Method store one period of the excitation sequence in a memory. Since the Sinc Method relies on a k_{DAC}–bit DAC when sending out the excitation sequence, $k_{DAC}\times N_{freq}$ memory space is required, while the Wideband Method requires N_{freq} memory space. The Binary Method and the Impedance-Chip Method do not require memory space for an excitation signal.

A signature generation requires several measurements for ensemble average to mitigate burst noise on the sensed structural response, and the sensed signal is represented with multiple bits in methods other than the Binary Method. Thus, all methods require at least $M_{avg}(=N_{avg}\times N_{bit})$ memory locations to store the measured structural response for ensemble average calculation, where N_{avg} and N_{bit} indicate the number of averaged measurements per signature and the number of bits for sensed signal representation. In case of the Binary Method, N_{bit} depends on the number of samples accumulated after the XOR operation, while N_{bit} is the resolution of the ADC for other methods. Furthermore, signature calculation requires FFT operation, which requires an extra memory space of M_{FFT} for all methods except the Binary Method. The memory requirements are summarized in Table 5.8.

Table 5.8 Computational complexity of structural condition assessment

Method	Excitation Signal	Memory Requirements
Sinc	Sinc wave	$k_{DAC}\times N_{freq}$, M_{avg}, M_{FFT}
Wideband	Wideband PN sequence	N_{freq}, M_{avg}, M_{FFT}
Binary	Square wave	M_{avg}
Impedance-Chip	Sinusoid	M_{avg}, M_{FFT}

5.7.3 Damage Detection Speed

The time taken on obtaining one damage metric after starting the structural excitation determines the speed of damage detection. The most critical factor that determines damage detection speed is the time duration required to excite the target frequency range because the structural response is measured at a certain sampling frequency while the structure is excited. Let us assume that other operational parameters, such as the sampling frequency of the structural response, the number of averages, and the frequency resolution in the target frequency range are identical among all methods.

The Sinc Method and the Wideband Method compress the excitation signal in a time domain either by overlaying signals with different excitation frequencies on top of

each other or by covering the target frequency range with a short noise-like sequence. On the contrary, the Binary Method keeps the time domain span of the excitation signal by exciting the structure with one frequency at a time. The Impedance-Chip Method employs a frequency-sweep sinusoid, which is an intermediate approach of the Sinc or Wideband Method and the Binary Method in terms of the excitation time duration. The time duration required to excite the entire target frequency range for each method is illustrated in Figure 5.22. It takes N_{freq} times longer for the Binary Method compared to the Sinc Method and the Wideband Method. The excitation time required for the Impedance-Chip Method, which depends on the sampling frequency and excitation period of each frequency, is typically longer than that for the Sinc and Wideband Methods and shorter than the Binary Method. Note that the total time duration on excitation and sensing until impedance signature generation is N_{avg} times T_{excite} because the impedance signature is calibrated from an averaged structural response, where N_{avg} is the number of average.

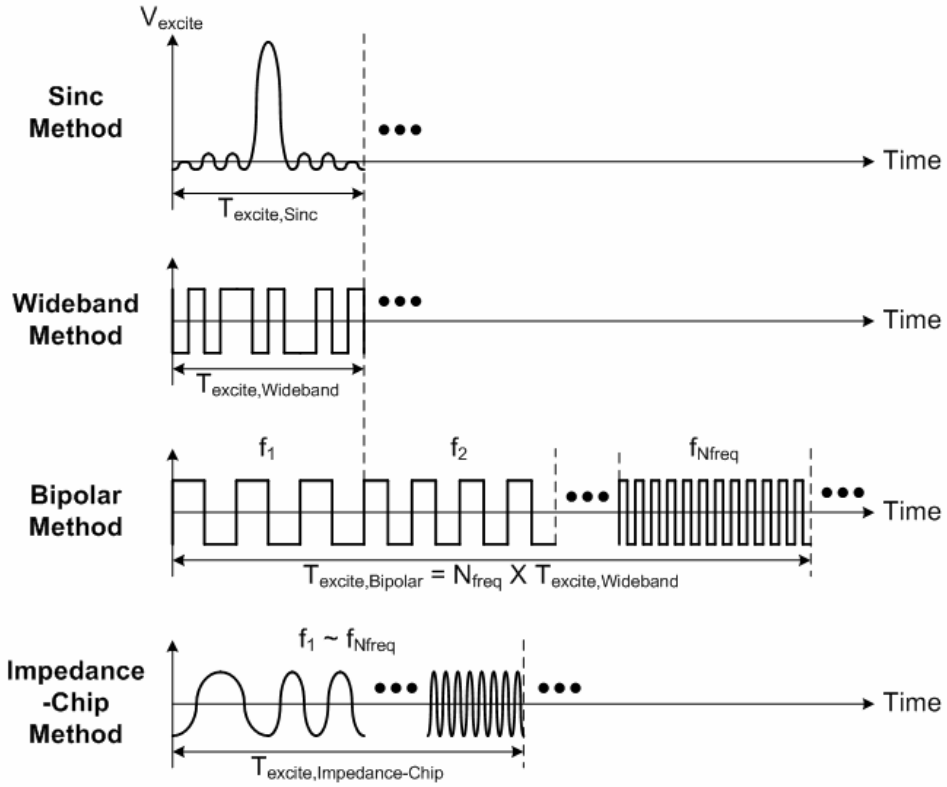

Figure 5.22 Excitation time of each method

One minor factor affecting the damage detection speed is the amount of calculation required to generate a damage metric from the measured structural response. The Binary Method calculates an SSD between the baseline signature and the current signature, while other methods calculate an RMSD after FFT. Assuming that an SSD and an RMSD entail the same calculation period, the Binary Method has an advantage over other methods by the duration of the FFT operation. However, time to perform an FFT is trivial compared to the excitation and sensing period. Therefore, approximate damage detection speeds can be expressed as equations (5.20) and (5.21), where v_{Sinc}, $v_{Wideband}$, $v_{Impedance\text{-}Chip}$ and v_{Binary} denote the damage detection speed of each method.

$$v_{Sinc} = v_{Wideband} = \left(N_{freq} - 1\right) \cdot N_{avg} \cdot v_{Bipolar} \tag{5.20}$$

$$v_{Sinc} = v_{Wideband} < v_{Impedance\text{-}Chip} < v_{Bipolar} \tag{5.21}$$

5.7.4 System Form Factor

System form factors are evaluated based on the actual system with which each method is realized. The Sinc Method relies on three PCBs, which are a DSP EVM, a DAC EVM, and an ADC EVM, and a minor system component is a sensing resistor. The Wideband Method is developed on two PCBs, which are a DSP EVM and an ADC EVM, and minor system components include op amps and resistors. The Binary Method can be developed either with a DSP EVM and an external circuitry consisting of op amps and resistors, or with one MCU EVM that can encompass the external circuitry on-board. These three methods are developed on completely localized systems, which do not require any separate devices or equipment.

The major difference of the Impedance-Chip Method from the Sinc, Wideband and Binary Methods is that the Impedance-Chip Method is developed on a non-localized system while the other methods are developed with completely localized and stand-alone systems. Since the Impedance-Chip Method requires a separate base station computer to perform structural condition assessment as well as a deployable system that performs the structural excitation and data collection, it is hard to compare the system form factors of the Impedance-Chip Method with other methods. Though it is claimed that the

Impedance-Chip Method is implemented on a PCB, the size of base station computer, which is indicated as α in Table 5.9, should not be ignored. The major system components are summarized in Table 5.9.

Table 5.9 System components of each method

Method	Major System Components	Dimension
Sinc	DSP EVM, DAC EVM, and ADC EVM	(22.3 cm X 11.5 cm) + (13.5 cm X 8.6 cm) + (10.2 cm X 8.6 cm)
Wideband	DSP EVM, and ADC EVM	(22.3 cm X 11.5 cm) + (10.2 cm X 8.6 cm)
Binary	DSP EVM and op amps	(12.7 cm X 7.6 cm) + (12.7 cm X 5 cm)
	MCU EVM and op amps	11.5 cm X 12.5 cm
Impedance-Chip	PCB with impedance chip and a computer	(5.5 cm X 3.7 cm) + α

5.7.5 Power Dissipation

Power dissipation has a close relationship with the system form factor and the computational complexity. The smaller system with less hardware components can run with lower power dissipation, and the simpler computation can relax the operating clock frequency and computational power requirements, which results in lower power dissipation. As summarized in Table 5.10, the power dissipation decreases from the Sinc Method to the Wideband Method and the Binary Method as expected. The power dissipation of the Impedance-Chip Method is lower than other three methods, because the Impedance-Chip Method is developed with a custom-designed PCB without including unnecessary components that are contained in the EVMs other three methods uses. Also, the power consumed by the base station computer, which is indicated as α in Table 5.10, is not encountered. The Binary Method, which is currently developed on a DSP EVM or a microcontroller EVM, is expected to have lower power dissipation when developed with a compact custom-designed PCB.

Table 5.10 System components of each method

Method	Power Dissipation (mW)
Sinc	4.01
Wideband	3.26
Binary	0.79
Impedance-Chip	$0.062 + \alpha$

Chapter 6:
Analytical Approach to SHM

6.1 Computer Aided Simulation and Evaluation

To evaluate the damage detection performance of the Binary Method, an SHM system with the Binary Method is modeled using the linear model of loaded PZT disclosed in Section 3.3. A set of simulation is conducted in MATLAB with loaded PZT models of a healthy structure and two representative damaged structures.

6.1.1 System Modeling

Unlike the ideal situation, determining a threshold value requires analytical effort in a practical environment. Though there are many possible sources of noise in reality, the background noise of an SHM system can be statistically modeled as additive white gaussian noise (AWGN) to the excitation signal as illustrated in Figure 6.1.

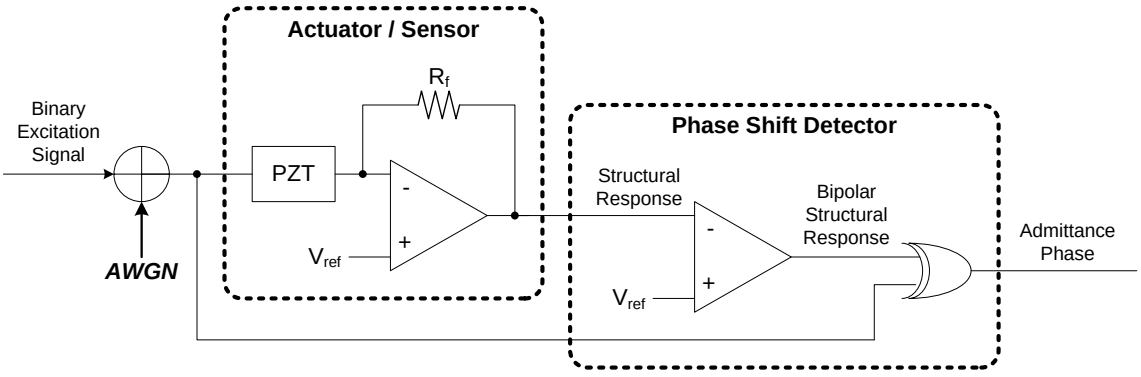

Figure 6.1 Block diagram of the Binary Method with AWGN

The system model of the Binary Method with AWGN is shown in Figure 6.2. Note that AWGN can be added before or after the actuator / sensor block because the actuator / sensor block uses a linear model of a loaded PZT. It is also assumed that, for a specific excitation frequency ω_0, the power density spectrums of $s(t)$ and $p(t)$ are maximum at the excitation frequency itself rather than at harmonics.

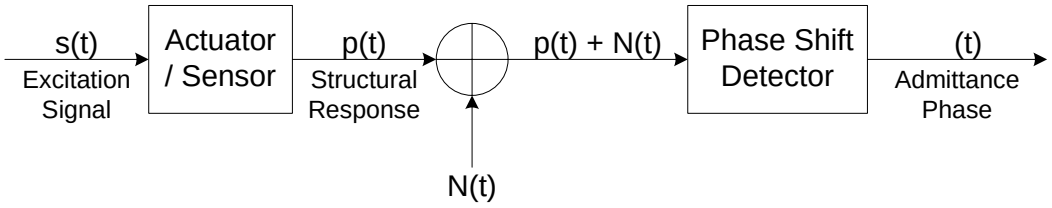

Figure 6.2 System model of the Binary Method with AWGN

6.1.2 Simulation Results

Based on the structural condition assessment method explained in Section 5.5 and the system model shown in Figure 6.2, a simulation is conducted with varying amounts of noise and threshold levels for detection error rate (DER) evaluation of the Binary Method. A detection result is claimed to be erroneous when either of the following two cases occurs: The first case occurs when the SHM system indicates that the structure is damaged when the structure is actually in a healthy status, which is called False Alarm. The other case occurs when the SHM system indicates that the structure is healthy when the structure is actually damaged, which is called Miss. The signal-to-noise ratio (SNR) is changed between -30 dB and 30 dB with a resolution of 1 dB, and the threshold value is changed from 500 to 3100 with a resolution of 65. Thus, a total of 2440 SNR-threshold pairs are simulated from 41 SNR values and 40 threshold values, and the False Alarm rate, Miss rate, and DER are measured from 3000 detection trials at each SNR-threshold pair. The target frequency range is from 12 KHz to 25 KHz, and the frequency resolution is 100 Hz, which results in 131 frequency components in the target frequency range. Two damage cases, Force 2 Position 1 and Force 1 Position 3, are simulated, and they are indicated as Strong Damage and Weak Damage, respectively.

Figure 6.3 shows the False Alarm rate. The False Alarm rate is high with small thresholds and low with large thresholds, and the smaller SNR gives a larger False Alarm rate. Figure 6.4 and Figure 6.5 present the Miss rate of Strong Damage and Weak Damage, respectively. Similar to the False Alarm rate, the Miss rate increases with a decreasing SNR. Also, the larger threshold value gives a higher Miss rate.

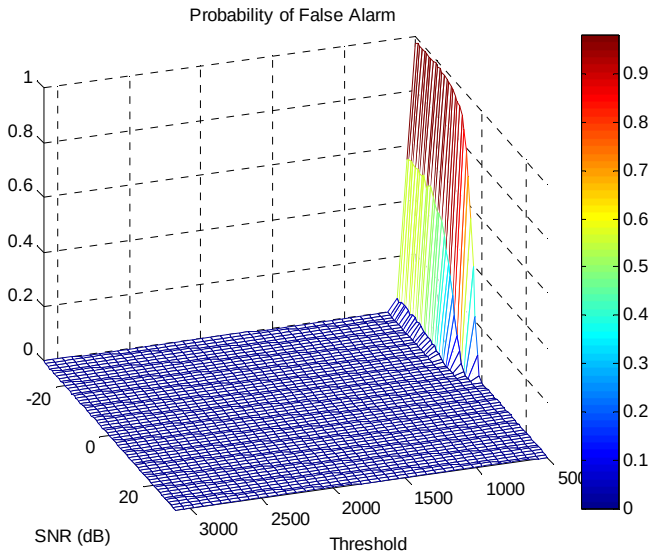

Figure 6.3 Probability of False Alarm – Detected as Damaged when the structure is Healthy

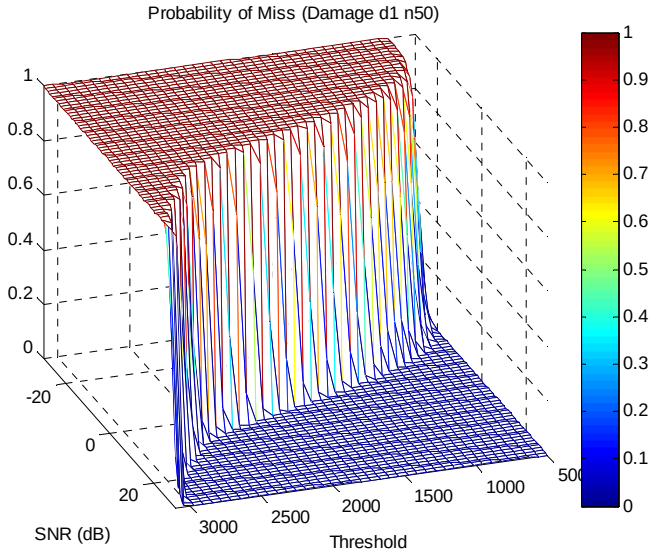

Figure 6.4 Probability of Miss (Strong damage) – Detected as Healthy when the structure is Damaged

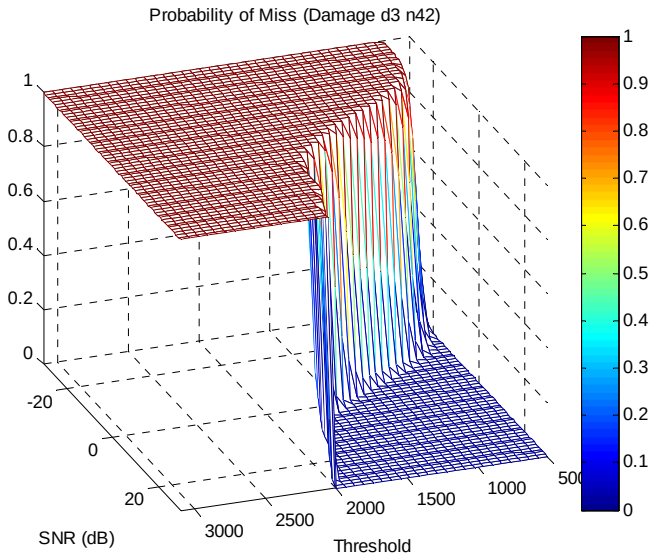

Figure 6.5 Probability of Miss (Weak damage) – Detected as Healthy when the structure is Damaged

Figure 6.6 shows the DER of Strong Damage, and Figure 6.7 shows the DER of Weak Damage. Both damage cases have the highest noise immunity at a threshold 695, at which they start having detection errors at an SNR of -11 dB. The DER of Strong Damage and Weak Damage at that threshold and SNR is 3.3e-4.

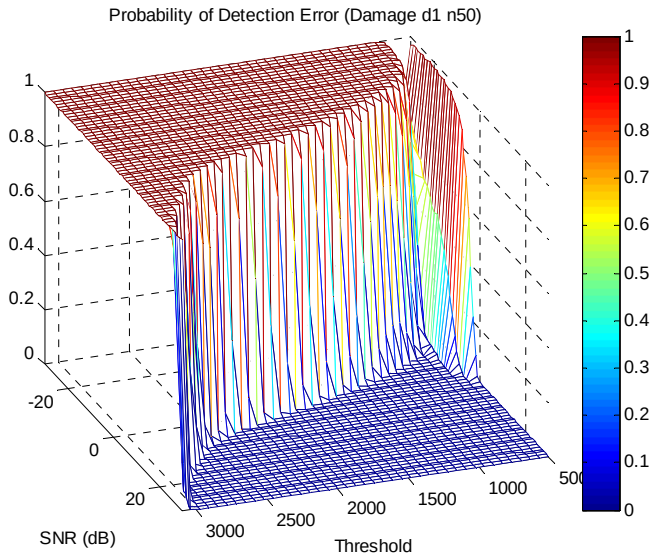

Figure 6.6 Probability of detection error (Strong damage) - Detected as Damaged when the structure is Healthy or detected as Healthy when the structure is Damaged

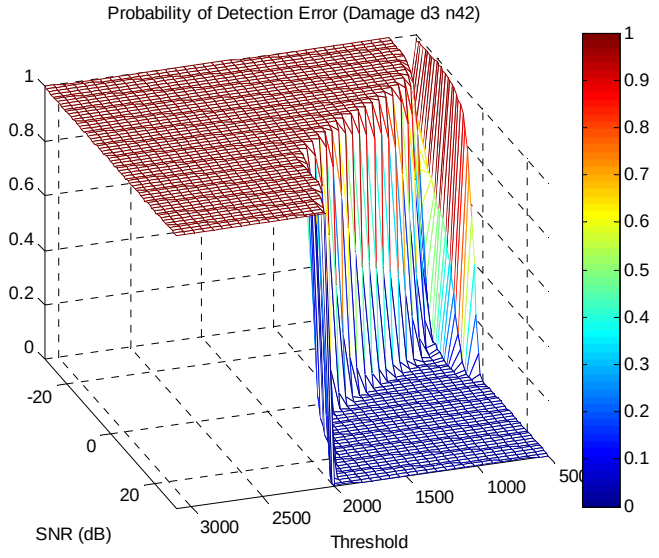

Figure 6.7 Probability of detection error (Weak damage) - Detected as Damaged when the structure is Healthy or detected as Healthy when the structure is Damaged

Traditionally, the threshold was decided based on measurements by actually damaging a test structure, which is a replica of the real structure where the SHM system will be applied. The traditional threshold decision method has drawbacks: First, the test

structure cannot replicate all the mechanical conditions of the actual structure though the test structure is a replica of the actual structure. Second, while the traditional method can simulate only a limited set of damage cases in a lab environment, the characteristics of the actual damage that will occur on the actual structure is unknown. Third, evaluating a test structure for threshold decision is time consuming and costly. Thus, it is not guaranteed whether the preset threshold can actually distinguish the healthy and damaged structural condition after deployment, and how much accuracy the SHM system can provide.

Also, as the threshold is fixed through the operation, the SHM system is not assured to provide the same degree of damage detection quality as when it was tested in the lab, when the environmental noise that the real structure is exposed to is changed. Since practical structures where the proposed SHM methods are applied have a high chance of being exposed to noisy environments, finding a perfect threshold value that can always provide a correct damage detection result is not a trivial task. In some cases, it might not be feasible to determine such a threshold level, and the detection result tends to have a certain error rate as presented in the simulation results. Therefore, an analytical approach is expected to detect various types and sizes of damage with a constant reliable detection performance in a practical environment.

6.2 System Observation in Phase Vector Domain

The impedance-based SHM monitors an impedance signature that contains structural integrity information at each excitation frequency. In the Binary Method, the impedance signature is a phase of the structure's electrical admittance. Thus, it is assumed that the impedance signature is a vector in an arbitrary phase vector domain for convenience of analysis. In this section, it will be shown how to composite the vector domain, and how each component of the vector domain can be justified as an orthogonal basis.

6.2.1 Phase Vector Domain

The structural response $p(t)$ of an excitation frequency ω_0 without AWGN is a complex signal expressed in equation (6.1), where A_0 and θ_0, the envelope and phase of $p(t)$, are constants.

$$\begin{aligned} p(t) &= A_0 \cos(\omega_0 t + \theta_0) \\ &= A_0 \cos(\theta_0)\cos(\omega_0 t) - A_0 \sin(\theta_0)\sin(\omega_0 t) \end{aligned} \tag{6.1}$$

The gaussian noise $n(t)$ added to $p(t)$ can be considered as a sample function of a zero-mean, wide-sense stationary gaussian bandpass process $N(t)$ with power $E\left[N^2(t)\right] = \sigma^2$ [55]. As the structural response $p(t)$ is a bandpass signal, $N(t)$ can be written in an equivalent form

$$N(t) = X(t)\cos(\omega_0 t) - Y(t)\sin(\omega_0 t) \tag{6.2}$$

where the processes $X(t)$ and $Y(t)$ are uncorrelated, and the zero-mean, gaussian, lowpass processes have the same powers $E\left[N^2(t)\right] = E\left[X^2(t)\right] = E\left[Y^2(t)\right] = \sigma^2$ [55].

Then, the sum of the structural response and the noise can be written as

$$\begin{aligned} p(t) + N(t) &= \left[A_0 \cos(\theta_0) + X(t)\right]\cos(\omega_0 t) - \left[A_0 \sin(\theta_0) + Y(t)\right]\sin(\omega_0 t) \\ &= A(t)\cos\left[\omega_0 t + \Theta(t)\right] \end{aligned} \tag{6.3}$$

where $A(t)$ and $\Theta(t)$ are the envelope and phase of $p(t) + N(t)$. Note that the constant envelope and phase of $p(t)$ become functions of time after adding the noise $N(t)$. $A(t)$ and $\Theta(t)$ can be considered as transformations of $X(t)$ and $Y(t)$ as shown in equations (6.4) and (6.5).

$$A(t) = T_A(X, Y) = \sqrt{\left[A_0 \cos(\theta_0) + X(t)\right]^2 + \left[A_0 \sin(\theta_0) + Y(t)\right]^2} \tag{6.4}$$

$$\Theta(t) = T_\Theta(X, Y) = \tan^{-1}\left[\frac{A_0 \sin(\theta_0) + Y(t)}{A_0 \cos(\theta_0) + X(t)}\right] \tag{6.5}$$

Since the impedance signature of the Binary Method is obtained from the phase of the structural response, the probability density of $\Theta(t)$, which is the phase pf the structural response affected by AWGN, given in equation (6.5) should be analyzed.

The structural response $p(t)$ and the AWGN $N(t)$ can be represented as vectors. For instance, Figure 6.8 (a) illustrates a signal vector $\vec{p}$, whose magnitude is $\sqrt{2}A_0$ and angle is θ_0, and Figure 6.8 (b) shows representative noise vectors with a magnitude of σ and arbitrary angles, where σ^2 is the power of AWGN $N(t)$. The noisy structural response, which is analyzed to obtain the phase shift through the actuator / sensor block and resultantly becomes a basis of an impedance signature, is a sum of those two vectors, $\vec{p}$ and $\vec{N}$ as shown in Figure 6.8 (c). Due to the addition of AWGN to the signal vector, the resulting signal vector has variable magnitude and phase.

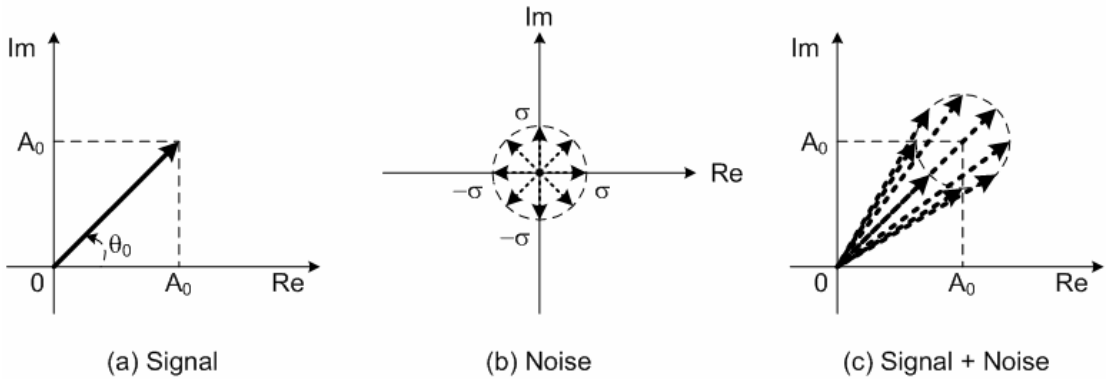

Figure 6.8 Signal and noise as vectors

Note that, as shown in Figure 6.9, the structural response has a maximum phase deviation of $\pm\theta_N$ due to the AWGN. Thus, the output of the phase shift detector, $\Theta(t)$, has a value within a range of $\theta_0 \pm \theta_N$ depending on the power level of AWGN $N(t)$, rather than an ideal value of θ_0. $\Theta(t)$ is rewritten in equation (6.6), where $r(t)$ is the ideal phase shift without existence of AWGN, and $N_\theta(t)$ is the phase deviation on $r(t)$ caused by $N(t)$.

$$\begin{aligned}\Theta(t) &= r(t) + N_\theta(t) \\ &= \theta_0 + N_\theta(t)\end{aligned} \tag{6.6}$$

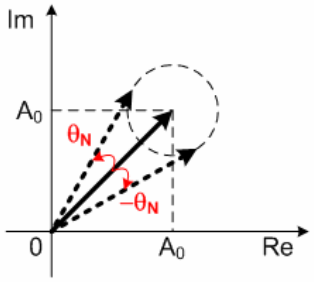

Figure 6.9 Phase deviation caused by the noise

Since the noise $N(t)$ added to the structural response $p(t)$ has a zero-mean gaussian distribution with power of σ^2, the probability density of $N(t)$ seen in a cross section on a straight line with an arbitrary angle passing through the origin follows a gaussian distribution, whose mean is zero and variance is σ^2 as shown in Figure 6.10.

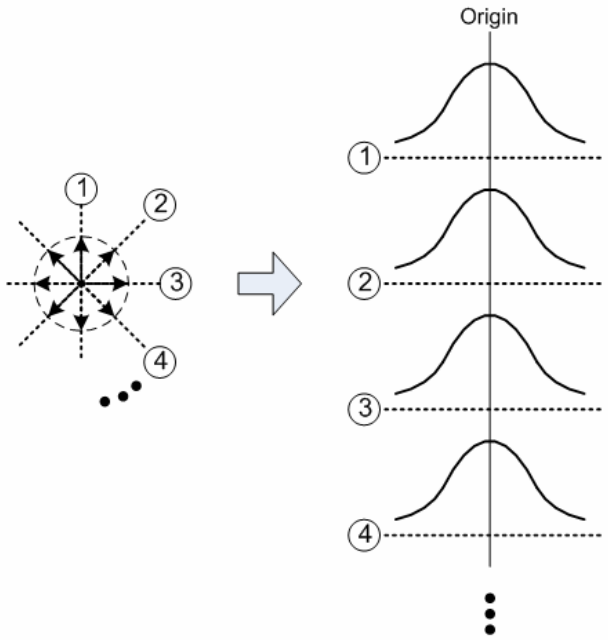

Figure 6.10 Cross sections of noise probability density at different phases

Let us examine the relationship between the AWGN $N(t)$ and the phase deviation $N_\theta(t)$. Figure 6.11 shows an example when the SNR of $p(t)+N(t)$ is 3 dB, as the signal power is $2A_0^2$ and the noise power is A_0^2. In this case, as shown in Figure 6.11 (c) and (d), the phase deviation $N_\theta(t)$ caused by the AWGN $N(t)$ falls in the range of $\pm(\pi/4)$. Notice that the arc tangent is roughly linear for the input range of ±1 and the output range of $\pm(\pi/4)$ as shown in Figure 6.12 and provides a correlation coefficient of 0.997 when compared with a linear approximation in that particular range. Therefore, assuming that the phase deviation $N_\theta(t)$ caused by the AWGN $N(t)$ is in the range of $\pm(\pi/4)$, or equivalently that the SNR of $p(t)+N(t)$ is at least 3 dB, the phase of $p(t)+N(t)$ can be approximated as a linear transformation of $X(t)$ and $Y(t)$ based on equation (6.5).

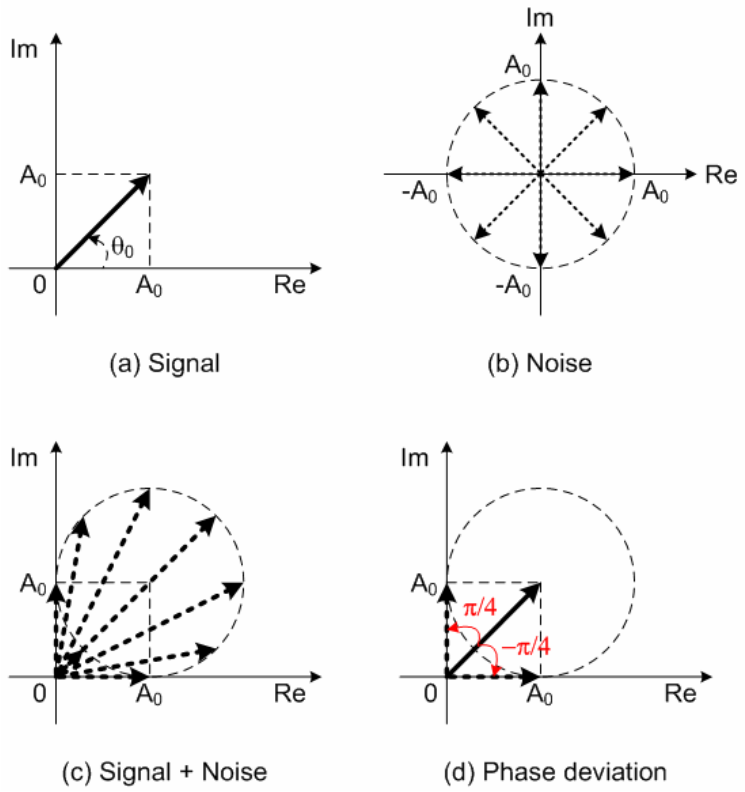

Figure 6.11 Signal and noise vectors with 3-dB SNR

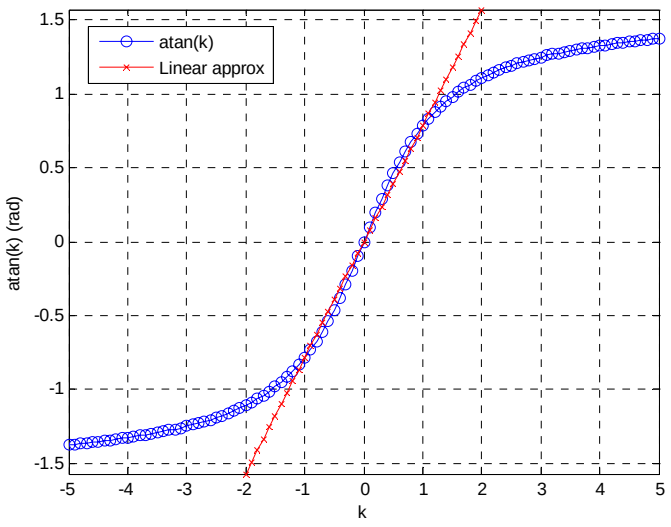

Figure 6.12 Linear approximation of tan^{-1}

Since $\Theta(t)$ is a linear transformation of $X(t)$ and $Y(t)$, which are uncorrelated gaussian processes with zero-mean and variance of σ^2, $\Theta(t)$ can also be estimated as a gaussian process with a mean of θ_0 and a variance of ${\sigma_\theta}^2$. This means that the phase deviation $N_\theta(t)$ is also a gaussian noise whose probability density function is expressed in equation (6.7) because $r(t)$ is a constant θ_0 as presented in equation (6.6).

$$f_{N_\theta}(n_\theta) = \frac{e^{-{n_\theta}^2/2{\sigma_\theta}^2}}{\sqrt{2\pi}\sigma_\theta} \tag{6.7}$$

Note that $N_\theta(t)$ is a gaussian noise with a zero-mean and variance of ${\sigma_\theta}^2$, and $\Theta(t)$ is the sum of a constant and a gaussian noise.

The system analysis conducted for one particular excitation frequency can be extended to all excitation frequency components in the target frequency range considering the phase of each excitation frequency as a basis of phase vector. When there are *k* frequency components in the target frequency range, *k* phase shift values acquired through the target frequency range can be considered as a k-dimensional vector, each as a basis which indicates the phase shift at each excitation frequency with gaussian

noise, as expressed in equation (6.8) and (6.9). Each basis experiences an independent gaussian noise.

$$\overrightarrow{\Theta} = \vec{r} + \overrightarrow{N_\theta} \tag{6.8}$$

$$\begin{aligned} \begin{pmatrix} \Theta_1 & \Theta_2 & \cdots & \Theta_k \end{pmatrix} &= \begin{pmatrix} r_1 & r_2 & \cdots & r_k \end{pmatrix} + \begin{pmatrix} N_{\theta,1} & N_{\theta,2} & \cdots & N_{\theta,k} \end{pmatrix} \\ &= \begin{pmatrix} \theta_1 & \theta_2 & \cdots & \theta_k \end{pmatrix} + \begin{pmatrix} N_{\theta,1} & N_{\theta,2} & \cdots & N_{\theta,k} \end{pmatrix} \end{aligned} \tag{6.9}$$

Then, the baseline signature and a current signature are k-dimensional vectors respectively as expressed in equations (6.10) and (6.11).

$$\overrightarrow{\Theta_{base}} = \overrightarrow{r_{base}} + \overrightarrow{N_{\theta,base}} \tag{6.10}$$

$$\overrightarrow{\Theta_{curr}} = \overrightarrow{r_{curr}} + \overrightarrow{N_{\theta,curr}} \tag{6.11}$$

As the structural condition is determined by comparing the baseline signature and a current signature, the difference between $\overrightarrow{\Theta_{base}}$ and $\overrightarrow{\Theta_{curr}}$ is quantified. As a first step, the difference vector $\overrightarrow{\Theta_{diff}}$ is defined as

$$\begin{aligned} \overrightarrow{\Theta_{diff}} &= \overrightarrow{\Theta_{curr}} - \overrightarrow{\Theta_{base}} \\ &= \left(\overrightarrow{r_{curr}} + \overrightarrow{N_{\theta,curr}}\right) - \left(\overrightarrow{r_{base}} + \overrightarrow{N_{\theta,base}}\right) \\ &= \left(\overrightarrow{r_{curr}} - \overrightarrow{r_{base}}\right) + \left(\overrightarrow{N_{\theta,curr}} - \overrightarrow{N_{\theta,base}}\right) \\ &= \overrightarrow{r_{diff}} + \overrightarrow{N_{\theta,diff}} \end{aligned} \tag{6.12}$$

Note that for a specific structural condition the signal vector $\left(\overrightarrow{r_{curr}} - \overrightarrow{r_{base}}\right)$ is a constant vector, while the noise vector $\left(\overrightarrow{N_{\theta,curr}} - \overrightarrow{N_{\theta,base}}\right)$ varies over measurements. When the current structural condition is healthy, the signal vector $\left(\overrightarrow{r_{curr}} - \overrightarrow{r_{base}}\right)$ is simply zero, while it becomes a specific damage vector if the structure is damaged.

The metric is then defined as a magnitude of the difference vector $\overrightarrow{\Theta_{diff}}$, which is equivalent to a vector distance between the baseline signature vector $\overrightarrow{\Theta_{base}}$ and the current signature vector $\overrightarrow{\Theta_{curr}}$ as expressed in equation (6.13).

$$Metric = \left|\overrightarrow{\Theta_{diff}}\right| = \sqrt{\sum_{i=1}^{k}\left(r_{diff,i} + N_{\theta,diff,i}\right)^2} \tag{6.13}$$

The calculated metric is compared with a threshold value to determine whether the structure is intact or damaged. A metric larger than the threshold value indicates that the structure is damaged. In reality, there are two possible reasons of an increased metric value. One case is when the structure is really damaged. In this 'damaged' case, the change on the metric is mainly due to the change on the signal vector $\overrightarrow{r_{curr}}$ rather than the change on the noise vector $\overrightarrow{N_{\theta,curr}}$. The other case is when the structure remains in healthy condition, but the background noise level is elevated. In this 'noisy' case, the change on the metric is mainly due to the change on the noise vector $\overrightarrow{N_{\theta,curr}}$ rather than the signal vector $\overrightarrow{r_{curr}}$. The typical structural condition assessment method compares only a metric, a scalar value which quantitatively represents the deviation of the structural condition from the baseline condition. However, a metric comparison with a threshold cannot distinguish whether the increment on the metric is cause by an actual damage or by increased environmental noise. Also, it is hard to determine a threshold value that can provide a constant damage detection quality through the operation of the SHM system in a time-variant environment.

6.2.2 Spatial Damage Detection and Quality Control

A fundamental question that arises regarding the performance of the SHM system is the sensitivity of the damage detection. The size or the strength of the damage can be quantified in terms of damage distance as presented in equation (6.13). Though it is not possible to provide a specific damage distance that an SHM system can detect due to the noise $N_\theta(t)$ included in the measured phase $\Theta(t)$, it is feasible to provide a constant DER that an SHM system can maintain with a specific damage distance provided. Since

the gaussian noise $N_\theta(t)$ is the obstacle in maintaining the damage detection quality, $N_\theta(t)$ is the target to control.

One efficient way to cancel out the background noise is an averaging. Since the background noise is a zero-mean gaussian process, the SNR can be improved by taking an average at each component of the phase difference vector $\Theta_{diff,i}$. Averaging can be considered as a normalized integration, which is a perfect low pass filter for a DC signal. According to the expression of the integration in Laplacian, which is *1/s*, the integration has an infinite response at DC and filters out any noise but a DC component. Since our interest is to measure a static vector component, which means DC, integration is a perfect choice to get rid of any noise component outside DC. The reason considering an averaging instead of an accumulation, which is analogue to integration in a digital domain, is that averaging normalizes accumulation, so that it insures a 0-dB gain at DC. However, since an SHM is a time-variant system, the order should be limited by the bandwidth of the system.

When the minimum damage distance that the SHM system is required to detect is given, the length of averaging can be determined based on the measured noise level at a particular excitation frequency, and the system's damage detection quality can be controlled. Consider one element of the difference vector $\Theta_{diff,i}$ given in equation (6.12). Since the phase difference calculated from the baseline signature and the current signature has a gaussian distribution centered at zero when the structure is healthy and at a damage distance when the structure is damaged, the probability density function (PDF) can be illustrated as Figure 6.13. Thus, by determining the threshold between zero and a given damage distance as $m_{damage}/2$, one can minimize the occurrence of erroneous detection results.

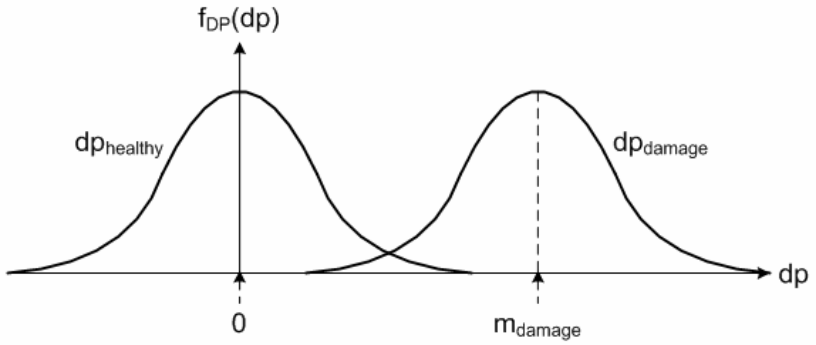

Figure 6.13 Probability density function of damage metric in a practical environment

Based on the calculated standard deviation of the current measurements σ_{curr}, the confidence level of the detection can be obtained. In the relationship between the confidence interval and the confidence level provided in Table 6.1, notice that the confidence level for damage detection is different from the regular confidence level. As shown in Figure 6.14, the left side of the PDF from a healthy structure and the right side of the PDF from a damaged structure are considered as a correct decision, while the confidence interval give in Table 6.1 is the distance from the mean to both sides of the PDF as shown in Figure 6.15. Thus, the confidence level of damage detection is 50% plus a half of the regular confidence level. Thus, based on Table 6.1, the confidence level of the damage detection can be found for a given damage distance.

Table 6.1 Confidence level

Confidence interval ($\times\sigma$)	Confidence level (%)	Confidence level for damage detection (%)
0.674	50.0	75.00
1.000	68.3	84.15
1.645	90.0	95.00
1.880	94.0	97.00
2.326	98.0	99.00

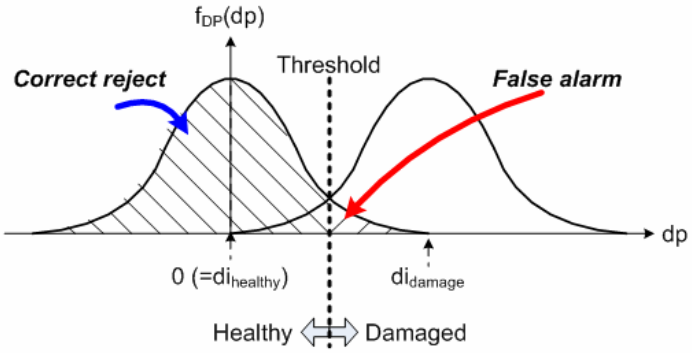

(a) Healthy => Correct reject / False alarm

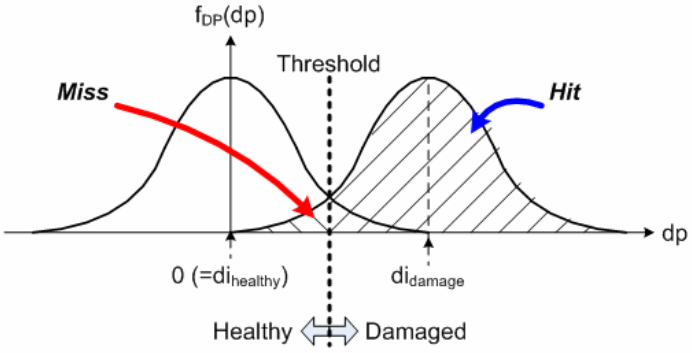

(b) Damaged => Hit / Miss

Figure 6.14 Correct reject / False alarm / Hit / Miss

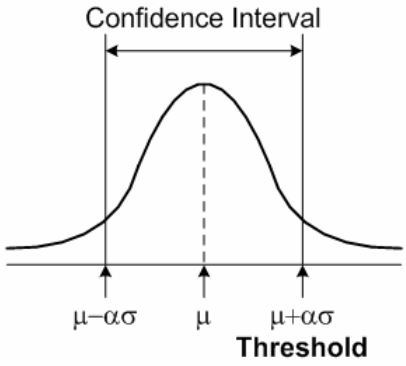

Figure 6.15 Confidence interval

Consider a case when the found confidence level based on $\sigma_{curr,i}$ is lower than the required confidence level at a given damage distance m_{damage}. In this case, current signature $\overrightarrow{\Theta_{curr}}$ should be averaged for a certain number of times to meet the required confidence level. Averaging a gaussian process with a mean of μ and a variance of σ^2 produce a new gaussian process with a mean of μ and a variance of σ^2 / N_{avg}, where N_{avg} is the length of averaging. Thus, by averaging the current signature $\Theta_{diff,i}$ for N_{avg} times, one can lower the standard deviation from $\sigma_{curr,i}$ to $\sigma_{curr,i} / \sqrt{N_{avg}}$, and resultantly acquires a higher confidence level that can meet the damage detection quality requirement.

This procedure is also valid when the background noise level is increased from σ_1^2 to σ_2^2, but the structure is remained healthy as shown in Figure 6.16. Then, the threshold found based on the noise power of σ_1^2 cannot provide the required confidence level. Since the threshold is determined as a half of the minimum damage distance that the SHM should detect, the threshold cannot be increased as well. Therefore, the current signature $\Theta_{diff,i}$ is averaged a certain number of times to increase SNR. The noise power of the averaged signal, when the length of averaging is N_{avg}, is σ_2^2 / N_{avg}, where the noise power of un-averaged signature is σ_2^2. Therefore, the required confidence level of the damage detection can be maintained by finding an appropriate N_{avg} that makes σ_2^2 / N_{avg} match the value of σ_1^2 through the SHM operation. Note that since the SHM system is a time-variant system, the measured phase samples cannot be averaged for a while, and there is a limit on the SNR that can be improved by the averaging.

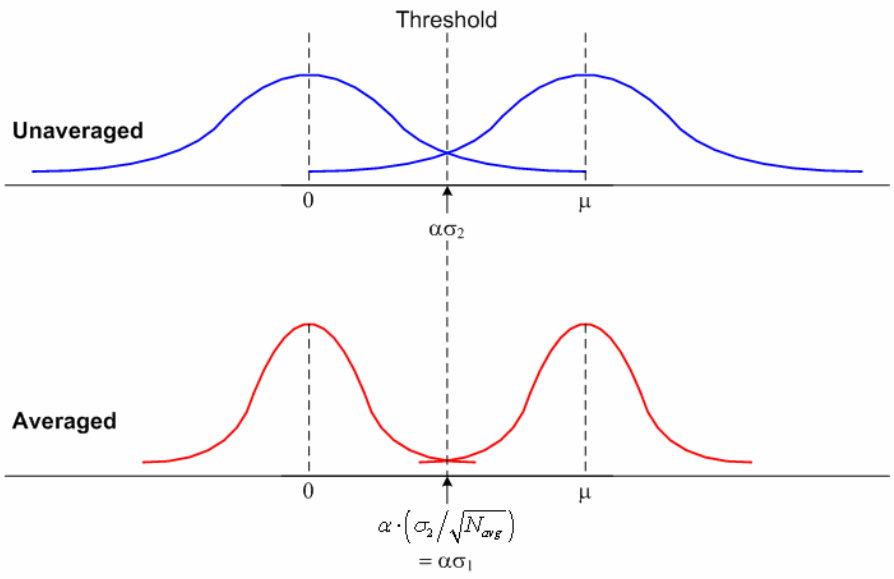

Figure 6.16 Confidence level maintained by averaging

This procedure is repeated for each element of the difference vector $\overrightarrow{\Theta_{diff}}$ to control the damage detection quality. Typically, a fielded SHM system will assess the structural condition once or twice a day. Thus, though the averaging process increases the computational complexity and the processing time to acquire one assessment result, the overall performance of the SHM system will not be affected. Also, this quality control technique benefits from the Binary Method, as the linear transformation of the AWGN to the gaussian phase noise is not applicable to the traditional structural condition assessment relying on the conductance of the measured admittance.

Chapter 7:
Conclusion

For massive and complicated new structures as well as aging structures in operation, locating damage and maintaining the structural integrity become critical. Hence, SHM technology that can identify whether the structure is intact or damaged gains increased attention, and the major issue in SHM research is how to develop a deployable SHM system. The impedance-based SHM utilizing a piezoelectric ceramic as a collocated actuator / sensor is favored over other NDE techniques, such as Global Vibration Method, Ultrasonic Testing, Acoustic Emission, and Impact-Echo Testing, in terms of easy interpretation on the measured data, low system development cost, wide sensing region, and high sensitivity to minor defects. This dissertation investigates properties of piezoelectric ceramic, proposes two low-power system design approaches for impedance-based SHM, and provides an analytical method to control the detection quality.

First, Chapter 3 investigated behaviors of piezoelectric ceramics and proposed an electrical model in order to enable system level analysis and evaluation of the SHM system. Unloaded and loaded piezoelectric ceramics were electrically modeled with lumped circuit components to provide a linear response. The proposed electrical model can be obtained through a systematic procedure by analyzing the actual measured electrical impedance of a piezoelectric ceramic. The linear electrical model can accelerate the procedure of system analysis by enabling simulations with parameters for various environmental conditions, which cannot be mimicked in the lab environment with a test structure.

Next, Chapter 4 proposed the Wideband Method, which uses a PN sequence instead of a signal with a particular waveform for the excitation of structure. The bandwidth of the target frequency range is controlled by the length of the PN sequence,

and the center frequency of the target frequency range is adjusted by the frequency of a carrier signal that upconverts the PN sequence. Since the PN excitation signal is a binary sequence, the need for a DAC in an SHM system is circumvented. The Wideband Method also simplifies the generation of the excitation signal, which resultantly reduces the development cost by relaxing the performance requirements of the computation unit. A prototype system was implemented on a DSP board with an ADC daughter card. The damage detection performance of the Wideband Method was compatible with that of the Sinc Method, while the system form factor is decreased by the size of a DAC EVM, and the power dissipation is reduced by 17%.

In Chapter 5, a breakthrough approach called the Binary Method is proposed, which exploits binary signaling for both excitation of the structure and measurement of the structural response. The Binary Method is the first approach which exploits the phase of the admittance based on the fact that the phase and real part of the admittance has a high correlation, while the traditional and all previous impedance-based SHM systems relied on the conductance. Since the phase can be obtained by measuring the polarity of the structural response and then compared with the original excitation signal, the Binary Method eliminates the need for a DAC and an ADC. Binary signaling also removes the DFT operation, which was necessary for previous structural condition assessment method. Two prototype systems were developed: one with a DSP board and the other with a microcontroller board. The DSP based prototype of the Binary Method reduced the power dissipation by 80% compared to the prototype implementing the Sinc Method and by 76% compared to the prototype implementing the Wideband Method. The microcontroller-based prototype of the Binary Method reduced the power dissipation by 79% compared to the prototype implementing the Sinc Method and by 74% compared to the prototype implementing the Wideband Method.

Finally, an analytical method to assess the quality of the damage detection for the Binary Method is explored. The measured phase at each excitation frequency is considered as a basis, which composes a phase vector domain. The metric was calculated as a vector distance between the baseline signature and the current signature. The quality of the damage detection can be described in terms of the confidence level for a given

damage distance. This is the first analytical approach to provide damage detection sensitivity based on damage distance and confidence level.

Appendix A – Publications

J. Kim, B.L. Grisso, J.K. Kim, D.S. Ha, and D.J. Inman, "Electrical Modeling of Piezoelectric Ceramics for Analysis and Evaluation of Sensory Systems," *IEEE Sensors Applications Symposium*, February 2008.

B.L. Grisso, J. Kim, D.S. Ha, and D.J. Inman, "Sensor Diagnostics for Autonomous Digital Structural Health Monitoring Systems," *SEM Conference on Structural Dynamics (IMAC XXVI)*, February 2008.

B.L. Grisso, J. Kim, J.R. Farmer, D.S. Ha, and D.J. Inman, "Autonomous Impedance-Based SHM Utilizing Harvested Energy," *International Workshop on Structural Health Monitoring*, pp. 1373-1380, September 2007.

J. Kim, B.L. Grisso, D.S. Ha, and D.J. Inman, "An All-Digital Low-Power Structural Health Monitoring System," *IEEE Conference on Technologies for Homeland Security*, pp. 123-128, May 2007.

J. Kim, B.L. Grisso, D.S. Ha, and D.J. Inman, "Digital Wideband Excitation Technique for Impedance-Based Structural Health Monitoring Systems," *IEEE International Symposium on Circuits and Systems*, pp. 3566-3569, May 2007.

J. Kim, B.L. Grisso, D.S. Ha, and D.J. Inman, "A System-On-Board Approach for Impedance-Based Structural Health Monitoring," *SPIE International Symposium on Smart Structures and Materials*, vol. 6529, pp. 65290O1-65290O9, March 2007.

R.C. Palat, J. Kim, J.-S. Lee, D.S. Ha, C.D. Patterson, and J.H. Reed, "Reconfigurable Modem Architecture for CDMA Based 3G Handsets," *Software Defined Radio Technical Conference*, Session 1.4-01, November 2005.

J. Kim, D.S. Ha, and J.H. Reed, "A New Reconfigurable Modem Architecture for 3G Multi-Standard Wireless Communication Systems," *IEEE International Symposium on Circuits and Systems*, pp. 1051-1054, May 2005.

Appendix B – Patents

J. Kim, B.L. Grisso, D.S. Ha, and D.J. Inman, "System and Method for Digital Wideband Excitation Technique for Impedance-Based Structural Health Monitoring Systems," Application no. 60/973999, September 2007.

J.-W. Heo, R.C. Palat, D.S. Ha, J.H. Reed, J. Kim, and J.-S. Lee, "Communication System with Reconfigurable Hardware Structure and Reconfiguration Method Therefor," Publication no. 20060105802, May 2006.

J.-W. Heo, R.C. Palat, D.S. Ha, J.H. Reed, J. Kim, and J.-S. Lee, "Reconfigurable Hardware Structure Supporting Multiple Wireless Transmission Standards," Republic of Korea Patent Pending.

Bibliography

[1] A.S. Sedra and K.C. Smith, Microelectronic Circuits, 5th edition, Oxford University Press, 2003.

[2] S. Franco, Design with Operational Amplifiers and Analog Integrated Circuits, 3rd edition, McGraw-Hill, 2002.

[3] T.H. Lee, The Design of CMOS Radio-Frequency Integrated Circuits, 2nd edition, Cambridge University Press, 2003.

[4] L.W. Couch, Digital and Analog Communication Systems, 6th edition, Prentice Hall, 2001.

[5] J.G. Proakis, Digital Communications, 4th edition, McGraw-Hill, 2001.

[6] G.E. Carlson, Signal and Linear System Analysis, Houghton Mifflin, 1992.

[7] B. Sklar, Digital Communications, 2nd edition, Prentice Hall, 2001

[8] D.J. Inman, C.R. Farrar, V. Lopes Jr., and V. Steffen Jr., Damage Prognosis for Aerospace, Civil and Mechanical Systems, Wiley 2005.

[9] G. Park, H. Sohn, C.R. Farrar, and D.J. Inman, "Overview of Piezoelectric Impedance-Based Health Monitoring and Path Forward," *The Shock and Vibration Digest*, vol. 35, no. 6, pp. 451-463, November 2003.

[10] D.M. Peairs, G. Park, and D.J. Inman, "Reducing the Cost of Impedance-Based Structural Health Monitoring," *SPIE International Symposium on Smart Structures and Materials*, vol. 4702, pp. 301-310, March 2002.

[11] D.M. Peairs, G. Park, and D.J. Inman, "Low Cost Impedance Monitoring Using Smart Materials," *European Workshop on Structural Health Monitoring*, pp. 442-449, July 2002.

[12] D.M. Peairs, G. Park, and D.J. Inman, "Improving Accessibility of the Impedance-Based Structural Health Monitoring Method," *Journal of Intelligent Material Systems and Structures*, vol. 15, pp. 129-139, February 2004.

[13] B.L. Grisso and D.J. Inman, "Developing an Autonomous On-Orbit Impedance-Based SHM for Thermal Protection Systems," *International Workshop on Structural Health Monitoring*, pp. 435-442, September 2005.

[14] D.J. Inman and B.L. Grisso, "Towards Autonomous Sensing," *SPIE International Symposium on Smart Structures and Materials*, vol. 6174, pp. 248-254, February 2006.

[15] J. Kim, B.L. Grisso, D.S. Ha, and D.J. Inman, "Digital Wideband Excitation Technique for Impedance-Based Structural Health Monitoring Systems," *IEEE International Symposium on Circuits and Systems*, pp. 3566-3569, May 2007.

[16] J. Kim, B.L. Grisso, D.S. Ha, and D.J. Inman, "An All-Digital Low-Power Structural Health Monitoring System," *IEEE Conference on Technologies for Homeland Security*, pp. 123-128, May 2007.

[17] J. Kim, B.L. Grisso, D.S. Ha, and D.J. Inman, "A System-On-Board Approach for Impedance-Based Structural Health Monitoring," *SPIE International Symposium on Smart Structures and Materials*, vol. 6529, pp. 65290O1-65290O9, March 2007.

[18] C. Liang, F.P. Sun, and C.A. Rogers, "Coupled Electro-mechanical Analysis of Adaptive Material Systems – Determination of the Actuator Power consumption and System Energy Transfer," *Journal of Intelligent Material Systems and Structures*, vol. 5, pp. 12-20, January 1994.

[19] C. Liang, F.P. Sun, and C.A. Rogers, "An Impedance Method for Dynamic Analysis of Active Material Systems," *ASME Journal of Vibration and Acoustics*, vol. 116, pp. 120-128, January 1994.

[20] F.P. Sun, Z. Chaudhry, C. Liang, and C.A. Rogers, "Truss Structure Integrity Identification Using PZT Sensor-Actuator," *Journal of Intelligent Material Systems and Systems*, vol. 6, pp. 134-139, January 1995.

[21] A.N. Zagrai, and V. Giurgiutiu, "Electromechanical Impedance Method for Crack Detection in Thin Plates," *Journal of Intelligent Material Systems and Structures*, vol. 12, pp. 709-718, October 2002.

[22] K. Tseng, and A. Naidu, "Non-Parametric Damage Detection and Characterization Using Smart Piezoceramic Materials," *Smart Materials and Structures*, vol. 11, pp. 317-329, June 2002.

[23] V. Lopes, G. Park. H. Cudney, and D.J. Inman, "Impedance-Based Structural Health Monitoring with Artificial Neural Networks," *Journal of Intelligent Material Systems and Structures*, vol. 11, no. 3, pp. 206-214, March 2000.

[24] F. Sun, Z. Chaudhry, and C.A. Rogers, "Automated Real-Time Structure Health Monitoring via Signature Pattern Recognition," *SPIE International Symposium on Smart Structures and Materials*, vol. 2443, pp. 236-247, May 1995.

[25] V. Raju, G. Park, and H. Cudney, "Impedance-Based Health Monitoring Technique of Composite Reinforced Structures," *International Conference on Adaptive Structures and Technologies*, pp. 448-457, October 1998.

[26] V. Raju, "Implementing Impedance-Based Health Monitoring Technique," Master's Thesis, Virginia Tech, November 1997.

[27] V. Giurgiutiu and C.A. Rogers, "Recent Advancements in the Electro-Mechanical (E/M) Impedance Method for Structural Health Monitoring and NDE," *SPIE Conference on Smart Structures and Materials*, vol. 3329, pp. 536-547, July 1998.

[28] S. Bhalla, A.S.K. Naidu, C.K. Soh, "Influence of Structure-Actuator Interactions and Temperature on Piezoelectric Mechatronic Signatures of NDE," *SPIE International Symposium on Smart Materials, Structures and Systems*, vol. 5062, pp. 263-269, October 2003.

[29] G. Park, H.H. Cudney, and D.J. Inman, "Impedance-Based Health Monitoring of Civil Structural Components," *ASCE Journal of Infrastructure Systems*, vol. 6, no. 4, pp. 153-160, December 2000.

[30] V. Giurgiutiu and A.N. Zagrai, "Embedded Self-Sensing Piezoelectric Active Sensors for On-Line Structural Identification," *ASME Journal of Vibration and Acoustics*, vol. 124, pp. 116-125.

[31] S.W. Doebling, C.R. Farrar, and M.B. Prime, "A Summary Review of Vigration-Based Damage Identification Methods," *Shock and Vibration Digest*, vol. 30, no. 2, pp. 91-105, September 1998.

[32] J.J. Dosch, D.J. Inman, and E. Garcia, "A Self-Sensing Piezoelectric Actuator for Collocated Control," *Journal of Intelligent Material Systems and Structures*, vol. 3, no. 1, pp. 166-185, January 1992.

[33] H.T. Banks, D.J. Inman, D.J. Leo, and Y. Wang, "An Experimentally Validated Damage Detection Theory in Smart Structures," *Journal of Sound and Vibration*, vol. 191, no. 5, pp. 859-880, April 1996.

[34] TMS320F2812 Digital Signal Processor Data Manual, Texas Instruments Inc., May 2006.

[35] OPA4342 Low-Cost, Low-Power, Rail-to-Rail Operational Amplifiers, Texas Instruments Inc., August 2000.

[36] TLV277x Family of 2.7-V High-Slew-Rate Rail-to-Rail Output Operational Amplifiers with Shutdown, Texas Instruments Inc., February 2004.

[37] ANSI/IEEE Std 176-1987, IEEE Standard on Piezoelectricity, 1987.

[38] S. Sherrit, H.D. Wiederick, B.K. Mukherjee, and M. Sayer, "An Accurate Equivalent Circuit for the Unloaded Piezoelectric Vibrator in the Thickness Mode," *Journal of Physics D: Applied Physics*, vol. 30, no. 16, pp. 2354-2363, August 1997.

[39] C.H. Park, "On the Circuit Model of Piezoceramics," *Journal of Intelligent Material Systems and Structures*, vol. 12, pp. 515-522, July 2001.

[40] M. Guan and W.H. Liao, "Studies on the Circuit Models of Piezoelectric Ceramics," *International Conference on Information Acquisition*, pp. 26-31, June 2004.

[41] X.M. Wang, and Y.P. Shen, "On the Characterization of Piezoelectric Actuators Attached to Structures," *Smart Materials and Structures*, vol. 7, no. 3, pp. 389-395, June 1998.

[42] http://www.drdo.org/pub/techfocus/oct1999/lead.htm, Lead Zirconate Titanate Based Piezoceramics, Bulletin of Defence Research and Development Organization, vol. 7, no. 5, October 1999.

[43] http://www.piezo.com/prodsheet2sq5H.html, PSI-5H4E Piezoceramic Sheets and Their Properties, Piezo Systems, Inc.

[44] Introduction to Piezo Transducers, Piezo Systems, Inc., pp. 20-62, 2006.

[45] D.A. Skoog, F.J. Holler, and S.R. Crouch, Principles of Instrumental Analysis, 6th edition, Brooks and Cole, 2006.

[46] G.H. Gautschi, *Piezoelectric Sensorics: Force, Strain, Pressure, Acceleration and Acoustic Emission Sensors, Materials and Amplifiers*, Springer, 2002.

[47] L.F Brown and D.L. Carlson, "Ultrasound Transducer Models for Piezoelectric Polymer Films," *IEEE Transactions on Ultrasonics, Ferroelectrics, and Frequency Control*, vol. 36, no. 3, pp. 313-318, May 1989.

[48] H. Shimizu and S. Saito, "An Improved Equivalent Circuit of Piezoelectric Transducers Including the Effect of Dielectric Loss," *Journal of the Acoustical Society of Japan*, vol. 6, no. 3, pp. 225-234, 1985.

[49] S. Butterworth, "On Electrically Maintained Vibrations," Proceedings of the Physical Society of London, vol. 27, no. 1, pp. 410-424, 1914.

[50] NDT Resource Center, Introduction to Ultrasonic Testing, http://www.ndt-ed.org/EducationResources/CommunityCollege/Ultrasonics/Introduction/description.htm

[51] M. Huang, L. Jiang, P.K. Liaw, C.R. Brooks, R. Seeley, and D.L. Klarstrom, "Using Acoustic Emission in Fatigue and Fracture Materials Research," *Journal of Metals*, vol. 50, no. 11, pp, November 1998.

[52] Impact-Echo Testing, WDP http://www.wdpa.com/impactecho.html

[53] The Impact-Echo Method, Impact Echo Instruments, http://www.impact-echo.com/Impact-Echo/impact.htm

[54] N.J. Carino, Impact-Echo Principle, http://ciks.cbt.nist.gov/~carino/ieprin.html

[55] P.Z. Peebles Jr., Probability, Random Variables, and Random Signal Principles, 4th edition, McGraw-Hill, 2001.

[56] AD5933 1-MSPS, 12-Bit Impedance Converter Network Analyzer, Analog Devices, September 2005.

[57] S.K. Mitra, Digital Signal Processing, 2nd edition, McGraw-Hill, 2001.

[58] D.M. Peairs, P.A. Tarazaga, and D.J. Inman, "Frequency Range Selection for Impedance-based Structural Healthy Monitoring," *Journal of Vibration and Acoustics*, vol. 129, no. 6, pp. 701-709, December 2007.

[59] L.D. Peterson, K.F. Alvin, S.W. Doebling, and K.C. Park, "Damage Detection Using Experimentally Measured Mass and Stiffness Matrices," *AIAA Structures, Structural Dynamics, and Materials Conference*, pp. 1518-1528, April 1993.

[60] J. Kim, B.L. Grisso, J.K. Kim, D.S. Ha, and D.J. Inman, “Electrical Modeling of Piezoelectric Ceramics for Analysis and Evaluation of Sensory Systems,” *IEEE Sensors Applications Symposium*, February 2008.

Vita

Jina Kim received a Bachelor of Science in Electrical Engineering from Hanyang University in Seoul, Korea in August 2000. She graduated with a Master of Science in Electrical Engineering from Virginia Tech in Blacksburg in December 2002. From May 2005 to May 2006, she worked as an Applications Engineer at Texas Instrument, Inc. in Dallas, Texas.

Since August 2000, she has worked under Dr. Dong Ha's advisory at the Virginia Tech VLSI for Telecommunications (VTVT) laboratory and researched low-power digital integrated circuit design, reconfigurable architecture design for wireless communication systems, and signal processing and system level design for low-power structural health monitoring systems. During her Ph.D. work, she published several IEEE conference papers regarding reconfigurable modem architecture and low-power structural health monitoring systems, and filed three patent applications in the U.S. and in Korea. She plans to graduate in the fall of 2007. After receiving her Ph.D. degree, she plans to look for a job in Portland, Oregon.